



A SYSTEMATIC STUDY OF THE
OPTICAL AND ELECTRICAL PROPERTIES
OF $\text{Ge}_{1-y}\text{Sn}_y$ AND $\text{Ge}_{1-x-y}\text{Si}_x\text{Sn}_y$
SEMICONDUCTOR ALLOYS

DISSERTATION

Thomas R. Harris
AFIT-ENP-DS-14-M-04

DEPARTMENT OF THE AIR FORCE
AIR UNIVERSITY

AIR FORCE INSTITUTE OF TECHNOLOGY

Wright-Patterson Air Force Base, Ohio

DISTRIBUTION STATEMENT A.
APPROVED FOR PUBLIC RELEASE; DISTRIBUTION UNLIMITED

The views expressed in this document are those of the author and do not reflect the official policy or position of the United States Air Force, the United States Department of Defense or the United States Government.

AFIT-ENP-DS-14-M-04

A SYSTEMATIC STUDY OF THE
OPTICAL AND ELECTRICAL PROPERTIES
OF $\text{Ge}_{1-y}\text{Sn}_y$ AND $\text{Ge}_{1-x-y}\text{Si}_x\text{Sn}_y$ SEMICONDUCTOR ALLOYS

DISSERTATION

Presented to the Faculty
Graduate School of Engineering and Management
Air Force Institute of Technology
Air University
Air Education and Training Command
in Partial Fulfillment of the Requirements for the
Degree of Doctor of Philosophy

Thomas R. Harris, B.S., M.S.

March 2014

DISTRIBUTION STATEMENT A.
APPROVED FOR PUBLIC RELEASE; DISTRIBUTION UNLIMITED

AFIT-ENP-DS-14-M-04

A SYSTEMATIC STUDY OF THE
OPTICAL AND ELECTRICAL PROPERTIES
OF $\text{Ge}_{1-y}\text{Sn}_y$ AND $\text{Ge}_{1-x-y}\text{Si}_x\text{Sn}_y$ SEMICONDUCTOR ALLOYS

Thomas R. Harris, B.S., M.S.

Approved:

//signed//

14 February 2014

Yung Kee Yeo, PhD (Chairman)

Date

//signed//

14 February 2014

Robert Hengehold, PhD (Member)

Date

//signed//

14 February 2014

Marina Ruggles-Wrenn, PhD (Member)

Date

Accepted:

//signed//

27 February 2014

Adedeji B. Badiru, PhD
Dean, Graduate School of Engineering
and Management

Date

Abstract

Silicon is very well known for its electronic device applications, but Si-based microelectronics will eventually reach their ultimate physical size and technological limits. In order to overcome these limitations and to broaden the role of Si technology into the realm of optical signal generation and processing, an intensive research effort has been made. As a result, a significant breakthrough has recently been achieved in fabricating Si- and Ge-based direct bandgap semiconducting materials such as $\text{Ge}_{1-y}\text{Sn}_y$ and $\text{Ge}_{1-x-y}\text{Si}_x\text{Sn}_y$ alloys. These materials represent a new paradigm in the integration of optical components with Si electronics on a single chip. Therefore, in order to fully utilize these materials in potential new novel optoelectronic devices, the optical and electrical properties of the $\text{Ge}_{1-y}\text{Sn}_y$ and $\text{Ge}_{1-x-y}\text{Si}_x\text{Sn}_y$ alloys were investigated as a function of alloy composition and sample temperature.

Temperature (T)-dependent photoluminescence (PL) has been investigated for *p*-Ge, *n*- $\text{Ge}_{1-y}\text{Sn}_y$ (0.3% Sn), and *p*- $\text{Ge}_{1-y}\text{Sn}_y$ (1.0% Sn) epitaxial layers grown on Si substrates. All these samples show both direct (E_D) and indirect (E_{ID}) bandgap related optical PL transitions at low temperatures (LTs) and/or at room temperature (RT), but they show vastly different temperature-dependent behavior. Moreover, they all clearly show the competitiveness between the direct (E_D) and indirect (E_{ID}) bandgap related PL transitions as temperature changes. In addition, PL was measured at RT for a set of *n*- $\text{Ge}_{1-y}\text{Sn}_y$ samples with Sn contents ranging from 0.3% to 3.6%. A reduction in the PL peak energy with increasing Sn content was observed and compared with theory. Furthermore, all the measured E_D PL peak energies were consistently lower than the theoretically calculated values, which

could imply a larger reduction in the direct bandgap due to Sn. Therefore, these T-dependent PL studies indicate that the indirect-to-direct bandgap transitions of $n\text{-Ge}_{1-y}\text{Sn}_y$ might take place at lower Sn contents than the theory predicts. Also, more importantly, strong direct bandgap PL emission was observed at RT from almost all the samples, which indicates that these semiconducting materials could be very promising candidates for Si-based light emitting devices.

The electrical properties of p -type Ge, $\text{Ge}_{1-y}\text{Sn}_y$, and $\text{Ge}_{0.882}\text{Si}_{0.090}\text{Sn}_{0.028}$ samples grown on n -type Si substrates as well as $p\text{-Ge}_{0.90}\text{Si}_{0.08}\text{Sn}_{0.02}$ samples grown on $p\text{-Ge}$ substrates have been investigated using temperature-dependent Hall-Effect measurements. Degenerate parallel conducting layers were found in almost all the samples, which are believed to be associated with dislocation defects at the interface produced by the lattice mismatch between the epilayers and substrates. These degenerate conducting layers affect the electrical properties of all the thin epitaxial films, and therefore may also significantly affect the operation of electronic and optoelectronic devices made from these materials. In addition, T-dependent Hall-effect measurements showed that these materials exhibit a conductivity type change from p to n at around 370-435 K. The mobilities of these samples are generally lower than that of bulk Ge due to carrier scattering near the interfacial layer and also due to alloy scattering. To further investigate the properties of the $\text{Ge}_{1-y}\text{Sn}_y$ and $\text{Ge}_{1-x-y}\text{Si}_x\text{Sn}_y$ layers alone, etch studies were performed with T-dependent Hall-effect measurements made from 10-300 K after each etch. Reasonable results for the average volume carrier density in the film were obtained. It was also found that in vacuum, there exists a high level of n -type surface states at the surface of almost all the samples. In conclusion, these studies should be very useful for the development of practical electrically-injected light-emitting diodes (LEDs) and laser diodes (LDs) based on direct bandgap $\text{Ge}_{1-y}\text{Sn}_y$ alloys grown on Si.

AFIT-ENP-DS-14-M-04

To my wife

Acknowledgements

It is no secret that earning a Ph.D is not a singular effort. This case is no exception and there are many people to whom I owe a great deal of gratitude and without whom this would not have been possible. First of all, I must thank my advisor, Dr. Yeo, whose expertise and guidance have been invaluable. He has invested a great deal in me and has taught me a lot of things, not just about physics, but about life as well. I would also like to thank Dr. Ryu for all of her help in collecting, analyzing, and plotting data as well as writing and editing papers. To Mike Ranft and Greg Smith, thank you for all of your help making sure the equipment was always working so that I could take measurements. To my immediate family, my house church family, and my friends, thank you for all of your prayers and support. To my wife, thank you for your patience, your willingness to listen, and your constant encouragement throughout this journey.

Thomas R. Harris

Contents

	Page
Abstract	iv
Acknowledgements	vii
List of Figures	x
List of Tables	xiv
I. Introduction	1
II. Background	9
Early Crystal Growth and Band Structure Calculations	9
Recent Growth and Structural Characterization (ASU)	10
Optical Characterization	11
III. Experiment	14
Sample Description	14
Ge/Si Sample Growth	14
Ge _{1-y} Sn _y /Si Sample Growth	14
Ge _{0.90} Si _{0.08} Sn _{0.02} Sample Growth	14
Post-Growth Characterization	15
Photoluminescence	15
Hall-Effect and Etching Studies	17
IV. Results and Discussion	20
Optical Characterization	20
PL of Ge/ <i>p</i> -Si(100)	20
PL of <i>n</i> -Ge _{0.997} Sn _{0.003} / <i>n</i> -Si(100)	25
PL of <i>p</i> -Ge _{0.99} Sn _{0.01} / <i>n</i> -Si(100)	30
PL of <i>n</i> -Ge _{1-y} Sn _y / <i>n</i> -Si(100) (0.3% - 3.6% Sn)	35
Electrical Characterization	43
Hall-Effect Measurements of <i>p</i> -Ge, <i>p</i> -Ge _{1-y} Sn _y (0.06–0.10% Sn), and <i>p</i> -Ge _{0.882} Si _{0.090} Sn _{0.028} Samples Grown on <i>n</i> -Si Substrates	43
Analysis of the <i>p</i> -Ge _{1-y} Sn _y / <i>n</i> -Si (0.06% Sn) Sample	51
Analysis of the <i>p</i> -Ge _{1-y} Sn _y / <i>n</i> -Si (0.1% Sn) Sample	68
Analysis of the <i>p</i> -Ge/ <i>n</i> -Si Sample	79
Hall-Effect Measurements of <i>p</i> -Ge _{0.90} Si _{0.08} Sn _{0.02} / <i>p</i> -Ge	90

	Page
Analysis of the p -Ge _{0.90} Si _{0.08} Sn _{0.02} / p -Ge (1×10^{18} cm ⁻³) Sample	97
V. Conclusions	105
VI. Recommendations for Future Work	108
Appendix A. Magnetic Field Correction	109
Appendix B. Band Structure Calculations	110
Appendix C. Temperature Dependent Strain Calculation	113
Appendix D. Publications and Presentations	116
Bibliography	117

List of Figures

Figure		Page
1	Schematic diagram of photoluminescence experimental setup.	16
2	Schematic diagram of the Hall-effect measurement system	18
3	Temperature-dependent PL measurements of Ge/ <i>p</i> -Si(100)	21
4	Simple band diagrams for bulk Ge and the 0.19% tensile strained <i>p</i> -Ge/ <i>p</i> -Si sample	23
5	Temperature-dependent PL spectra of the P-doped <i>n</i> -Ge _{0.997} Sn _{0.003} grown on <i>n</i> -Si substrate	26
6	Simple band diagrams for 0.22% tensile strained <i>n</i> -Ge _{0.997} Sn _{0.003} /Si sample	28
7	Temperature-dependent PL spectra of a B-doped <i>p</i> -Ge _{0.99} Sn _{0.01} / <i>n</i> -Si sample	31
8	Simple band diagrams for 0.16% tensile strained <i>p</i> -Ge _{0.99} Sn _{0.01} /Si sample	33
9	Normalized room temperature PL spectra of P-doped <i>n</i> -Ge _{1-y} Sn _y / <i>n</i> -Si samples	37
10	Representative diagram for bandgap narrowing (BGN) in Ge using the empirical expression in Eqn. (9) derived by Camacho-Aquilera et al	38
11	Unnormalized room temperature PL spectra of P-doped <i>n</i> -Ge _{1-y} Sn _y samples plotted as a function of Sn concentration	41
12	Sheet carrier concentration plotted as a function of inverse temperature for Ge, Ge _{1-y} Sn _y , and Ge _{0.882} Si _{0.090} Sn _{0.028} films along with the <i>n</i> -Si substrate	45
13	Carrier mobility plotted as a function of temperature for Ge, Ge _{1-y} Sn _y , and Ge _{0.882} Si _{0.090} Sn _{0.028} films along with the <i>n</i> -Si substrate	48

Figure		Page
14	Log conductivity plotted as a function of inverse temperature for Ge, $\text{Ge}_{1-y}\text{Sn}_y$, and $\text{Ge}_{0.882}\text{Si}_{0.090}\text{Sn}_{0.028}$ films along with the n -Si substrate	50
15	Two-layer model fit for the $p\text{-Ge}_{0.9994}\text{Sn}_{0.0006}/n\text{-Si}$ sample	53
16	Classical energy-band diagrams at the $p\text{-Ge}(\text{Sn})$ surface showing an n -type inversion layer with accumulated surface electrons	56
17	Sheet carrier concentration plotted as a function of inverse temperature for the $p\text{-Ge}_{0.9994}\text{Sn}_{0.0006}/n\text{-Si}$ sample for all etches.	58
18	Carrier mobility plotted as a function of temperature for the $p\text{-Ge}_{0.9994}\text{Sn}_{0.0006}/n\text{-Si}$ sample for all etches.	60
19	Log conductivity plotted as a function of inverse temperature for the $p\text{-Ge}_{0.9994}\text{Sn}_{0.0006}/n\text{-Si}$ sample for all etches.	62
20	Room temperature sheet carrier concentration plotted as a function of etch depth for the $p\text{-Ge}_{0.9994}\text{Sn}_{0.0006}/n\text{-Si}$ sample.	63
21	Volume carrier concentration plotted as a function of etch depth for the $p\text{-Ge}_{0.9994}\text{Sn}_{0.0006}/n\text{-Si}$ sample calculated using the differential Hall model	65
22	Measured sheet carrier profiles at different temperatures for the $\text{Ge}_{0.9994}\text{Sn}_{0.0006}$ sample.	67
23	Calculated volume carrier profiles at different temperatures for the $\text{Ge}_{0.9994}\text{Sn}_{0.0006}$ sample.	67
24	Sheet carrier concentration plotted as a function of inverse temperature for the $p\text{-Ge}_{0.999}\text{Sn}_{0.001}/n\text{-Si}$ sample for all etches.	69
25	Carrier mobility plotted as a function of temperature for the $p\text{-Ge}_{0.999}\text{Sn}_{0.001}/n\text{-Si}$ sample for all etches.	71
26	Log conductivity plotted as a function of inverse temperature for the $p\text{-Ge}_{0.999}\text{Sn}_{0.001}/n\text{-Si}$ sample for all etches.	72

Figure		Page
27	Room temperature sheet carrier concentration plotted as a function of etch depth for the $p\text{-Ge}_{0.999}\text{Sn}_{0.001}/n\text{-Si}$ sample including linear fits with different slopes.	73
28	Calculated volume carrier concentration plotted as a function of etch depth for the $p\text{-Ge}_{0.999}\text{Sn}_{0.001}/n\text{-Si}$ sample at room temperature	76
29	Measured sheet carrier profiles at different temperatures for the $\text{Ge}_{0.999}\text{Sn}_{0.001}$ sample.	78
30	Calculated volume carrier profiles at different temperatures for the $\text{Ge}_{0.999}\text{Sn}_{0.001}$ sample.	78
31	Sheet carrier concentration plotted as a function of inverse temperature for the $p\text{-Ge}/n\text{-Si}$ sample for all etches.	80
32	Carrier mobility plotted as a function of temperature for the $p\text{-Ge}/n\text{-Si}$ sample for all etches.	82
33	Log conductivity plotted as a function of inverse temperature for the $p\text{-Ge}/n\text{-Si}$ sample for all etches.	84
34	Room temperature sheet carrier concentration plotted as a function of etch depth for the $p\text{-Ge}/n\text{-Si}$ sample.	86
35	Volume carrier concentration plotted as a function of etch depth for the $p\text{-Ge}/n\text{-Si}$ sample calculated using the differential Hall model	87
36	Measured sheet carrier profiles at different temperatures for the Ge/Si sample.	89
37	Calculated volume carrier profiles at different temperatures for the Ge/Si sample.	89
38	Sheet carrier concentration plotted as a function of inverse temperature for undoped and p -type doped $\text{Ge}_{0.90}\text{Si}_{0.08}\text{Sn}_{0.02}/p\text{-Ge}$ samples along with the $p\text{-Ge}$ substrate	91
39	Carrier mobility plotted as a function of temperature for undoped and p -type doped $\text{Ge}_{0.90}\text{Si}_{0.08}\text{Sn}_{0.02}/p\text{-Ge}$ samples along with the $p\text{-Ge}$ substrate	94

Figure		Page
40	Log conductivity plotted as a function of inverse temperature for undoped and p -type doped $\text{Ge}_{0.90}\text{Si}_{0.08}\text{Sn}_{0.02}/p\text{-Ge}$ samples along with the $p\text{-Ge}$ substrate.	96
41	Sheet carrier concentration plotted as a function of inverse temperature for the $p\text{-Ge}_{0.90}\text{Si}_{0.08}\text{Sn}_{0.02}/p\text{-Ge}$ sample for all etches.	98
42	Carrier mobility plotted as a function of temperature for the $p\text{-Ge}_{0.90}\text{Si}_{0.08}\text{Sn}_{0.02}/p\text{-Ge}$ sample for all etches.	99
43	Log conductivity plotted as a function of inverse temperature for the $p\text{-Ge}_{0.90}\text{Si}_{0.08}\text{Sn}_{0.02}/p\text{-Ge}$ sample for all etches.	101
44	Room temperature sheet carrier concentration plotted as a function of etch depth for the $p\text{-Ge}_{0.90}\text{Si}_{0.08}\text{Sn}_{0.02}/p\text{-Ge}$ sample.	102
45	Volume carrier concentration plotted as a function of etch depth for the $p\text{-Ge}_{0.90}\text{Si}_{0.08}\text{Sn}_{0.02}/p\text{-Ge}$ sample calculated using the differential Hall model	103
46	Measured sheet carrier profiles at different temperatures for the $p\text{-Ge}_{0.90}\text{Si}_{0.08}\text{Sn}_{0.02}/p\text{-Ge}$ sample.	104
47	Calculated volume carrier profiles at different temperatures for the $p\text{-Ge}_{0.90}\text{Si}_{0.08}\text{Sn}_{0.02}/p\text{-Ge}$ sample.	104
48	Calculated compositional dependence of the unstrained $\text{Ge}_{1-y}\text{Sn}_y$ band gaps	111
49	Strain dependence of the Γ -hh (red) and Γ -lh (black) band gaps of $\text{Ge}_{1-y}\text{Sn}_y$	112

List of Tables

Table		Page
1	Various properties of selected $n\text{-Ge}_{1-y}\text{Sn}_y/n\text{-Si}$ samples studied ($y < 0.036$)	36
2	Measured RT PL peak positions of selected $n\text{-Ge}_{1-y}\text{Sn}_y/n\text{-Si}$ samples ($y < 0.036$)	36
3	Summary of Hall-effect data for $p\text{-Ge}$, $p\text{-Ge}_{1-y}\text{Sn}_y$, and $p\text{-Ge}_{0.882}\text{Si}_{0.090}\text{Sn}_{0.028}$ samples measured at room temperature.	43
4	Measured sheet carrier concentration in cm^{-2} as a function of etch depth at selected temperatures for the $p\text{-GeSn}/n\text{-Si}$ (0.06% Sn) sample.	57
5	Sheet carrier concentration measured at RT in both air and vacuum as a function of etch depth for the $p\text{-GeSn}/n\text{-Si}$ (0.06% Sn) sample.	63
6	Measured sheet carrier concentration in cm^{-2} as a function of etch depth at selected temperatures for the $p\text{-GeSn}/n\text{-Si}$ (0.1% Sn) sample.	68
7	Sheet carrier concentration measured at RT in both air and vacuum as a function of etch depth for the $p\text{-GeSn}/n\text{-Si}$ (0.1% Sn) sample.	73
8	Measured sheet carrier concentration in cm^{-2} as a function of etch depth at selected temperatures for the $p\text{-Ge}/n\text{-Si}$ sample.	79
9	Sheet carrier concentration measured at RT in both air and vacuum as a function of etch depth for the $p\text{-Ge}/n\text{-Si}$ sample.	86
10	Parameters used to calculate the compositional dependence of the band gap in $\text{Ge}_{1-y}\text{Sn}_y$ alloys.	110
11	Parameters used to calculate the strain dependence of the band gap in $\text{Ge}_{1-y}\text{Sn}_y$ alloys.	112
12	Parameters used to calculate the temperature dependence of the thermal expansivities of Si and Ge	114

Table		Page
13	Comparison of room temperature and low temperature strain values for selected Ge and $\text{Ge}_{1-y}\text{Sn}_y$ samples	115

A SYSTEMATIC STUDY OF THE
OPTICAL AND ELECTRICAL PROPERTIES
OF $\text{Ge}_{1-y}\text{Sn}_y$ AND $\text{Ge}_{1-x-y}\text{Si}_x\text{Sn}_y$ SEMICONDUCTOR ALLOYS

I. Introduction

It is a well known fact that current silicon-based microelectronics technology is fast approaching its fundamental limits. Limits in both minimum feature size as well as maximum bandwidth are major hurdles in the development of next-generation electronic devices. To overcome these limitations, the integration of optical components together with traditional electronic circuits on the same silicon chip has been pursued for many years now. Much progress has been made in this area, and many of the components needed have been developed including waveguides, electro-optic modulators, and optical switches. However, the development of efficient light sources and detectors continues to be the most significant fundamental challenge. Although there are several promising candidates, there has not yet been a clear winner. A major challenge in the development of light sources and detectors comes from the fact that both silicon (Si) and germanium (Ge) are naturally poor light emitters due to their fundamental indirect energy-gap. In order to satisfy conservation of momentum, phonons are usually involved in the optical transition, which results in a very inefficient process since it requires two particles with appropriate energy and momentum (often called a second-order process.)

In particular, silicon's very large direct band-gap energy of 3.4 eV (compared to its indirect gap of 1.12 eV) makes it an unlikely candidate for a light emitter. Germanium on the other hand appears to be much more promising. It too is an

indirect material, but the separation between the direct “ Γ -valley” and indirect “L-valley” in the conduction band is a mere 0.14 eV [1]. Additionally, the dipole matrix element for the direct transition is very large, which, in combination with a short radiative lifetime, means that the direct transition in Ge is actually quite efficient. Because of this reason, Ge is sometimes referred to as a “pseudo-direct” material. In fact, light emission in Ge is limited mostly by the electron population in the Γ -valley, which is ordinarily quite low.

To overcome this inherent “indirectness” in Ge, two things must be accomplished:

1. a reduction in the Γ -L separation
2. an increase in the number of conduction electrons in the Γ -valley.

Fortunately, it has been recently shown that the Γ -L separation can be decreased with the addition of tensile strain [2]. In fact, Ge is even predicted to become a true direct-bandgap material at around 2.0% tensile strain [3]. Recently, strain values up to about 0.22% have been achieved in Ge films grown directly on Si substrates [4]. This is remarkable considering that the lattice constant of Si is roughly 4% smaller than that of Ge, which would result in a natural compressive strain in the Ge layer. However, these Ge-on-Si layers are grown at high temperatures (600 - 650 °C) with the tensile strain being created upon cooling due to the large thermal expansion mismatch between Si and Ge [5]. Subsequent rapid thermal annealing (RTA) treatments at 900 °C and 780 °C were shown to greatly reduce the number of threading dislocations present in the Ge layers and resulted in high quality strained films [6].

It has also been shown that direct gap emission in Ge can be further enhanced by heavy n-type doping ($>10^{19} \text{ cm}^{-3}$) which raises the Fermi level above the level of the L-valley in the conduction band and results in a partial filling of the band with electrons [2]. Additional conduction electrons provided by thermalization, photo-excitation, or electrical injection can then “spill over” into the Γ -valley, where

they may recombine directly with holes in the valence band and produce photons. This has led to the observation of increased direct-gap photoluminescence in n-type doped Ge-on-Si layers [4]. More remarkably, it has led to the recent development of an optically-pumped Ge-on-Si laser reported by Liu, et al [7].

While these are unprecedented achievements in the field of silicon photonics, there are still many hurdles to overcome. For instance, the high growth and high annealing temperatures required are incompatible with current standard silicon-based complementary metal-oxide-semiconductor (CMOS) processes and facilities. The high levels of strain and n-type doping may affect material stability and device performance or have other unintended consequences. These and other challenges may prohibit the large scale integration of a Ge-on-Si laser with other optical and electronic components on the same Si chip.

$\text{Ge}_{1-y}\text{Sn}_y$ alloys have recently been presented as an attractive alternative to tensile-strained Ge-on-Si [8]. Sn-alloying in Ge has been shown to have an effect similar to that of tensile strain in that it reduces the Γ -L separation. For example, incorporating 1% Sn in Ge is roughly equivalent to increasing the tensile strain by about 0.35% [9]. Furthermore, this material is predicted to undergo an indirect-to-direct transition at around 20% Sn [10]. This prediction assumes a simple linear interpolation between the bandgaps of pure Ge and α -Sn at the Γ - and L-points, respectively. However, recent experimental measurements suggest that the crossover may occur at much smaller Sn concentrations (9% [11], 7.1% [12] and 6% [13]), indicating a large bowing parameter (1.8 to 2.8 eV) for the direct transition.

Recent developments in the growth and processing of binary $\text{Ge}_{1-y}\text{Sn}_y$ and ternary $\text{Ge}_{1-x-y}\text{Si}_x\text{Sn}_y$ semiconductor alloys have led to a new generation of device-quality materials grown directly on Si. The $\text{Ge}_{1-y}\text{Sn}_y$ alloy system is predicted to undergo an indirect to direct transition at around $y = 0.2$. Recent

experimental data suggests it may occur at much lower Sn concentrations, between 6% and 10%, making it possible to fabricate for the first time a true direct-bandgap semiconductor entirely out of Group-IV materials. Even with small amounts of Sn ($\sim 1\%$), these materials show a significant reduction in the Γ -L separation (~ 30 meV), offering an attractive alternative to tensile strained Ge-on-Si. Similarly, $\text{Ge}_{1-x-y}\text{Si}_x\text{Sn}_y$ is predicted to display a direct-bandgap that is tunable above and below that of pure Ge (0.80 eV). Also, the ternary alloy allows for the decoupling of the lattice constant and bandgap energy, enabling a flexibility in bandgap and strain engineering heretofore unattainable.

These materials show much promise for use in many optoelectronic devices including integrated electronics and photonics in a single Si chip, light emitters (LEDs, laser diodes), photo-detectors, and electro-optical modulators as well as biological and chemical sensors. Despite the substantial recent progress in crystal growth, however, the development of these materials is still in its infancy and much work remains to be done. A thorough understanding of these new materials and their behavior is needed in order for their full potential to be realized. To date there is a lack of comprehensive and systematic studies of these materials and all of their optical and electronic properties in the literature.

Researchers at Arizona State University (ASU) have recently fabricated new fully-relaxed, device-quality $\text{Ge}_{1-y}\text{Sn}_y$ and $\text{Ge}_{1-x-y}\text{Si}_x\text{Sn}_y$ alloys grown directly on Si [14, 15]. These materials are grown using an ultra-high vacuum chemical vapor deposition (UHV-CVD) system with custom designed chemical precursors [16]. Through accurate control of the crystal growth, researchers at ASU are able to produce $\text{Ge}_{1-y}\text{Sn}_y$ materials with precise and reproducible Sn concentrations. Ternary $\text{Ge}_{1-x-y}\text{Si}_x\text{Sn}_y$ materials have also been grown using this UHV-CVD method with Sn concentrations ranging from 2% to 7% and Si concentrations

ranging from 8% to 20% [17]. These samples have shown good crystallinity which was confirmed by high-resolution x-ray diffraction (HRXRD) and cross-sectional transmission electron microscopy (XTEM) measurements. They also show almost perfect substitutionality of Si and Sn atoms in the Ge zincblende (diamond) lattice as measured by Rutherford backscattering (RBS) and HRXRD. Finally, these films exhibit an adjustable strain state ranging from compressive to tensile strain with full relaxation also being achieved.

These relatively new materials have tremendous potential for application in many next generation electronic and optoelectronic devices including photonic integrated circuits (PICs), optoelectronic integrated circuits (OEICs), high-mobility *p*-type metal-oxide-semiconductor field effect transistors (MOSFETS) as source/drain materials, light-emitting diodes (LEDs) and laser diodes (LDs), photodetectors, infrared amplifiers, and electro-optical modulators and routing switches, as well as biological and chemical sensors. Both $\text{Ge}_{1-y}\text{Sn}_y$ and $\text{Ge}_{1-x-y}\text{Si}_x\text{Sn}_y$ grown directly on Si can also be used as buffer layers for the subsequent growth of either tensile-strained Ge layers or III-V compound semiconductors such as GaAs and InGaAs [18].

The first component of this work was a systematic photoluminescence (PL) study of undoped, *p*-type, and *n*-type doped $\text{Ge}_{1-y}\text{Sn}_y/\text{Si}(100)$ samples with $0.0006 < y < 0.036$. Post-growth annealing treatments have been shown to improve crystal quality and remove unwanted defects, resulting in increased luminescent intensity in $\text{Ge}_{1-y}\text{Sn}_y$ samples. Therefore, annealing treatments were performed immediately after growth with different temperatures and times used for different sample compositions. These types of materials have not been extensively studied to date due to many factors including difficulties in crystal growth. To facilitate this research effort, $\text{Ge}_{1-y}\text{Sn}_y/\text{Si}(100)$ samples were requested from researchers at ASU in

a collaborative research effort. The subsequent measurements should also provide valuable feedback to the crystal growers and allow for further optimization of growth and post-processing conditions.

Photoluminescence is a very versatile and powerful tool and thus was chosen as the primary method for the optical characterization of these $\text{Ge}_{1-y}\text{Sn}_y$ samples. To put it simply, photoluminescence is one of the easiest ways to measure direct-gap behavior. In general, direct-gap materials show much stronger luminescence than indirect-gap materials. The recent observations of room temperature luminescence from $\text{Ge}_{1-y}\text{Sn}_y$ alloys is promising, however the Sn concentrations of these samples ($y < 0.03$) was not sufficient to produce a true direct bandgap material, i.e. one where $E_{\Gamma} < E_{\text{L}}$. Further, the luminescent intensity was seen to decrease with increasing Sn content, indicating the possibility of some deleterious effects due to the addition of Sn. It is expected that the luminescence from a $\text{Ge}_{1-y}\text{Sn}_y$ sample which is a true direct-bandgap material would be significantly greater than its “pseudo-direct” counterparts. Because of this, PL can be used to differentiate between indirect- and direct-gap materials. Furthermore, for some samples, both direct and indirect-gap emission peaks have been observed at room temperature. In these samples, the dominant PL peak is generally attributed to the direct gap, while the weaker low-energy peak is attributed to the indirect gap. Because the peaks are closely spaced (< 140 meV) and are relatively broad, it is often difficult to resolve them at room temperature. However, the indirect gap is often stronger at lower temperatures, so temperature dependent PL can be used to more accurately determine both the direct and indirect gaps. In this way, PL can be used to experimentally determine the exact point at which the indirect-to-direct crossover occurs. This information is vital in the development of optoelectronic devices from $\text{Ge}_{1-y}\text{Sn}_y$ materials and compliments the theoretical work that has already been

done in predicting this crossover point.

Temperature-dependent PL is a valuable characterization tool and can provide insight into the mechanisms involved in luminescence and how those evolve with a change in temperature. The ratio of the integrated PL intensity of the direct and indirect bandgap related peaks as a function of temperature is of particular interest. Temperature-dependent Hall-effect measurements will be performed in tandem to provide information on the carrier concentration. Laser power-dependent PL will also be performed to detect any changes in peak position and relative peak intensities. The dependence of the integrated PL intensity with laser power gives some insight into the non-radiative recombination processes. For example, it is well known that if the dependence is highly non-linear, then Auger recombination is dominant. A change in the relative intensities of the direct and indirect PL peaks as a function of laser power could indicate a departure from “equilibrium” conditions which is usually an assumption made in the analysis of PL data. Evidence for some “quasi-equilibrium” has been seen even in pure Ge-on-Si films in the form of an increased direct-to-indirect intensity ratio relative to bulk Ge. Some of this is due to the effect of self-absorption which causes a decrease in the observed direct-gap PL intensity in the bulk material but is usually negligible in the thin films due to their small thickness. That being said, this effect cannot completely explain the increased intensity ratio observed in these films [19]. By studying a large number of samples over a wide range of compositions, processing conditions, and temperatures, we can better understand direct-gap behavior in these alloys.

As mentioned previously, there is much debate currently about where the indirect-to-direct transition will occur for the $\text{Ge}_{1-y}\text{Sn}_y$ system and predicted values vary from 6-20%. While there is not much agreement on the exact value, there seems to be a consensus on an upper limit. Most groups have rejected the initial

predictions of about 20% Sn, and instead believe the crossover will occur somewhere at or below about 11%. If this proves to be the case, then the samples obtained for this work in the range $0.003 < y < 0.06$ could lead to the observation of the first true direct bandgap group-IV semiconductor integrated directly on Si.

Additionally, PL may be performed on suitable $\text{Ge}_{1-x-y}\text{Si}_x\text{Sn}_y$ samples. To date, no PL has been observed in the ternary compound indicating that further development in the growth of these materials is needed. ASU plans to re-examine the entire growth process for $\text{Ge}_{1-x-y}\text{Si}_x\text{Sn}_y$ and hopes to produce high-quality films grown on either Si, Ge, or GaAs substrates. The ternary is of significant interest in the development of both strain-free and strain-compensated heterostructure lasers with $\text{Ge}/\text{Ge}_{1-x-y}\text{Si}_x\text{Sn}_y$ active regions as well as in photovoltaics where there is currently a great demand for a material with a bandgap in the 1 eV range. Because the bandgap of the ternary can be tuned above and below that of pure Ge, it could be a valuable material for a wide range of applications across the visible (VIS) and infrared (IR) spectrum.

II. Background

Early Crystal Growth and Band Structure Calculations

$\text{Ge}_{1-y}\text{Sn}_y$ alloys have been a material of interest for use in infrared devices since the early 60's. Even before the successful growth of single-crystal $\text{Ge}_{1-y}\text{Sn}_y$, there was much interest in the material because of its electrical and optical properties. Early theoretical efforts utilized band structure calculation methods such as the virtual crystal approximation (VCA) with tight-binding[10], density functional theory (DFT) with local density approximation (LDA)[20], and empirical pseudopotential[21]. Most of these calculations showed a near-linear dependence (i.e. small bowing) to the fundamental energy bands as a function of composition, leading to a prediction of an indirect-to-direct crossover near $y = 0.2$. However, most experimental measurements for Ge-rich alloys show a very strong deviation from linear behavior, leading to the conclusion that the methods and approximations used may not be valid for these alloys. Some more refined calculations have attempted to account for other factors such as alloy disorder, and have found a stronger compositional dependence to the band gaps [22].

Attempts to grow $\text{Ge}_{1-y}\text{Sn}_y$ materials over the last 20 years have been hampered by many factors including the very low solid solubility ($<1.0\%$) of α -Sn in Ge[23], the instability of pure α -Sn at temperatures above 13.2°C , and the large lattice mismatch ($\approx 15\%$) between the two materials[24]. Early attempts using methods like sputtering[25] and laser crystallization[26] often produced either amorphous or polycrystalline materials which cannot be used for practical devices. Some single-crystal materials were achieved using molecular beam epitaxy (MBE), however, the quality of the films was usually degraded by phase segregation (of β -Sn) and clustering of the Sn atoms. Furthermore, their potential was limited by

very small critical thicknesses (500 to 35 Å for $x = 0.02 - 0.26$)[27].

In 1997, He and Atwater reported the growth of $\text{Ge}_{1-y}\text{Sn}_y$ films ($0 < y < 0.15$) grown on Ge buffer layers on Si substrates by low-energy ion-assisted MBE[28]. Subsequent optical absorption measurements showed a very rapid shift of the absorption edge toward lower energy with increasing Sn concentration, resulting in a large extrapolated bowing parameter of 2.8 eV for the direct transition[11].

Recent Growth and Structural Characterization (ASU)

One the most impressive breakthroughs in crystal growth has been achieved by researchers at Arizona State University (ASU) who have recently fabricated new device-quality $\text{Ge}_{1-y}\text{Sn}_y$ and $\text{Ge}_{1-x-y}\text{Si}_x\text{Sn}_y$ alloys grown directly on Si using a UHV CVD method [14, 15] which utilizes custom designed chemical precursors. A first generation of materials was grown in 2002, and their growth process has been constantly refined over the last 10 years, resulting in high-quality, reproducible $\text{Ge}_{1-y}\text{Sn}_y$ and $\text{Ge}_{1-x-y}\text{Si}_x\text{Sn}_y$. Samples with up to 4% Sn have been grown using digermane (Ge_2H_6) as the Ge precursor while more recent efforts using trigermane (Ge_3H_8) have resulted in $\text{Ge}_{1-y}\text{Sn}_y$ alloys with up to 9%[29].

Numerous characterization techniques have been used on these newly-developed materials to investigate their structural properties and crystal quality. Reciprocal space maps (RSM) as well as rocking curves of the (004) reflection were generated using high resolution x-ray diffraction (HRXRD) and were used to determine the lattice constant, residual strain (both before and after annealing), and the degree of crystallinity of the $\text{Ge}_{1-y}\text{Sn}_y$ layers. Rutherford backscattering (RBS) was used to measure the Sn and Si concentrations as well as the substitutionality of the Sn and Si atoms in the lattice (given by the change in Sn and Si peaks between “random” and “aligned” modes). Secondary Ion-Mass Spectroscopy (SIMS) was used to

identify the different atomic species and their corresponding concentrations. It was also used to generate depth profiles of each species which was used to verify the layer thickness and the uniformity of any p- or n-type doping. The Sn content was also estimated using the lattice constant obtained from HRXRD in combination with a modified version of Vegard's Law. The Sn concentrations calculated using this method showed good agreement with those obtained using RBS.

Additionally, cross-sectional tunneling electron microscopy (XTEM) was employed to visually examine the quality and uniformity of the film, measure the film thickness, and observe the film-substrate interface. XTEM images show very uniform layers and smooth interfaces with the exception of periodic Lomer dislocations which serve to relieve the strain caused by the intrinsic lattice mismatch between the film and the Si substrate. Fortunately, these dislocations appear to be confined to the plane of interface with no observed dislocation cores propagating into the films. XTEM images from before and after post-growth annealing treatments clearly show a large reduction in the number of threading defects. Finally, atomic force microscopy (AFM) measurements were used to examine the surface morphology of the films. These measurements show very flat, atomically smooth surfaces with an average RMS roughness of about 1 nm (over a $5 \times 5 \mu\text{m}^2$ area).

Optical Characterization

Preliminary measurements of the optical properties of these materials have been performed using spectroscopic ellipsometry and photoreflectance (PR) spectroscopy, as well as room-temperature photoluminescence (PL) measurements. D'Costa, et. al.[13] measured critical point energies of $\text{Ge}_{1-y}\text{Sn}_y\text{-Si}$ ($y \leq 0.2$) using both photoreflectance and ellipsometry. They determined the compositional dependence of the direct gap, E_0 , as well as higher energy transitions. Unfortunately, an indirect

peak could not be resolved well in those measurements, so a determination of the Γ -L separation as a function of Sn concentration could not be made. However, all the critical point energies showed a definitive red-shift relative to those of pure Ge, which is was an encouraging result for these $\text{Ge}_{1-y}\text{Sn}_y$ materials.

Room temperature PL was reported in 2010 by Mathews, et. al. for $\text{Ge}_{1-y}\text{Sn}_y$ samples grown directly on Si with Sn concentrations ranging from 0.6 to 3.0%[9]. The observed PL showed one main peak at 0.776-0.690 eV depending on Sn content which was assigned to the direct transition and a smaller shoulder peak near 0.703 eV for 0.0% Sn which was assigned to the indirect transition. For the $\text{Ge}_{1-y}\text{Sn}_y$ materials, a systematic shift of the peak position to longer wavelengths (lower energies) was observed with increasing Sn concentration. In addition, the Γ -L separation estimated from the PL spectra was shown to decrease with increasing Sn concentration. The direct band gap energy, E_0 , can be written as a function of Sn content, y , as

$$E_0(y) = E_0^{Ge} + (E_0^{Sn} - E_0^{Ge} - b) y + by^2 \quad (1)$$

where E_0^{Ge} and E_0^{Sn} are the direct band gaps in Ge and α -Sn, and the constant b is the bowing parameter. Using the RT PL data, a value of $b = 1.8\text{eV}$ was determined. However, when the two samples with $y \leq 0.02$ were excluded, a value of $b = 2.5\text{eV}$ was obtained. This indicates a compositional dependence of the bowing parameter, i.e. a deviation from the pure quadratic behavior given by Eqn. 1.

This compositional dependence was investigated by Chibane and Ferhat[30] who performed an *ab initio* theoretical calculation with the full potential augmented plane wave (APW) plus local orbital method using the local density approximation (LDA) within the framework of density functional theory (DFT) for small Sn compositions ($x = 0.0625, 0.125, 0.1875$, and 0.25). They also performed a detailed analysis of the physical origins of the bandgap bowing and found that there were

three components: volume deformation (VD), charge exchange (CE), and structural relaxation (SR). Of these, they found that the most significant effect was the structural one (i.e. relaxation and VD) due to the large lattice mismatch between Sn and Ge ($\sim 15\%$). They expressed the compositional dependence of the band gap as

$$E_g(x) = xE_{Sn}(a_{Sn}) + (1-x)E_{Ge}(a_{Ge}) - bx(1-x) \quad (2)$$

where $E_{Sn}(a_{Sn})$ and (a_{Sn}) and $E_{Ge}(a_{Ge})$ and (a_{Ge}) are the band gaps and equilibrium lattice constants of α -Sn and Ge, respectively. The total bowing, b , is given by $b = b_{VD} + b_{CE} + b_{SR}$ where

$$b_{VD} = \frac{E_{Ge}(a_{Ge}) - E_{Ge}(a)}{x} + \frac{E_{Sn}(a_{Sn}) - E_{Sn}(a)}{1-x} \quad (3)$$

$$b_{CE} = \frac{E_{Sn}(a)}{1-x} + \frac{E_{Ge}(a)}{x} + \frac{E_{SnGe}(a)}{x(1-x)} \quad (4)$$

$$b_{SR} = \frac{E_{SnGe}(a) - E_{SnGe}(a_{eq})}{x(1-x)} \quad (5)$$

where a and a_{eq} are the unrelaxed and relaxed alloy lattice constants, respectively. For the direct gap, they found a strong bowing of 2.9 eV for small Sn content ($x \leq 0.0625$) and a slightly smaller bowing of 1.9 eV for larger Sn contents ($0.0625 \leq x \leq 0.1875$).

Despite the tremendous progress in recent years, there is still a lack of systematic studies of these materials over a wide range of compositions, sample temperatures, and device structures. Also, there is a lack of good physical explanations for some of the unexpected behaviors that have been observed. All of these factors illustrate the need for the type of systematic study that is proposed here. The details of this study are described in the next section.

III. Experiment

Sample Description

Ge/Si Sample Growth

Two pure Ge films were characterized in this study, one grown on a *p*-Si substrate for photoluminescence (PL) measurements and one grown on a high resistivity *n*-Si substrate for Hall-effect measurements. Both Ge films were grown using gas source MBE at temperatures ranging from 350 to 420 °C and at pressures ranging from 5×10^{-5} to 2×10^{-4} Torr using appropriate stock mixtures of $\text{CH}_2(\text{GeH}_3)_2$ and Ge_2H_6 . Film thicknesses are 670 and 490 nm for the optical and electrical samples, respectively. After growth, the optical sample was annealed at 830 °C for 30 min in a hydrogen-rich environment which was proven to enhance the PL intensity.

$\text{Ge}_{1-y}\text{Sn}_y/\text{Si}$ Sample Growth

A set of $\text{Ge}_{1-y}\text{Sn}_y$ ($y = 0.03\% - 3.6\%$) films were grown directly on a high resistivity *n*-Si(100) substrate using ultra-high vacuum chemical vapor deposition (UHV-CVD) and were produced by means of the reaction of Ge_2H_6 and SnD_4 at temperatures ranging from 385 to 320 °C and a pressure of 0.30 Torr, with the lower temperatures being used for the higher Sn content samples. This growth method resulted in film thicknesses ranging from 300 to 900 nm.

$\text{Ge}_{0.90}\text{Si}_{0.08}\text{Sn}_{0.02}$ Sample Growth

The $\text{Ge}_{0.90}\text{Si}_{0.08}\text{Sn}_{0.02}$ films were grown on a *p*-Ge(100) (6° miscut) substrate using the UHV-CVD method via reactions of Ge_2H_6 , Si_3H_8 , and SnD_4 at a temperature of 370 °C and a pressure of 0.3 Torr and resulted in film thicknesses ranging from 600 to 900 nm.

Post-Growth Characterization

The Sn and Si contents as well as the film thicknesses were measured using RBS. For the doped samples, *in situ* *p*- and *n*- type doping of B and P atoms was achieved using the single-source precursors of B_2H_6 and $\text{P}(\text{GeH}_3)_3$, respectively. Dopant levels as high as $1 \times 10^{19} \text{ cm}^{-3}$ were measured using spectroscopic ellipsometry, Hall Effect measurements, and SIMS. After growth, the $\text{Ge}_{1-y}\text{Sn}_y$ and $\text{Ge}_{0.90}\text{Si}_{0.08}\text{Sn}_{0.02}$ samples underwent three cycles of RTA for 10 s each at temperatures ranging from 700 to 625 °C in order to reduce the levels of threading defects and to relax the strain in the epitaxial layers. HRXRD measurements were used to determine the residual strain in the films. The strain was initially slightly compressive but changed to tensile after annealing and ranged from 0.16% for the *p*- $\text{Ge}_{1-y}\text{Sn}_y$ /*n*-Si (1.0% Sn) sample to 0.22% for the *n*- $\text{Ge}_{1-y}\text{Sn}_y$ /*n*-Si (0.3% Sn) sample. XTEM was used to examine the overall film quality as well as the film substrate interface. Periodic dislocations were observed near the interface. However, they remained localized and no dislocation cores were observed propagating into the film. AFM measurements of the annealed layers showed smooth surfaces, void of any defects.

Photoluminescence

A schematic diagram of the photoluminescence set-up is shown in Figure 1. PL measurements were performed using a tunable Ti-Sapphire laser set to 830 nm pumped by an Ar-ion laser at 514 nm. The laser was focused using an $f = 4 \text{ cm}$ aspheric achromatic doublet lens with a NIR anti-reflective coating for maximum power and minimum spot size. A focused spot size of $50 \mu\text{m}$ was achieved using the Ti-Sapphire laser. The power incident on the sample was varied using a neutral density filter which was placed directly in front of the output of the laser. For the PL emission, collimating lenses were used to collect the light from the sample and

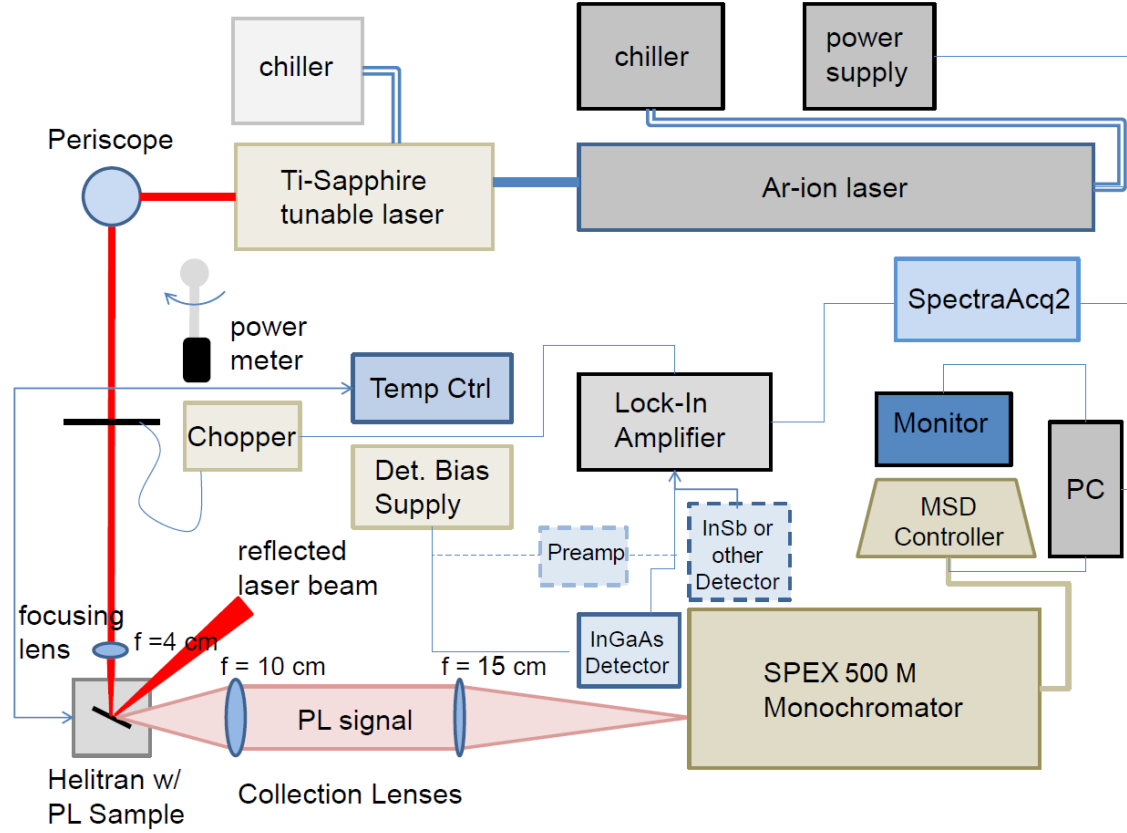


Figure 1. Schematic diagram of photoluminescence experimental setup. Not shown are vacuum pump, helium dewar and Helitran[®] transfer tube, N₂ tank and purging tubes.

focus it onto the entrance slit of a SPEX 500M (f/4) monochromator. The luminescence was dispersed using a 600 groove/mm ruled diffraction grating blazed at 1.6 μm . After passing through the exit slit of the monochromator, the PL signal was focused onto a TE-cooled, wavelength-extended InGaAs detector (2.05 μm cutoff). To further improve the signal-to-noise ratio, the signal was then passed through an SR850 lock-in amplifier which was used in conjunction with an SR540 optical chopper run at 200 Hz. For temperature-dependent PL measurements, the sample was mounted to the cold finger of an ARS-Cryo Helitran[®] continuous flow liquid-helium cryostat equipped with two Si-diode temperature sensors. The sample temperature was varied from 10 K to 300 K using a LakeShore model 331

temperature controller. A slit width of 3 mm and resolution of 1-2 nm was used for all measurements along with a lock-in time constant of 0.3 s. The system response was observed to be fairly uniform over the spectral range studied and so the measured PL intensity was not corrected. However, in order to ensure the accuracy of the measured peak positions, the system was calibrated using a spectral lamp and this wavelength correction was applied to all of the PL data. Results of the PL measurements are presented in a later section.

Hall-Effect and Etching Studies

A schematic diagram of the Hall-effect measurement system is shown in Figure 2. Hall-effect measurements were made using the standard Van der Pauw technique. Ohmic contacts were formed on the 4 corners of a 5×5 mm sample using either indium solder or metal contacts with Cr(200 Å)/Au(2000 Å) deposited using an e-beam evaporator. The temperature-dependent measurements were performed using a LakeShore 7704 Hall Measurement System (HMS). A typical magnetic field of 5 kG and excitation currents ranging from 50 μ A to 1.0 mA were used. The samples were mounted on a sapphire substrate for electrical isolation which was then mounted on the copper cold-finger of a closed-cycle cryostat operating at a temperature range of 10 – 300 K. Electrical contact was made using small diameter wires which were connected to copper posts on the cold finger and were then soldered using indium to the contacts on the sample.

A separate LakeShore 7704 system equipped with a high-temperature oven was used for measurements from 300 to 800 K. This system used pressurized tungsten probes for electrical contact with a similar sapphire-on-copper mount for electrical isolation and thermal contact. To improve measurement accuracy, the magnetic field was measured at the pole and at the sample position for both systems. Both

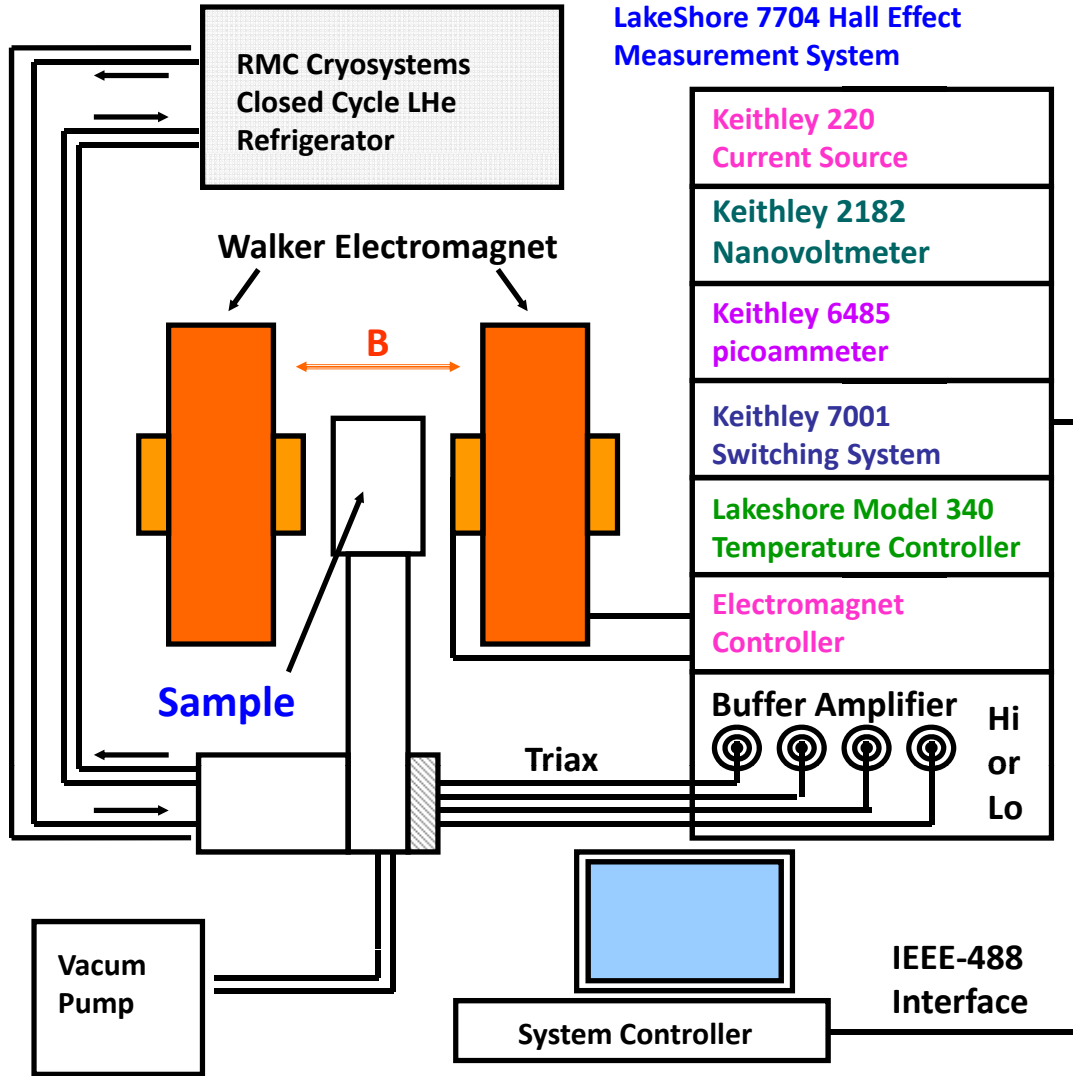


Figure 2. Schematic diagram of the Hall-effect measurement system

sets of data were then corrected using their respective magnetic field ratio, the details of which are described in Appendix A.

For samples with conductive substrates, the electrical properties of the substrate were independently measured using the substrate samples provided. The properties of the epilayers were then extracted from the data using a multi-layer model which included effects from the interfacial region. To validate the multi-layer model and more accurately determine the properties of the epilayers alone, etch studies were

performed for selected samples. Temperature-dependent Hall-effect measurements were performed after each etch. A wet etch method was used for these samples with a selective etchant of $\text{HCl}:\text{H}_2\text{O}_2:\text{H}_2\text{O}$ mixed in a 1:1:20 ratio which was shown not to etch the Si substrate. Etch rates of approximately 60 and 30 nm/min were observed for the $\text{Ge}_{1-y}\text{Sn}_y$ and $\text{Ge}_{0.90}\text{Si}_{0.08}\text{Sn}_{0.02}$ samples, respectively. The slightly slower etch rate observed for the ternary alloy is expected due to the Si content. In addition to the sample used for the Hall measurements, a second, reference sample was employed to enable an accurate measurement of the etch depth. Standard photolithography techniques were used to define a 500 μm -wide open strip on the reference sample, which was exposed and etched. The Hall sample and the reference sample were etched at the same time, after which the remaining photoresist was removed from the reference sample and the etch depth was measured using a Tencor stylus profilometer. To simplify the process, In contacts were used. They were shown not to be significantly effected by the etchant and maintained their ohmic behavior after etching. Unfortunately, this limited the measurements to the low temperature system (10 – 300 K), however, this still allowed for the observation of the degenerate conduction and shallow and deep acceptors. Results of the Hall-effect measurements and etch studies are presented in a later section.

IV. Results and Discussion

Optical Characterization

PL of Ge/*p*-Si(100)

In addition to the $\text{Ge}_{1-y}\text{Sn}_y$ samples, a Ge reference sample was grown as described in the previous chapter. Temperature dependent PL measurements were performed and the results are shown in Figure 3a [31]. The main peak near 0.852 eV (0.770 eV) at 20 K (300 K) is attributed to direct-gap (E_D) emission while the weaker broad peak near 0.701 eV at 20 K (almost unobservable at RT) is assigned to the indirect-gap (E_{ID}) emission. The integrated PL intensity of the E_D emission peak is very strong for 20 K < T < 50 K. The intensity then decreases gradually with increasing T up to around 150 K then starts to increase again from 150 K to 300 K. It is interesting to note that the intensity of the E_D peak is larger than that of the E_{ID} peak at all temperatures. This is probably due in part to the photo-excitation of electrons out of the valence band directly into the Γ -valley of the conduction-band which is possible with a laser wavelength of 830 nm (1.49 eV). As a result, a large number of non-thermalized electrons could be trapped in the Γ valley which could lead to strong, direct-gap emission. Also, it is important to mention that the strong E_D PL intensity observed here indicates that the effect of self absorption is not significant for this thin *p*-Ge/*p*-Si film in contrast to the case of bulk Ge [19].

The broad weak peak assigned to E_{ID} emission at 20 K consists of two peaks centered at 0.737 and 0.701 eV, which are attributed to no phonon (NP) and transverse optical (TO) phonon related emission, respectively. The separation between these two peaks agrees very well with the accepted value of 36 meV for the TO phonon energy [32]. These assignments are consistent with previously reported PL peak positions [32, 33]. For example, Wagner and Via [33] reported PL peaks at

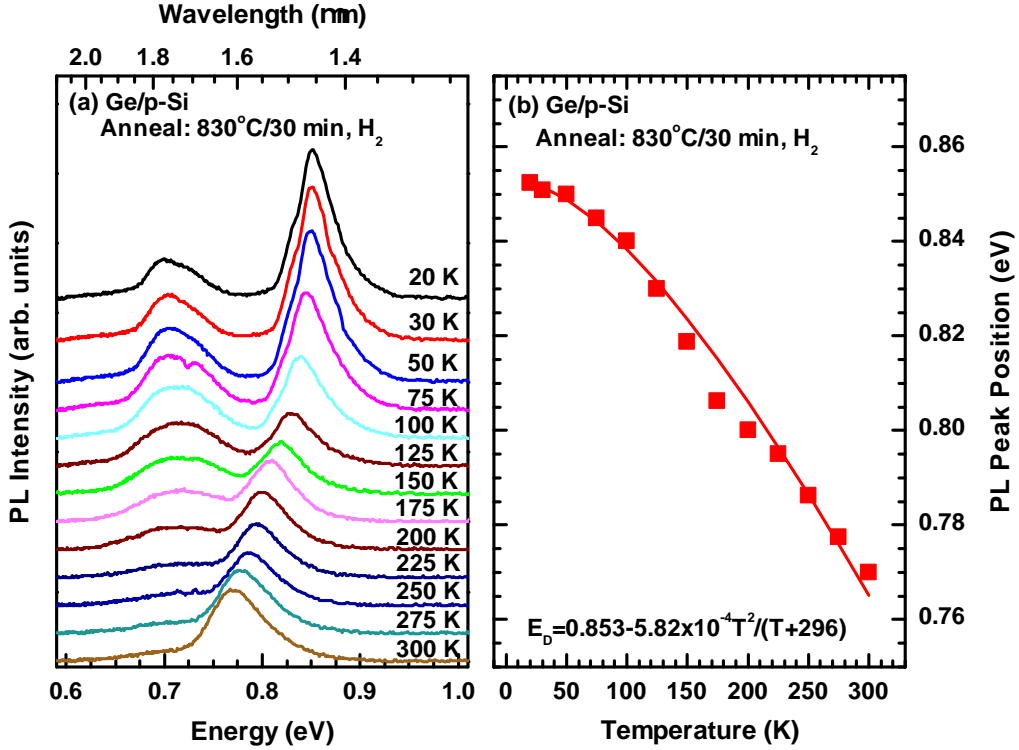


Figure 3. a. Temperature-dependent PL measurements of Ge/*p*-Si(100) b. Peak positions (scatter) obtained from Gaussian fitting along with a Varshni curve (solid line) fit to the data (equation shown in figure).

0.736 and 0.710 eV at 5 K for bulk Ge (*p*-type doped with Ga at $\approx 10^{19} \text{cm}^{-3}$), which were attributed to NP and longitudinal acoustic (LA) phonon related emission, respectively. It is not surprising to observe different phonon related PL peaks from different samples, since they depend on the nature and properties of each individual sample.

The Gaussian fit of the E_{ID} PL peak shows that the intensities of these two peaks increase with T up to around 100 K with the NP peak increasing more rapidly than the TO peak. This fact, along with the influence of the nearby E_D PL peak, actually causes the broad E_{ID} PL peak to appear blue-shifted as T increases, but a more careful analysis shows that both the NP and TO peaks are in fact red-shifted.

As T increases above around 100 K, the two peaks converge and appear as one broad peak with rapidly decreasing PL intensity up to around 250 K, with almost no observable intensity at RT.

The fitted peak positions for the E_D PL emission are plotted as a function of temperature from 20 to 300 K in Fig. 3b. Unfortunately, the T -dependent $E_{ID}(T)$ PL peaks could not be determined reliably due to the lack of clear PL peaks at higher T s. The solid fitting curve for $E_D(T)$ was calculated as a function of T using a Varshni type equation [34] with $E_D(T) = E_D(0) - \alpha T^2 / (T + \beta)$, where $E_D(0) = 0.853$ eV, $\alpha = 5.82 \times 10^{-4}$ eV/K, and $\beta = 296$ K (the same as those for bulk Ge) [1]. The calculated values agree very well with the PL data as shown in Fig. 3b with the exception of the intermediate T region, where the influence of the E_{ID} PL peak obscures the accurate estimation of E_D .

A schematic band diagram (not scaled) for this tensile strained p -Ge/ p -Si sample are plotted in Figure 4 along with the observed PL peak energies (E_D and E_{ID}) at 20 K. The room temperature strain value for this samples was 0.19% as measured by XRD, however at lower temperatures the strain should increase due to the thermal expansion mismatch between the Ge and the Si substrate. To quantify this, the thermal expansivities of Si and Ge were calculated and used to determine the strain in the epilayer at low temperatures. More details of this calculation can be found in Appendix C.

The compositional dependence of the $\text{Ge}_{1-y}\text{Sn}_y$ band gaps were calculated using a standard quadratic equation of the form:

$$E_{i,\text{GeSn}}(y, T) = yE_{i,\text{Sn}} + (1 - y)E_{i,\text{Ge}}(T) - y(1 - y)b_i(T) \quad (6)$$

where $i = \Gamma, L$, and $E_{i,\text{Ge}}$ and $E_{i,\text{Sn}}$ are the band gaps for pure Ge and α -Sn given by Refs [1, 22, 35]. Bowing parameters of $b_\Gamma(0 \text{ K}) = 2.55$ eV and $b_L(0 \text{ K}) = 0.89$ eV

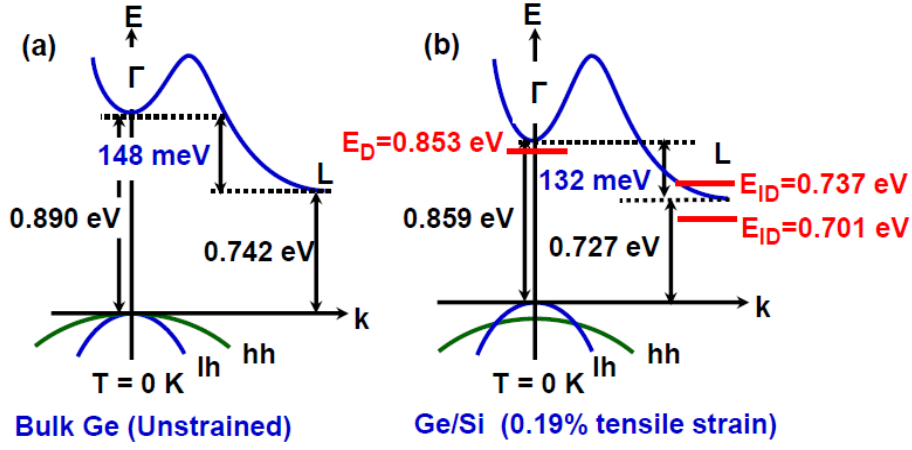


Figure 4. Simple band diagrams (not scaled) for (a) bulk Ge at 0 K, (b) 0.19% tensile strained p -Ge/ p -Si samples at 0 K, respectively, plotted along with the observed PL peak energy positions at each temperature.

were used for low temperatures, while bowing parameters of $b_{\Gamma}(300 \text{ K}) = 1.95 \text{ eV}$ and $b_L(300 \text{ K}) = 0.68 \text{ eV}$ were used for room temperature. These bowing parameters represent a compilation of the best estimates available in the literature, including those obtained from theoretical and experimental methods [13, 22, 36]. On the other hand, this choice of bowing parameters is believed to be the cause of some of the observed discrepancies between the experimental results and theoretically calculated values, indicating that further study of these bowing parameters is probably required. Additionally, the behavior of the bowing parameter at intermediate temperature is not well known, therefore the analysis should be restricted to low temperature (0 K) and room temperature (300 K). Finally, the effect of strain was calculated using the deformation potential theory of Van de Walle [3]. More details of these band structure calculations can be found in Appendix B.

The $E_{\Gamma}(0)$ for the p -Ge/ p -Si sample is expected to be reduced to 0.859 eV from the value of 0.890 eV in bulk Ge at 0 K due to 0.19% tensile strain as shown in

Figs. 4(a) and 4(b). However, the estimated value of $E_D(0) = 0.853$ eV from the T-dependent PL peak energies shown in Fig. 4(b) for p -Ge/ p -Si sample is slightly smaller by about 6 meV than the predicted value of 0.859 eV, which implies that the $E_\Gamma(0) [\approx E_D(0)]$ reduction in Γ conduction valley minimum might be a little larger than the theory predicted. On the other hand, the indirect bandgap at 0K, $E_L(0) [\approx E_g(0)]$, which is defined as the difference between the L-valley minimum and the up-shifted light-hole valence band maximum, is expected to be reduced to 0.727 eV for this p -Ge/ p -Si sample, compared to the value of 0.742 eV in bulk Ge. However, the observed PL peak energy of the NP peak at 20 K ($E_{ID}(20)$) is 0.737 eV for this sample, which is actually slightly higher (by about 10 meV) than the predicted value of 0.727 eV, implying that the actual bandgap, $E_L(0)$, could be as high as 0.737 eV. This indicates that the reduction in the indirect bandgap might be smaller than the theory predicted.

For this sample, the estimated energy separation between the Γ and L valleys at 0 K, $[E_\Gamma(0) - E_L(0)]$, could be about 116 meV ($= 0.853 - 0.737$ eV), which is smaller (by about 16 meV) than the theoretically predicted value of 132 meV. This difference could be due in part to the larger tensile strain expected at lower temperatures due to the thermal expansion mismatch between Ge and Si, however it could also indicate a slightly larger reduction of the energy gap with tensile strain than what the theory predicted. Similarly, the direct bandgap (not shown in Fig 4) at RT is expected to be reduced to 0.769 eV compared to the value of 0.800 eV in bulk Ge. The observed PL peak energy ($E_D(300)$) is 0.770 eV for this sample. Strictly speaking however, the actual band gap is lower than the PL peak energy by a ‘Boltzman’ factor of $kT/2$ (≈ 13 meV at 300 K). If this additional correction is taken into account, then $E_\Gamma(300)$ could be about 0.757 eV which is just slightly smaller (by about 12 meV) than the predicted value of 0.769 eV. Unfortunately, the

indirect PL peak energy ($E_{ID}(300)$) at RT could not be observed as seen in Fig. 3. Thus, an accurate estimate of the indirect bandgap at RT was not possible for this sample. Therefore, a reliable estimate of the energy separation $E_T(300)$ - $E_L(300)$ could not be obtained through PL measurements.

PL of n -Ge_{0.997}Sn_{0.003}/ n -Si(100)

The T-dependent PL spectra of a P-doped ($1.5 \times 10^{19} \text{ cm}^{-3}$) n -type Ge_{0.997}Sn_{0.003} sample grown on an n -Si substrate are shown in Figure 5a. The as-grown sample showed no measurable PL, but after an RTA treatment at 725 °C , a strong PL signal was observed as shown in the figure. The improved PL intensity has been attributed to a reduction in the number of nonradiative recombination centers achieved by the annealing process. The strong main peak near 0.711 eV at 5 K is associated with the E_{ID} transition. At present, the exact nature of this PL peak could not be determined, i.e. whether it is no phonon, acoustic, or optical phonon related. The integrated PL intensity of this E_{ID} emission decreases continuously as T increases from 5 to 225 K, and by 300 K the peak has almost entirely disappeared due to the prevailing non-radiative recombination.

Another strong broad peak was observed at 0.720 eV at RT for this sample, which is attributed to the direct-gap (E_D) emission. The E_D PL intensity decreases continuously as the T decreases from 300 to 100 K, and then it disappears as T decreases further as shown in the figure. Since this sample is heavily n -type doped with phosphorus at $1.5 \times 10^{19} \text{ cm}^{-3}$, a higher electron population in the direct Γ valley caused by thermalization at RT is expected due to both the indirect L valley states filling effect [4] and photo-excitation. Thus, very strong E_D emission is expected from this sample. Still, the PL intensity of the E_D emission at RT of this sample is not as strong as expected. Interestingly, the sample does show very strong

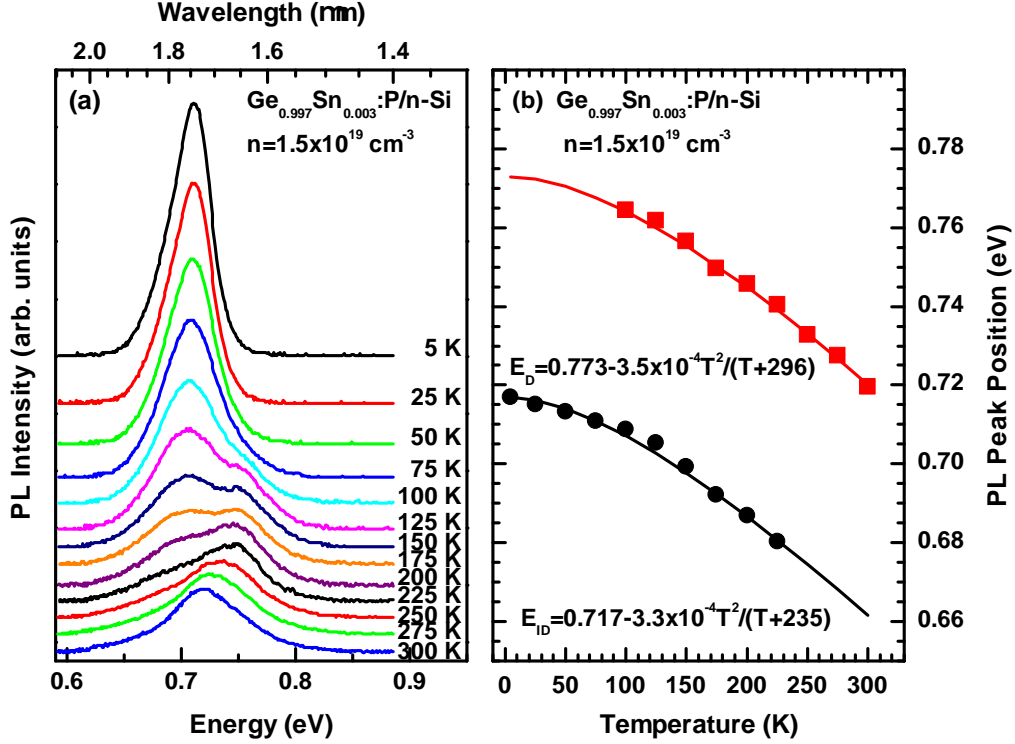


Figure 5. (a) Temperature-dependent PL spectra of the P-doped $n\text{-Ge}_{0.997}\text{Sn}_{0.003}$ grown on $n\text{-Si}$ substrate. (b) Direct (E_D ; red squares) and indirect (E_{ID} ; black circles) bandgap related PL peak energies plotted as a function of temperature from 5 to 300 K. The red and black fitting curves are the calculated direct (E_D) and indirect (E_{ID}) bandgap related energies, respectively, plotted as a function of temperature using Varshni equation.

E_{ID} PL at low temperature (LT). The intensity of E_D PL peak of this sample decreases as T decreases possibly at the expense of an increase in the E_{ID} PL intensity. This is the opposite behavior of the $p\text{-Ge}/p\text{-Si}$ sample where the E_D intensity increases as T decreases. The PL results from both samples clearly show the competitiveness between the E_D and E_{ID} PL transitions as T changes.

The PL peak positions of E_D at RT and E_{ID} at LT are well defined, but their positions at intermediate temperatures are not. However, two distinct peaks are very clearly observed at a temperature of about 150 K. In order to separate the two

peaks, each set of T-dependent PL data was fit with two Gaussian peaks, one for E_D (red solid squares) and one for E_{ID} (black solid circles) wherever possible. The results of these fits are plotted in Fig. 5b as a function of T from 5 to 300 K. The calculated T-dependent $E_D(T)$ for this sample (red solid line) is given by:

$$E_D(T) = 0.773 - 3.5 \times 10^{-4}T^2/(T + 296)(\text{eV}) \quad (7)$$

For bulk Ge, the T-dependence of the direct bandgap (E_Γ) is given by:

$E_\Gamma(T) = 0.89 - 5.82 \times 10^{-4}T^2/(T + 296)$ [37]. This tells that the observed $E_D(T)$ changes at a much slower rate than in case of bulk Ge as T increases. The black solid line is the calculated T-dependent $E_{ID}(T)$ and is given by

$$E_{ID}(T) = 0.717 - 3.3 \times 10^{-4}T^2/(T + 235) \quad (8)$$

For bulk Ge, the T-dependence of the energy gap (E_g) is given by

$E_g(T) = 0.742 - 4.8 \times 10^{-4}T^2/(T + 235)$ [37]. This again indicates that the observed $E_{ID}(T)$ changes more slowly than E_g in bulk Ge as T increases as was the case with the direct bandgap, although the difference here is less.

Schematic band diagrams (not scaled) for this 0.22% tensile strained $n\text{-Ge}_{0.997}\text{Sn}_{0.003}/n\text{-Si}$ samples are plotted in Fig. 6 along with the observed PL peak energies of E_D and E_{ID} at LT and 300 K. At 0 K, the $E_\Gamma(0)$ and $E_L(0)$ for the $n\text{-Ge}_{0.997}\text{Sn}_{0.003}/\text{Si}$ sample are expected to be reduced to 0.843 and 0.721 eV, respectively, due to the combination of 0.22% tensile strain and 0.3% Sn content as shown in Fig. 6a. However, the extrapolated PL peak energy at 0 K, $E_D(0)$ [$\approx E_\Gamma(0)$], is 0.773 eV as shown in Fig. 5b, which is about 70 meV smaller than the predicted value of 0.843 eV. Also, note here that the $E_D(0)$ of 0.773 eV for this sample occurred at a photon energy that is about 80 meV lower than the $E_D(0)$ of

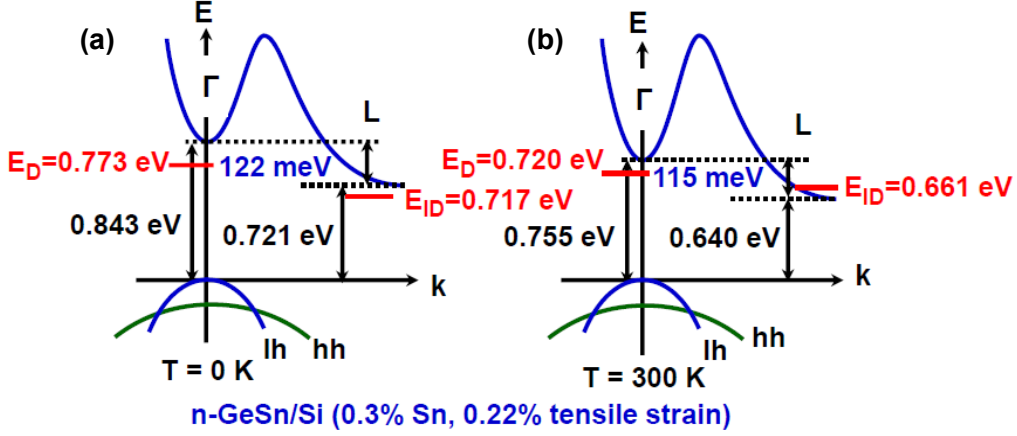


Figure 6. Simple band diagrams (not scaled) for 0.22% tensile strained n - $\text{Ge}_{0.997}\text{Sn}_{0.003}/\text{Si}$ sample at (a) 0 and (b) 300 K, respectively, plotted along with the observed PL peak energy positions at each temperature.

0.853 eV for the p -Ge/ p -Si. This difference is most likely due to the 0.3% Sn content, considering the fact that the strain is about the same for both samples. There could also be some bandgap narrowing due to the heavy doping, but it is not clear at this point. There are conflicting reports on this topic in the literature. Haas [38] (and others) observed a red-shift in the absorption edge of bulk n -Ge with increased doping (up to about $4 - 5 \times 10^{19} \text{ cm}^{-3}$). However, Sun et al [4] performed RT PL measurements on a series of n -type, tensile-strained Ge layers grown on Si substrates and saw no shift in the emission wavelength with increasing doping concentration (up to about $1 \times 10^{19} \text{ cm}^{-3}$). For this reason, bandgap narrowing (BGN) is not included in most of the analysis.

On the other hand, the value of the $E_{ID}(0)$ derived from the fit to the T-dependent data is 0.717 eV for this sample, which is just slightly less (by about 4 meV) than the predicted value of 0.721 eV. Assuming that this PL peak at 0 K is due to phonon emission rather than phonon absorption, $E_L(0)$ could range from

0.717 to 0.753 eV for this sample using energies of 0 meV for the NP and 36 meV for TO phonon, respectively. So the estimated value of the energy separation $[E_T(0)-E_L(0)]$ obtained through PL measurements would be less than or equal to 56 meV ($=0.773-0.717$ eV), which is much smaller than the theoretically calculated separation of 122 meV.

At RT, $E_T(300)$ and $E_L(300)$ are expected to be reduced to 0.755 and 0.640 eV, respectively, for this $n\text{-Ge}_{0.997}\text{Sn}_{0.003}/\text{Si}$ sample. Although the measured PL peak energy, $E_D(300)$, is 0.720 eV, if the $kT/2$ factor is taken into account, $E_T(300)$ could be 0.707 eV, which is much smaller (by about 48 meV) than the predicted value of 0.755 eV. Also, note here that the measured $E_D(300)$ of 0.720 eV for this sample is about 50 meV lower than the $E_D(300)$ of 0.770 eV for the $p\text{-Ge}/p\text{-Si}$, which again could be mainly due to the 0.3% Sn content. In the mean time, for the indirect bandgap, the extrapolated $E_{ID}(300)$ is 0.661 eV for this sample, which is higher than the predicted value of 0.640 eV. However, it is a lot more difficult to discuss the relationship between the PL peak energies and the actual bandgap because the observed $E_{ID}(300)$ PL peak at RT may be due to no-phonon, phonon absorption, or phonon emission processes.

In addition, this heavy n -type P-doping may also fill up the conduction band above the $E_L(300)$ minimum in addition to possible band tailing. Also, according to the theory for bandgap narrowing [39], at a doping level of $1.5 \times 10^{19} \text{ cm}^{-3}$ the L-valley minimum would be reduced by about 30 meV at RT. Therefore, all of these factors could affect the observed $E_{ID}(300)$ PL peak energy as well as $E_D(300)$. Since the $[E_T(300)-E_L(300)]$ would not be affected by the common factor of $kT/2$, it has not been included in this discussion.

While the exact nature of the $E_{ID}(300)$ PL peak cannot be determined, it is possible to estimate bandgap values given the different cases and therefore come up

with a range of possible energies for $E_L(300)$. First, if the measured PL is no-phonon related, then $E_L(300)$ would simply be 0.661 eV. Second, if the measured PL peak is phonon emission related, then $E_L(300)$ could range from 0.669 to 0.697 eV, using phonon energies of 8 meV and 36 meV for the TA and TO phonons, respectively. Third, if the measured PL peak is phonon absorption related, which is very unlikely, then $E_L(300)$ could range from 0.653 to 0.625 eV, using the same phonon energies. Therefore, for this sample, the estimated value of $[E_T(300)-E_L(300)]$ through PL measurements could be about 59 meV ($= 0.720 - 0.661$ eV) for NP related, between 23 and 51 meV for phonon emission, and between 67 and 95 meV for phonon absorption, depending on the nature of the phonons involved. These are all compared to the theoretically calculated reduced energy separation of 115 meV.

PL of $p\text{-Ge}_{0.99}\text{Sn}_{0.01}/n\text{-Si}(100)$

Another sample to show strong RT PL was a B-doped ($1 \times 10^{19} \text{ cm}^{-3}$) $p\text{-Ge}_{0.99}\text{Sn}_{0.01}$ sample grown on an $n\text{-Si}$ substrate. The measured layer thickness was 585 nm. The sample was subjected to 3 cycles of RTA for 10 s each at 750 °C. The temperature-dependent PL spectra for this sample are shown in Figure 7a. The small peak near 0.688 eV at 20 K is associated with the E_{ID} transition. At low temperature (LT), this sample does not show very strong E_{ID} PL at all which is in stark contrast to the $n\text{-Ge}_{0.997}\text{Sn}_{0.003}/n\text{-Si}$ sample. Due to the very weak signal, an exact analysis of this PL peak could not be made, i.e. whether it is no phonon, acoustic, or optical phonon related. As was the case with the Ge/Si and the $n\text{-Ge}_{0.997}\text{Sn}_{0.003}/n\text{-Si}$ samples, the integrated PL intensity of this E_{ID} emission decreases continuously as T increases from 20 to 225 K, and by 300 K the peak has almost entirely disappeared. Again this is due to the prevailing non-radiative recombination which effectively quenches the emission at higher temperatures.

Another stronger peak was observed at 0.716 eV at RT for this sample, which is

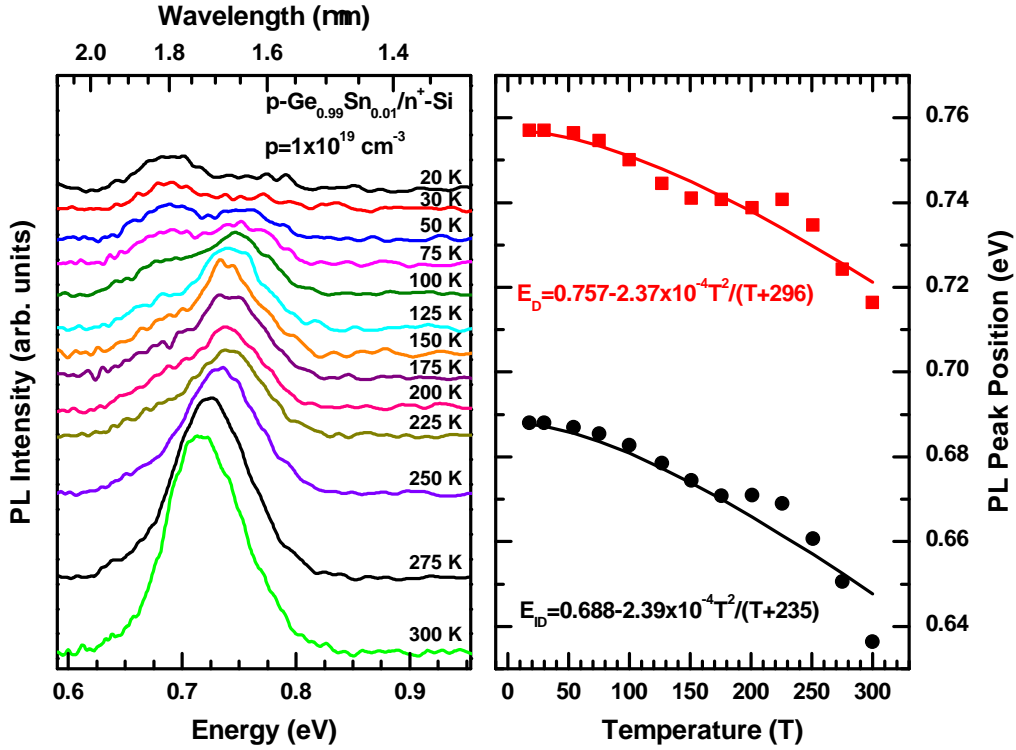


Figure 7. (a) Temperature-dependent PL spectra of a B-doped $p\text{-Ge}_{0.99}\text{Sn}_{0.01}/n\text{-Si}$ sample. (b) Direct (E_D ; red squares) and indirect (E_{ID} ; black circles) bandgap related PL peak energies plotted as a function of temperature from 20 to 300 K.

attributed to the direct-gap (E_D) emission. The PL intensity of the E_D peak decreases continuously with decreasing T from 300 to about 75 K and appears only as a very weak peak at 20 K. Since this sample is fairly heavily p -type doped with boron at $1.0 \times 10^{19} \text{ cm}^{-3}$, a larger hole population in the valence band is expected. Since the laser photon energy used was 1.49 eV (830 nm), a sufficient number electrons would be excited directly into the Γ -valley in the conduction band, which should resulting in very strong E_D emission. That being said, the observed PL intensity of this sample is not as strong as expected. In fact it is weaker than the PL intensities of both the other two samples previously studied. The intensity of

E_D PL peak does decrease as T decreases which again may be at the expense of an increase in the E_{ID} PL intensity. However the effect is much less for this sample since the E_{ID} intensity doesn't increase that much. It is also worth noting here that this is the opposite behavior of the Ge/*p*-Si sample where the E_D intensity increases as T decreases. While the PL intensity from different samples cannot be compared directly, we can examine the relative intensities. For this sample the E_D (300 K) intensity is much larger (by about a factor of 6.6) than the E_{ID} (20 K) intensity. However, for the n -Ge_{0.997}Sn_{0.003} sample the E_{ID} (5 K) intensity is larger (by a factor of about 2.4) than the E_D (300 K) intensity. It is unclear whether this difference is due to the Sn content or n -type versus p -type doping. Nevertheless, the PL results for this p -Ge_{0.99}Sn_{0.01} sample also clearly show the competitiveness between the E_D and E_{ID} PL transitions.

The PL peak positions of E_D at RT and to a lesser extent E_{ID} at LT are well defined, but their positions at intermediate temperatures are not. However, two distinct peaks can clearly be seen at temperatures around 50-75 K. In order to separate the two peaks, each set of T-dependent PL data was fit with two Gaussian peaks as described earlier, one for E_D (red solid squares) and one for E_{ID} (black solid circles) wherever possible. The results of these fits are plotted in Fig. 7b as a function of T from 20 to 300 K. The calculated T-dependent $E_D(T)$ for this sample (red solid line) is given by $E_D(T) = E_D(0) - \alpha T^2/(T + \beta)$, where $E_D(0) = 0.757$ eV, $\alpha = 2.37 \times 10^{-4}$ eV/K, and $\beta = 296$ K. For bulk Ge, the T-dependence of the direct bandgap (E_Γ) is given by $E_\Gamma(T) = 0.89 - 5.82 \times 10^{-4} T^2/(T + 296)$ [37]. This tells that the observed $E_D(T)$ changes at a much slower rate than in case of bulk Ge.

The black solid line is the calculated T-dependent $E_{ID}(T)$ and is given by $E_{ID}(T) = E_{ID}(0) - \alpha T^2/(T + \beta)$, where $E_{ID}(0) = 0.688$ eV, $\alpha = 2.39 \times 10^{-4}$ eV/K, and $\beta = 235$ K. For bulk Ge, the T-dependence of the energy gap, E_g , is given by

$E_g(T) = 0.742 - 4.8 \times 10^{-4}T^2/(T + 235)$ [37]. This again indicates that the observed $E_{ID}(T)$ changes more slowly than $E_g(T)$ in bulk Ge as T increases as was the case with the direct bandgap, although again the difference here is less.

Schematic band diagrams (not scaled) for this 0.16% tensile strained $p\text{-Ge}_{0.99}\text{Sn}_{0.01}/n\text{-Si}$ samples are plotted in Fig. 8 along with the observed PL peak energies of E_D and E_{ID} at LT and 300 K. As with the previous discussions, all

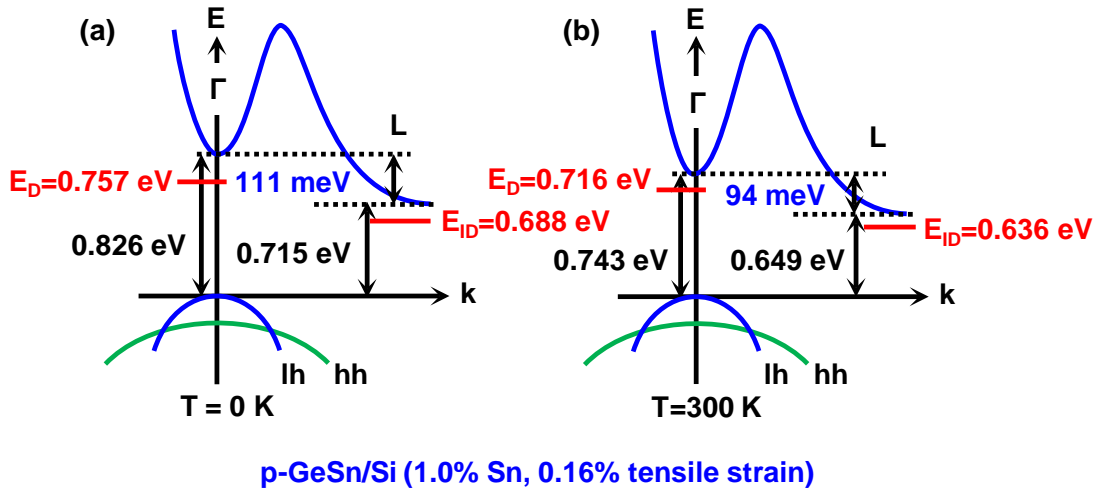


Figure 8. Simple band diagrams (not scaled) for 0.16% tensile strained $p\text{-Ge}_{0.99}\text{Sn}_{0.01}/\text{Si}$ sample at (a) 0 and (b) 300 K, respectively, plotted along with the observed PL peak energy positions at each temperature.

calculated bandgap values given are for transitions from the conduction band to the upshifted light-hole valence band. At 0 K, the direct ($E_{\Gamma}(0)$) and indirect ($E_L(0)$) bandgaps for this $p\text{-Ge}_{0.99}\text{Sn}_{0.01}/\text{Si}$ sample are expected to be reduced to 0.826 and 0.715 eV, respectively. This is due to a combination of the 1.0% Sn content and 0.16% tensile strain. However, the extrapolated PL peak energy at 0 K, $E_D(0)$ [$\approx E_{\Gamma}(0)$], is 0.757 eV as seen in Fig. 7b, which is about 69 meV smaller than the predicted value of 0.826 eV. Also, note here that the $E_D(0)$ of 0.757 eV for this sample occurred at a photon energy that is about 96 meV lower than the $E_D(0)$ of

0.853 eV for the p -Ge/ p -Si. Considering that the strain is somewhat less for this sample, this difference could actually be larger and is most likely due to the 1.0% Sn content. There could also be some additional bandgap reduction due to the heavy doping, but that is not included in this analysis.

As for the indirect gap, the value of the $E_{ID}(0)$ derived from the fit to the T-dependent data is 0.688 eV for this sample, which is less (by about 27 meV) than the predicted value of 0.715 eV. Assuming that this PL peak at 0 K is due to phonon emission and not phonon absorption, the actual bandgap $E_L(0)$ could range from 0.688 to 0.724 eV for this sample using energies of 0 meV for the NP and 36 meV for TO phonon, respectively. So the estimated value of the energy separation $[E_{\Gamma}(0)-E_L(0)]$ obtained through PL measurements would be less than or equal to 69 meV ($=0.757-0.688$ eV), which is much smaller than the theoretically calculated separation of 111 meV. Also note that this is larger than the separation of 56 meV obtained for the n -Ge_{0.997}Sn_{0.003} sample, probably due to the lower tensile strain in this sample.

At RT, $E_{\Gamma}(300)$ and $E_L(300)$ are expected to be reduced to 0.743 and 0.649 eV, respectively, for this p -Ge_{0.99}Sn_{0.01}/Si sample. With the $kT/2$ factor taken into account, $E_{\Gamma}(300)$ could be about 0.703 eV, which is much smaller (by about 40 meV) than the predicted value of 0.743 eV. Also, the measured $E_D(300)$ of 0.716 eV for this sample is about 54 meV lower than the $E_D(300)$ of 0.770 eV for the p -Ge/ p -Si, which could be mainly due to the 1.0% Sn content. Meanwhile, for the indirect bandgap, the extrapolated $E_{ID}(300)$ is 0.636 eV, which is just slightly lower (by about 13 meV) than the predicted value of 0.649 eV. As mentioned earlier, it is much more difficult to discuss the relationship between the PL peak energies and the actual bandgap because the observed $E_{ID}(300)$ PL peak at RT may be due to no-phonon, phonon absorption, or phonon emission processes. For this sample, the

very weak E_{ID} PL signal at RT also makes determining the bandgap difficult.

However, a range of possible energies can be determined similar to what was done previously for the $n\text{-Ge}_{0.997}\text{Sn}_{0.003}$ sample. So $E_L(300)$ would be 0.636 eV for the no-phonon case, and would range from 0.644 to 0.672 eV for phonon emission, and from 0.628 to 0.600 eV for phonon absorption, using the same phonon energies of 8 and 36 meV for the TA and TO phonons, respectively. Therefore, for this sample, the estimated value of the Γ -L separation [$E_\Gamma(300)$ - $E_L(300)$] through PL measurements could be about 80 meV ($=0.716\text{-}0.636$ eV) for NP related, between 44 and 72 meV for phonon emission, and between 88 and 116 meV for phonon absorption, depending on the nature of the phonons involved. These are all compared to the theoretically calculated reduced energy separation of 94 meV.

PL of $n\text{-Ge}_{1-y}\text{Sn}_y/n\text{-Si}(100)$ (0.3% - 3.6% Sn)

A set of $n\text{-Ge}_{1-y}\text{Sn}_y$ samples with Sn contents ranging from 0.3% to 3.6% were also studied. A summary of the RT properties of these samples are shown in Table 1. The film thicknesses were measured using RBS, the strain using HRXRD, and the carrier concentration using Hall-effect measurements. As seen in the table, the strain in the films decreases with increasing Sn content, starting as highly tensile and changing to slightly compressive for the 3.6% Sn sample. This is caused partly by an increased lattice mismatch between the $\text{Ge}_{1-y}\text{Sn}_y$ layer and the Si substrate, creating a larger amount of compressive strain in the as-grown films. It could also be caused by the decrease in annealing temperature with increasing Sn content which is necessary to prevent Sn segregation in these samples. This lower temperature results in less strain relaxation during the annealing process and therefore the strain state of the film remains more compressive (or less tensile). The normalized room temperature PL spectra of these selected samples are shown in

Figure 9. The measured PL peak energies are plotted as black circles in the inset of Fig. 9 as a function of Sn concentration. A clear decrease in the emission peak energy with increasing Sn content is observed, however the decrease is not as large as expected. Table 2 shows the measured peak positions compared with two sets of theoretically or empirically calculated values. The first set of values, shown as red squares in the inset of Fig. 9, was theoretically calculated using the effects of Sn and strain. The second set of values, shown as green triangles in the inset of Fig. 9, were obtained to include the effect of band gap narrowing (BGN) due to heavy doping in addition to the theoretically calculated values.

Table 1. Various properties of selected $n\text{-Ge}_{1-y}\text{Sn}_y/n\text{-Si}$ samples studied ($y < 0.036$). All samples were annealed three times for 10 s at the temperatures indicated using RTA.

Sn (%)	Film Thickness (nm)	Annealing Temp. ($^{\circ}\text{C}$)	Strain (%)	Carrier Conc. (cm^{-3})
0.3	890	725	-0.22	1.5×10^{19}
1.6	520	625	-0.12	1.6×10^{19}
1.9	500	625	-0.11	1.5×10^{19}
3.2	380	550	-0.05	1.2×10^{19}
3.6	320	500	0.072	1.2×10^{19}

Table 2. Measured RT PL peak positions of selected $n\text{-Ge}_{1-y}\text{Sn}_y/n\text{-Si}$ samples ($y < 0.036$) compared with two sets of theoretically or empirically calculated values including: 1. the effect of Sn and strain only 2. the effect of Sn, strain, and doping.

Sn (%)	Measured PL Peak Position (eV)	Calculated Peak Position ¹ (eV)	Difference (meV)	Calculated Peak Position ² (eV)	Difference (meV)
0.3	0.7113	0.7684	-57.1	0.7404	-29.1
1.6	0.7031	0.7445	-41.4	0.7155	-12.4
1.9	0.6896	0.7369	-47.3	0.7089	-19.3
3.2	0.6730	0.7070	-34.0	0.6820	-9.0
3.6	0.6658	0.7147	-48.9	0.6897	-23.9

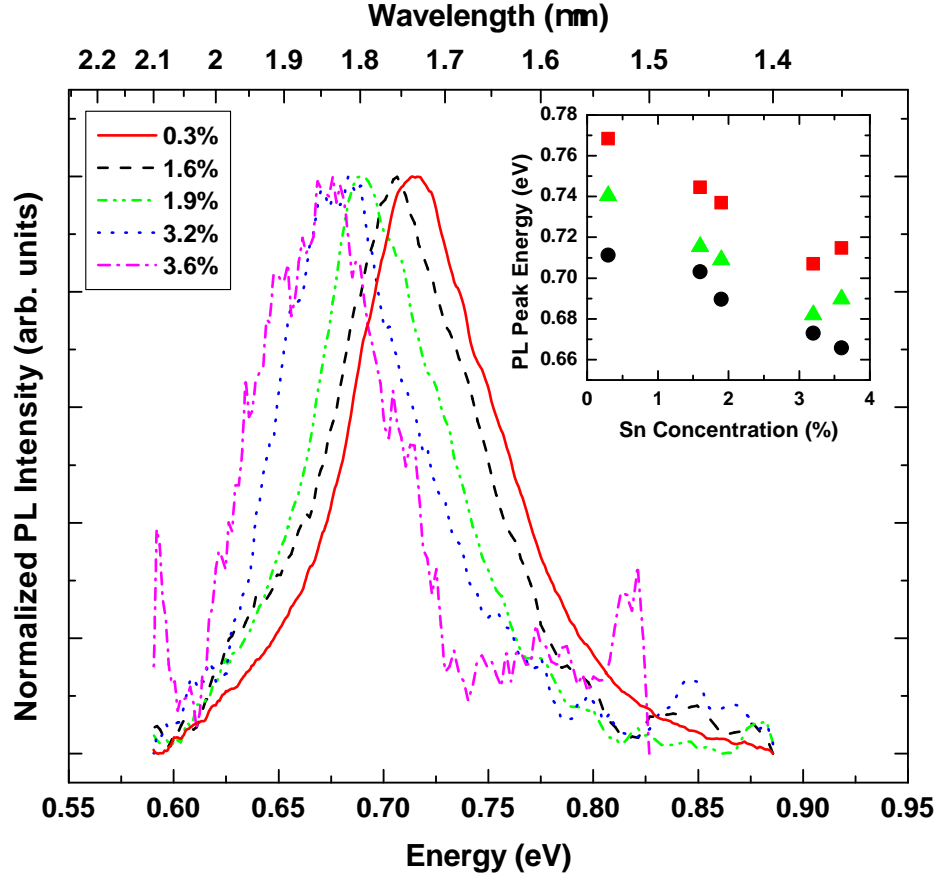


Figure 9. Normalized room temperature PL spectra of P-doped $n\text{-Ge}_{1-y}\text{Sn}_y/n\text{-Si}$ samples. The inset shows the PL peak positions (black circles) plotted as a function of Sn concentration along with two sets of theoretically or empirically calculated peak positions. The first set (shown as red squares) was theoretically calculated with the effects of Sn and strain. The second set (shown as green triangles) was calculated using the effects of Sn, strain, and doping, with the empirical formula in Eqn. (9) used for the doping effect.

The results of Camacho-Aguilera et al [40] were used here to calculate the BGN. They measured the RT PL spectra of a set of n -Ge/Si samples with a wide range of doping concentrations. They observed a redshift in the emission wavelength with increasing doping, but only for samples with P concentrations greater than $1 \times 10^{19} \text{cm}^{-3}$. They used the following, semi-empirical, linear equation to describe the BGN of the direct gap:

$$E_g(N_D = 0) - E_g = E_{BGN} + \Delta_{BGN} N_D \text{ (cm}^{-3}\text{)}, \quad (9)$$

where N_D is the doping concentration, E_{BGN} is the BGN turn-on offset energy reduction (intercept at $N_D = 0$); and Δ_{BGN} is the BGN coupling parameter (slope of the linear fit). They obtained values of 0.013 eV and $10^{-21} \text{ eV/cm}^{-3}$ for E_{BGN} and Δ_{BGN} , respectively. Note that this equation is only valid for $N_D > 10^{19} \text{cm}^{-3}$. For the sake of clarity, Eqn. 9 is plotted as a function of doping concentration in Figure 10.

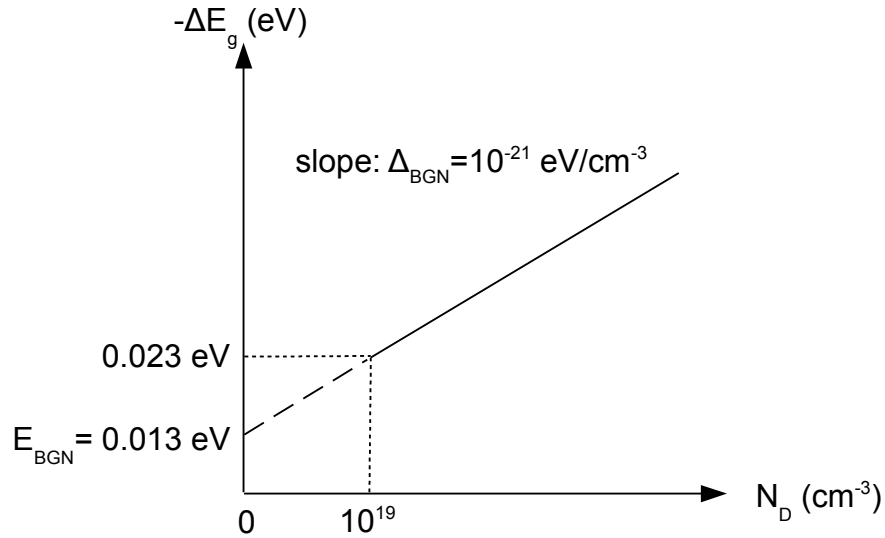


Figure 10. Representative diagram for bandgap narrowing (BGN) in Ge using the empirical expression in Eqn. (9) derived by Camacho-Aguilera et al. The linear increase in bandgap reduction as a function of doping concentration is shown.

For these $\text{Ge}_{1-y}\text{Sn}_y$ samples with P concentrations in the range of $1.2 - 1.6 \times 10^{19} \text{ cm}^{-3}$, the BGN was determined to be about $20 - 30 \text{ meV}$, which is significant. As seen in the inset of Fig. 9, the inclusion of BGN greatly improved the agreement between the calculated and measured values, however there was still some offset. These offsets could indicate a larger band gap reduction caused by the Sn, which would result in a larger (negative) bowing parameter. However, if the bowing parameter was the cause, we would expect a larger error for larger Sn concentrations, but the offsets seem to be relatively constant for all the samples. In fact, the offset for the 0.3% Sn sample was a little larger than the others which is opposite of the expected result. Therefore a larger bowing parameter can be reasonably ruled out. The data could also indicate a larger deformation potential constant is needed in the strain calculation. The value used in this work was -9.48 which was obtained from Van de Walle [3]. More recently, J. Liu et al [41] calculated the deformation potential constants of Ge from the photoreflectance (PR) data of tensile-strained Ge/Si samples and compared their values with a large number of values found in the literature. The literature values varied from -8.0 to -11.5 and the value determined by Liu et al [41] from the PR data was -8.97. So then a larger value of this constant is possible, but it is not very likely.

A more probable cause of the observed discrepancies is a higher sample temperature than what was read from the temperature sensor. The samples were mounted to a cold finger, but the measurements were made at RT without using any liquid nitrogen or helium to actively cool the sample. Because of that, and because of the relatively high laser power of 500 mW used, significant local sample heating probably occurred. During the PL measurements, the temperature read by the thermocouple on the cold finger typically only fluctuated by a few degrees (usually 2 or 3 K). However the actual sample temperature probably changed much

more significantly. An increase in the sample temperature would lower the band gap and therefore could help to largely explain why the measured direct bandgap PL peak positions are lower than the calculated values. To quantify this, we can take the average offset between the measured and calculated values and use the Varshni equation obtained for the 0.3% Sn sample to approximately calculate the actual sample temperature, assuming that the change in the bandgap is only due to a change in temperature. Differentiating Eqn. 7, we get:

$$\frac{d}{dT}E_D(T) = \frac{0.35T^2}{(296 + T)^2} - \frac{0.7T}{296 + T} \quad (\text{meV/K}) \quad (10)$$

Multiplying both sides by dT , we obtain:

$$dE_D(T) = \left(\frac{0.35T^2}{(296 + T)^2} - \frac{0.7T}{296 + T} \right) dT \quad (\text{meV/K}) \quad (11)$$

Strictly speaking, we should integrate this expression. However looking at the plot of $E_D(T)$ in Fig. 5b we can see that it is fairly linear in this temperature range ($T > 250$ K). So we can choose a value for T , say 300 K, set the left-hand side equal to the average offset which was -18.7 meV, and solve for dT . Doing so, we obtain:

$$dT = -18.7 \left/ \left(\frac{0.35 \times 300^2}{(296 + 300)^2} - \frac{0.7 \times 300}{296 + 300} \right) \right. \approx 71K \quad (12)$$

and so the true sample temperature could be about 371 K. This is a rough calculation, but it does give a pretty good idea of what the temperature would have to be in order to explain the observed offset, and the result is not unbelievable.

The un-normalized PL spectra for these samples are shown in Figure 11. The integrated intensities of the PL peaks are plotted as a function on Sn concentration in the inset of Fig. 11. As seen in the figure, the PL intensity decreases with

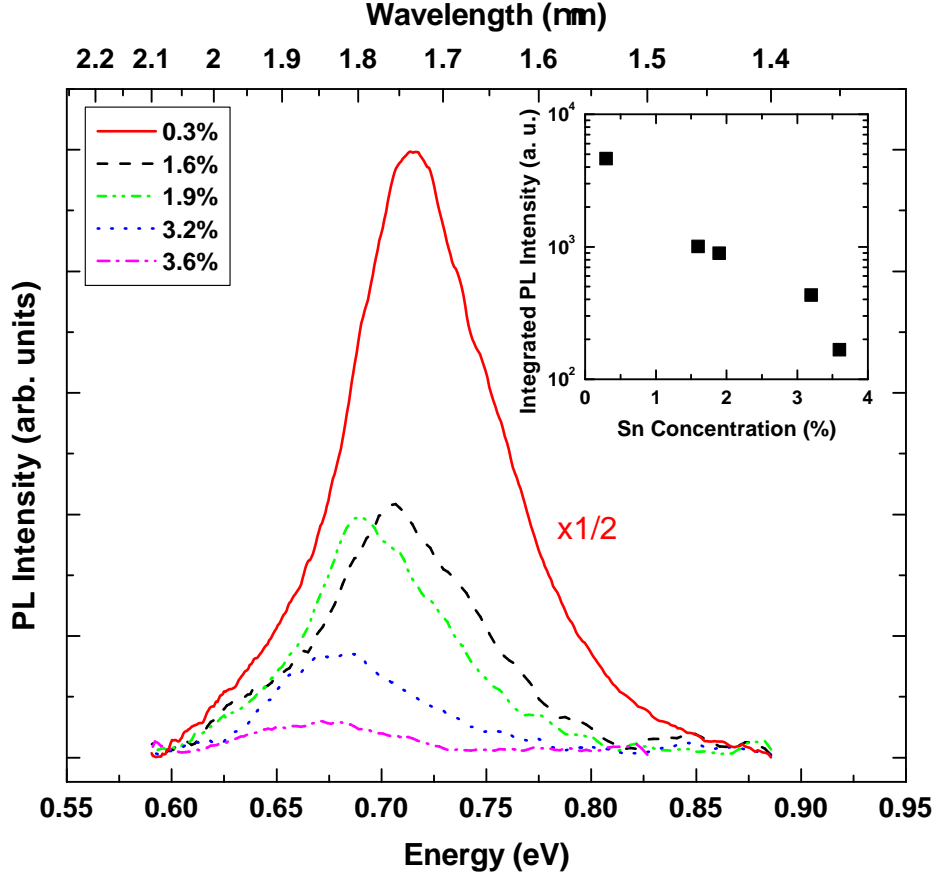


Figure 11. (a) Unnormalized room temperature PL spectra and (b) the integrated PL intensity of P-doped $n\text{-Ge}_{1-y}\text{Sn}_y$ samples plotted as a function of Sn concentration.

increasing Sn content which is unexpected. In theory, the higher Sn content samples should have a smaller Γ -L separation and therefore should show stronger direct-gap luminescence. There are a few possible explanations for this observed decrease in intensity. One is the lower annealing temperature used for the higher Sn content alloys. As mentioned previously, this was necessary to prevent the segregation of Sn atoms in the layers. Recall that the as-grown, unannealed samples did not show any measurable PL at all and that the annealing treatment was shown to improve the overall quality of the samples and relax the (compressive) strain in the epilayer. It is likely that annealing at lower temperatures did not improve the quality of the films

as much as annealing at higher temperatures and therefore those samples showed less PL intensity. Another reason could be the slightly lower n -type carrier concentration for the 3.2% and 3.6% Sn samples. Sun et al [4] observed a superlinear dependence of the integrated PL intensity as a function of n -type doping concentration. Based on their results, the intensity difference between samples with carrier concentrations of $1.2 \times 10^{19} \text{cm}^{-3}$ and $1.5 \times 10^{19} \text{cm}^{-3}$ would be about 30%, with all other factors being equal. The difference in integrated PL intensity between the 1.9% and 3.2% Sn samples was about 52%. So the difference in doping could be responsible for a majority of the change in intensity. The other $\approx 22\%$ may be due to the lower annealing temperature of 550°C used for the 3.2% Sn sample as opposed to 625°C used for the 1.9% Sn sample.

Electrical Characterization

Hall-Effect Measurements of p -Ge, p -Ge_{1-y}Sn_y (0.06–0.10% Sn), and p -Ge_{0.882}Si_{0.090}Sn_{0.028} Samples Grown on n -Si Substrates

Temperature dependent Hall measurements were carried out for a set of p -Ge, p -Ge_{1-y}Sn_y (0.06-0.10% Sn), and p -Ge_{0.882}Si_{0.090}Sn_{0.028} samples grown on n -Si substrates using the evaporated Cr/Au contacts described earlier. A summary of the measured electrical properties of these samples at room temperature is given in Table 3 and the temperature dependent results are shown in Figures 12–14 [42]. The sheet carrier concentration is plotted on a log scale as a function of inverse temperature ($1000/T$) in Fig. 12. On the left, in Fig. 12a, the entire temperature range is shown with a split in the axis near 300 K and an expanded scale used in the high temperature regime where the carrier concentration changes more rapidly. Fig. 12b is an enlarged plot of the low-to-mid temperature regime which is used to show the two distinct slopes in the data which are believed to correspond to shallow and deep acceptors.

Table 3. Summary of Hall-effect data for p -Ge, p -Ge_{1-y}Sn_y, and p -Ge_{0.882}Si_{0.090}Sn_{0.028} samples measured at room temperature.

Sn (%)	Thickness (nm)	Carrier Concentration (cm ⁻³)	Mobility μ (cm ² /V-s)	Conductivity (Ω -cm) ⁻¹
0.00	490	5.90×10^{16}	721	4.27
0.06	800	2.97×10^{16}	345	1.17
0.10	1100	1.76×10^{16}	357	0.77
2.80	550	2.19×10^{16}	212	4.80

The first notable feature of this data is the fairly constant low-temperature carrier density of about $1.61 \times 10^{11} - 3.64 \times 10^{12} \text{ cm}^{-3}$ depending on the sample. This indicates the presence of a parallel conduction path which is degenerate (i.e.

temperature independent) in nature. There are a few possible sources of this degenerate conduction including: a surface conducting layer [43–45], impurity band conduction [46, 47], and a conducting layer in the region near the film-substrate interface [48, 49]. Surface conduction in *p*-type materials must involve an *n*-type electron accumulation layer. In other words, the surface state is always opposite in type to the rest of the material. Since this material and the degenerate conducting layer are both *p*-type, a surface layer can reasonably be ruled out as the source of the degenerate conduction. Impurity band conduction only occurs at high doping levels ($N > 10^{18} \text{ cm}^{-3}$). Since these samples were either unintentionally or very lightly doped, impurity band can also be excluded as the cause of the degenerate conduction. On the other hand, there is some evidence to suggest that an interfacial layer may be the cause. As mentioned earlier, XTEM images revealed periodic misfit dislocations at the interface which served to partially relieve the strain caused by the lattice mismatch (4% for $y < 0.1\%$) between the Ge or $\text{Ge}_{1-y}\text{Sn}_y$ and the Si substrate. These defects, if present in a high enough density, and distributed throughout the interfacial region, could serve as a conducting channel and therefore be the cause of the observed parallel degenerate conducting layer.

Above about 50 K, the carriers start to increase slowly as seen in the right-hand side of Fig. 12b which corresponds to the ionization of shallow acceptors believed most likely to be boron. As the temperature increases further, the carriers begin to increase more rapidly as seen in the left-hand side of Fig. 12b where a definitive change in the slope is observed. This is believed to be caused by the activation of another, deeper acceptor, the origin of which is unknown at present. As temperature continues to increase above room temperature, the carriers increase even more quickly until they reach singularities near 370 – 440 K, depending on the sample, at which point the observed conductivity changes from *p*-type to *n*-type. A

zero Hall coefficient has also been previously reported in lightly B-doped p -Si (10^{12} cm^{-3}) [50], B-doped p -SiGeC thin film grown on n^- -Si substrate [51], and an unintentionally doped p -InSb grown on GaAs substrate [43]. After initially decreasing, the n -type carriers then start to increase very rapidly in the intrinsic regime. Another important detail to note is that the sheet carrier density of the Si has become appreciable at these higher temperatures and could have an influence on the measured carrier density.

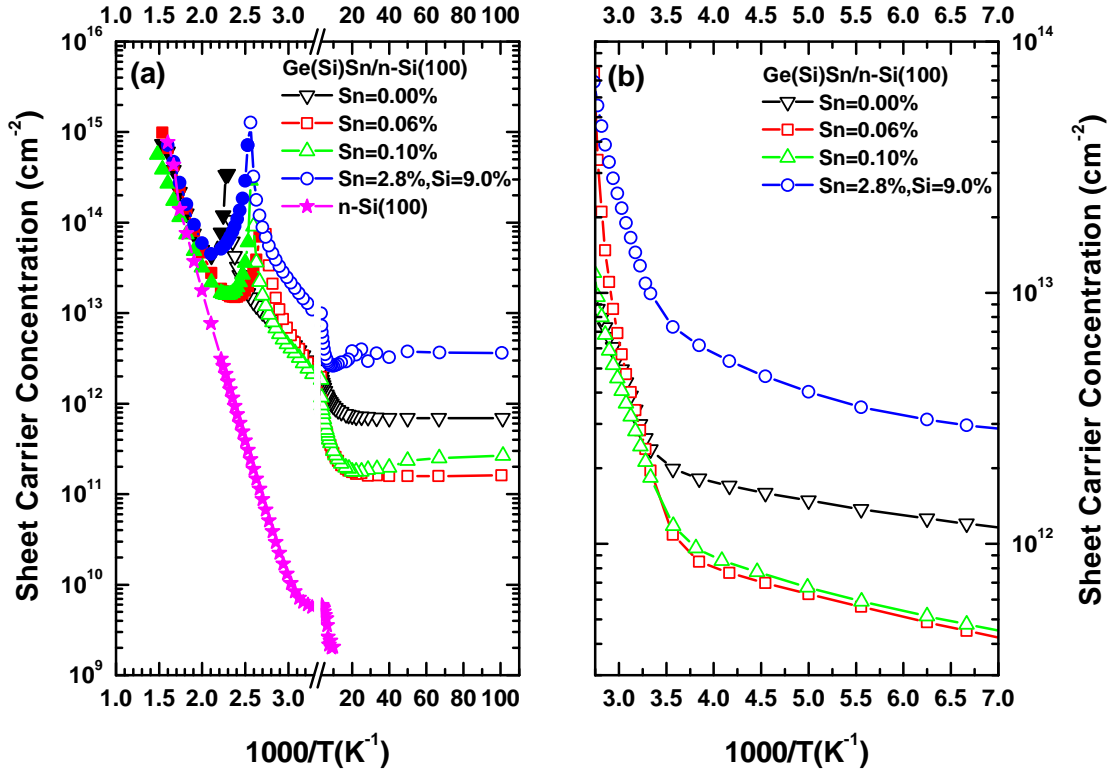


Figure 12. Sheet carrier concentration plotted as a function of inverse temperature for Ge, $\text{Ge}_{1-y}\text{Sn}_y$, and $\text{Ge}_{0.882}\text{Si}_{0.090}\text{Sn}_{0.028}$ films along with the n -Si substrate; for (a) all temperatures and (b) lower temperatures. Open symbols indicate p -type conductivity, while closed symbols indicate n -type conductivity.

It is well known that when both holes, p , and electrons, n , are present in a semiconductor, the Hall coefficient in the low magnetic field limit is given by [52]:

$$R_H = \frac{p - b^2 n}{e(p + bn)^2}, \quad (13)$$

where e is the electron charge and $b = \mu_e/\mu_h$, where μ_e and μ_h are the electron and hole mobility, respectively. At low temperatures, the intrinsic carriers, n_i , freeze out, and the extrinsic p -type conduction becomes dominant for a p -type semiconductor. As temperature increases above room temperature, intrinsic carriers come into play for narrow bandgap materials like the current $\text{Ge}_{0.9994}\text{Sn}_{0.0006}$ and Ge samples, going through $R_H = 0$ when $p = b^2 n = bn_i$ where $ni^2 = np$. As the temperature increases beyond the $R_H = 0$ point, where $p < b^2 n$ or $p < bn_i$, the contribution from the intrinsic electrons will become dominant because of their higher mobility (for the case when $\mu_e > \mu_h$), giving rise to an apparent n -type conduction in the Hall measurements. More specifically, when we assumed all acceptors, N_A , and donors, N_D , are ionized then the total hole concentration can be written as $p(T) = [N_A - N_D] + n_i^2(T)/p(T) = [N_A - N_D] + n_i(T)/b$. Thus the semiconductor may act as an apparent n -type material for $n_i \geq [N_A - N_D]b/(b^2 - 1)$.

An accurate quantitative explanation for the change in the conductivity type for the current sample is not a simple matter due to the many unknown variables of involving multiple conducting layers of $p\text{-Ge}_{1-y}\text{Sn}_y$ layer, p -interfacial layer, and $n\text{-Si}$ substrate. Furthermore, in the high temperature region, the contribution of both intrinsic electrons and holes as well as their mobilities from $p\text{-Ge}_{1-y}\text{Sn}_y$ and $n\text{-Si}$ substrate should also be taken into account for the conductivity type conversion along with those from the extrinsic carriers. In principle, if we knew all the necessary values for the epitaxial layer as well as the other conducting layers involved, then the type conversion temperature could be reasonably well predicted,

but unfortunately, many of those parameters are unknown for the current sample. However, in order to have an idea of conductivity type conversion for this Ge-like $p\text{-Ge}_{0.9994}\text{Sn}_{0.0006}/n\text{-Si}$ sample, a simplified calculation is illustrated here by neglecting the effects of intrinsic carriers and mobilities of $n\text{-Si}$ substrate, and deep acceptor concentration and mobility. If we assume some reasonable values of parameters such as $\mu_e/\mu_h = 2.13$ (used the same value as bulk Ge [53]) and $[N_A - N_D] \approx 5 \times 10^{15} \text{ cm}^{-3}$ for the $\text{Ge}_{1-y}\text{Sn}_y$ layer, then the p - to n -type conversion ($R_H = 0$) would occur for $n_i \approx [N_A - N_D]b/(b^2 - 1) = 3 \times 10^{15} \text{ cm}^{-3}$, which corresponds to the value of intrinsic carriers in Ge (GeSn) at around 426 K. This value is roughly comparable with the observed type-conversion temperature of 370 K for the Ge-like $p\text{-Ge}_{0.9994}\text{Sn}_{0.0006}$. Note here that as shown in Fig. 12a, the effect of $n\text{-Si}$ substrate in the high temperature region could be significant, and it could further bring down the type conversion temperature.

The mobility is plotted as a function of temperature in Figure 13. This Ge/Si sample had the highest mobility of all the samples with a maximum value of 2,096 $\text{cm}^2/\text{V-s}$ at 90 K and a modest room temperature value of 669 $\text{cm}^2/\text{V-s}$ which is about 1/3 of the value for bulk Ge with similar hole concentrations. This reduction is most likely due to carrier scattering at the Ge-Si interface. The mobility is observed to decrease with increasing Sn content for all temperatures. The peak of the mobility also shifts to higher temperatures with increased Sn. This may be due to alloy scattering or scattering at the interface. Samples with more Sn content will have a larger equilibrium lattice constant, and therefore a greater mismatch with the Si substrate. This could lead to more dislocations at the film-substrate interface. If scattering at the interface is at least partially caused by these dislocations, then the scattering could increase with Sn content and therefore help to explain the observed decrease in Hall mobility.

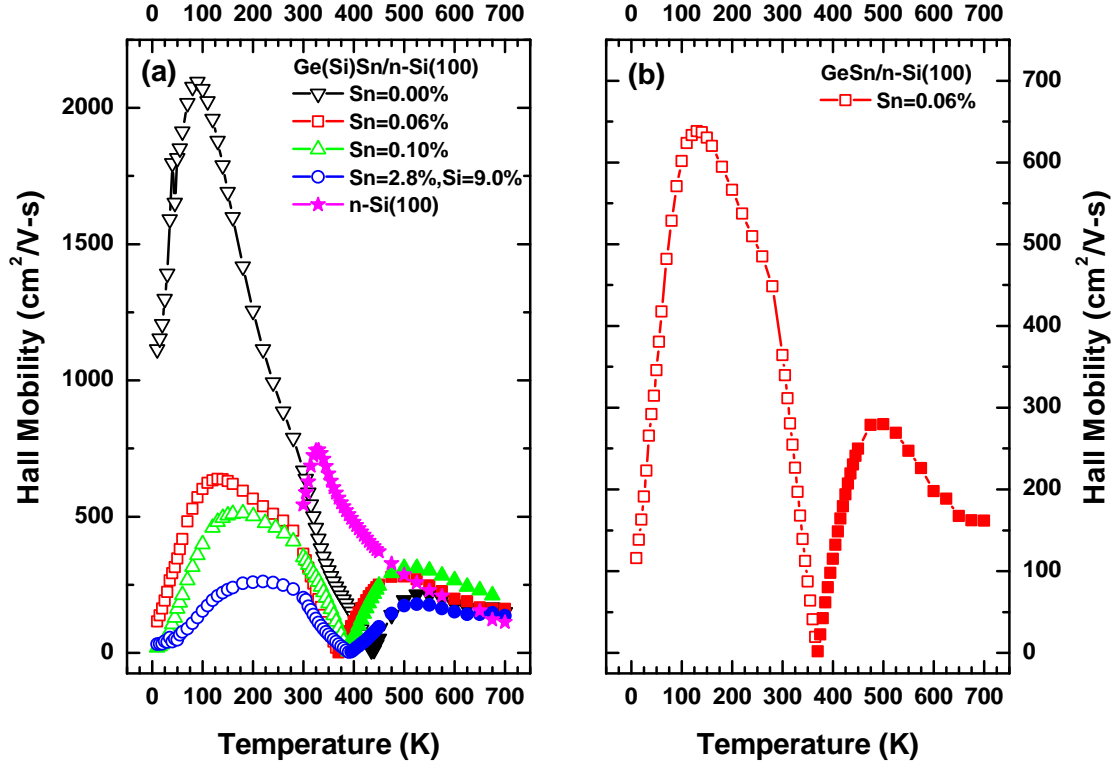


Figure 13. Carrier mobility plotted as a function of temperature for Ge, Ge_{1-y}Sn_y, and Ge_{0.882}Si_{0.090}Sn_{0.028} films along with the *n*-Si substrate; for (a) all samples and (b) for the Ge_{1-y}Sn_y (0.06% Sn) sample. Open symbols indicate *p*-type conductivity, while closed symbols indicate *n*-type conductivity.

As temperature continues to increase the mobility exhibits a kink around 280 K which coincides fairly well with the onset of the deep acceptor ionization seen in the carrier concentration plot. After that point, the mobilities decrease rapidly and eventually goes to zero at the singularity (i.e. when $R_H=0$). The mobility then increases and reaches a peak around 550 K after which it decreases slowly up to 700 K. The observed deviations from pure ionized impurity and lattice scattering are believed to be caused by the addition of alloy scattering [36] as well as carrier scattering near the interface. A detailed analysis of the temperature dependence of the mobility for the Ge_{0.9994}Sn_{0.0006} sample can be found in the next section.

The mobility is observed to decrease with increasing Sn content for all temperatures. The peak of the mobility also shifts to higher temperatures with increased Sn. This may simply be due to alloy scattering however that is not the only factor that depends upon Sn content. Samples with more Sn content will have a larger equilibrium lattice constant, and therefore a greater lattice mismatch with the Si substrate. This larger mismatch could lead to more strain in the film which could cause more dislocations to form in an attempt to relieve that strain. So if the scattering at the interface is at least partially caused by these dislocations, then the scattering could increase with Sn content and therefore help to explain the observed decrease in Hall mobility.

The log of the conductivity is plotted as a function of inverse temperature in Figure 14 [42]. Fig. 14a shows the entire temperature range and Fig. 14b shows an expanded scale of the high temperature range. Again, the degenerate behavior is obvious at low temperatures as shown in the right side of Fig. 14a. At low T, the relative values of the conductivity differ somewhat from those of the carrier concentration. For example, the Ge/Si sample shows the highest degenerate conductivity, whereas the $\text{Ge}_{0.882}\text{Si}_{0.090}\text{Sn}_{0.028}$ sample showed the highest degenerate carrier concentration. This can be explained by the much higher mobility of the Ge/Si sample. Recall that for a *p*-type semiconductor, the conductivity can be expressed as $\sigma = pe\mu_h$ where *p* is the hole concentration and μ_h is the hole mobility. The carrier density of the Ge/Si sample was about 5 times smaller than that of the $\text{Ge}_{0.882}\text{Si}_{0.090}\text{Sn}_{0.028}$ sample (6.93×10^{11} as a function of $3.64 \times 10^{12} \text{ cm}^{-3}$), but its mobility was about 35 times greater (1,113 as a function of $31 \text{ cm}^2/(\text{V-s})$). Therefore, the low-T conductivity of the Ge/Si sample is larger than that of the $\text{Ge}_{0.882}\text{Si}_{0.090}\text{Sn}_{0.028}$ sample. For the $\text{Ge}_{1-y}\text{Sn}_y$ (0.06-0.1% Sn) samples, a similar reversal is observed, i.e. the degenerate conductivity of the $\text{Ge}_{0.9994}\text{Sn}_{0.0006}$ sample is

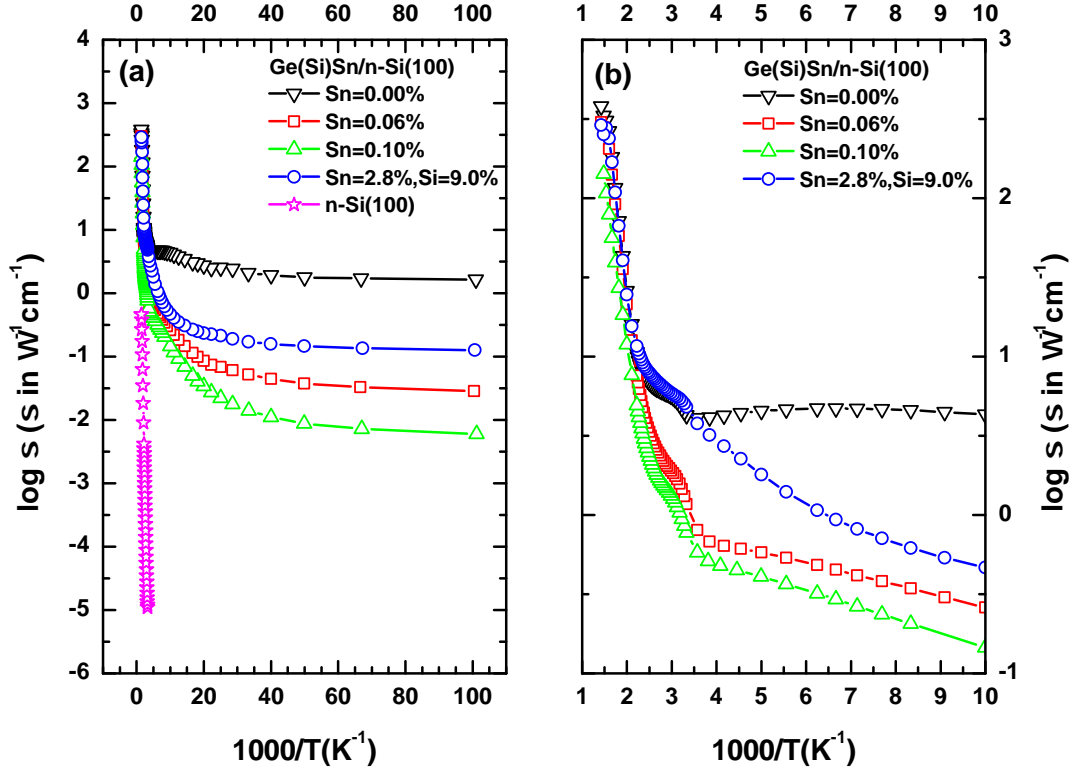


Figure 14. Log conductivity plotted as a function of inverse temperature for Ge, $\text{Ge}_{1-y}\text{Sn}_y$, and $\text{Ge}_{0.882}\text{Si}_{0.090}\text{Sn}_{0.028}$ films along with the n -Si substrate; for (a) all temperatures and (b) high temperatures.

larger than that of the $\text{Ge}_{0.999}\text{Sn}_{0.001}$ sample even though the carrier concentration was smaller. This can also be explained by the mobility. The carrier density of the $\text{Ge}_{0.9994}\text{Sn}_{0.0006}$ sample was about 1.6 times smaller than that of the $\text{Ge}_{0.999}\text{Sn}_{0.001}$ sample (1.61×10^{11} as a function of $2.67 \times 10^{11} \text{ cm}^{-3}$), but its mobility was about 5.8 times greater (116 as a function of $20 \text{ cm}^2/(\text{V}\cdot\text{s})$) which results in the larger conductivity. It also is easy to see the onset of the deep acceptors around 280 K in Fig. 14b. The conductivities of all the different samples converge in the intrinsic region which is more clearly visible in the left side of the Fig. 14b.

Analysis of the $p\text{-Ge}_{1-y}\text{Sn}_y/n\text{-Si}$ (0.06% Sn) Sample

Two-Layer Model

In order to extract the electrical properties of the $\text{Ge}_{0.9994}\text{Sn}_{0.0006}$ layer alone, a simple two-layer conducting model was applied for temperatures below the type conversion where the contribution from the Si substrate was negligible. As shown in Fig. 12, for temperatures below the singularity, only carriers in the epitaxial and degenerate parallel conducting layers are significant, whereas for the temperatures above the singularity, intrinsic carriers from both the $\text{Ge}_{1-y}\text{Sn}_y$ and Si layers are significant. As shown in Fig. 12b, the hole concentration, p_1 , in the $\text{Ge}_{1-y}\text{Sn}_y$ layer consists of both shallow and deep acceptors which are compensated by some residual donors. For this two-layer model, the measured sheet carrier concentration and mobility are given by [48, 54]:

$$p_s = \frac{(\mu_1 p_{s,1} + \mu_2 p_{s,2})^2}{\mu_1^2 p_{s,1} + \mu_2^2 p_{s,2}}, \quad \text{and} \quad (14)$$

$$\mu = \frac{\mu_1^2 p_{s,1} + \mu_2^2 p_{s,2}}{\mu_1 p_{s,1} + \mu_2 p_{s,2}} \quad (15)$$

where μ_1 and μ_2 are the mobilities, and $p_{s,1}$ and $p_{s,2}$ are the sheet carrier concentrations of the $p\text{-Ge}_{1-y}\text{Sn}_y$ and p -type parallel conducting layers, respectively. Here the measured concentration p is given by $p = r_H / eR_H$ where the Hall factor, r_H , is defined as the ratio of the Hall mobility and the drift mobility. For this analysis, the Hall factor for both layers were set to unity.

The total volume hole concentration of the $\text{Ge}_{1-y}\text{Sn}_y$ layer including both shallow and deep acceptors must be solved for using the full charge balance equation which is given by [54]:

$$p_1 = \frac{N_{A1}}{1 + \frac{p_1}{\Phi(E_1, T)}} + \frac{N_{A2}}{1 + \frac{p_1}{\Phi(E_2, T)}} - N_D \quad (16)$$

where

$$\Phi(E, T) = \frac{g_1}{g_0} N'_V T^{3/2} \exp\left(-\frac{E}{kT}\right). \quad (17)$$

Here N_{A1} (N_{A2}) is the shallow (deep) acceptor concentration, E_1 (E_2) is the ionization energy of the shallow (deep) acceptor level, N_D is the residual donor concentration, g_0 is the degeneracy of the unoccupied acceptor state (assume $g_0 = 4$), g_1 is the degeneracy of the occupied state (assume $g_1 = 1$), and N'_V is the effective density of states of the valence band at 1 K ($N'_V \approx 9.6 \times 10^{14} \text{ cm}^{-3}$ for $m^* = 0.33m_0$). It has been assumed that the effective density of states of these $\text{Ge}_{1-y}\text{Sn}_y$ (<1% Sn) samples are essentially the same as that of Ge.

For the Hall mobility, Mattheissens rule was used which is given by

$$\frac{1}{\mu_i} = \frac{1}{\mu_I} + \frac{1}{\mu_L}$$

where μ_i is the effective mobility of the $\text{Ge}_{1-y}\text{Sn}_y$ layer, μ_I is the mobility due mainly to ionized impurity scattering which is dominant at low temperatures, and μ_L is the mobility due mainly to lattice scattering which is dominant at high temperatures. The temperature dependence of the mobility in these two regions was determined from a simultaneous parametric fit of p and μ given by Eqns. 14 and (15) to the measured carrier and mobility data. N_D was determined from the fit and was used as a free parameter only in Eqn. 16. As a result of the fit, temperature dependencies of $AT^{0.56}$ and $BT^{-2.0}$ were determined, where the proportionality factors A and B were also used as free parameters. The results of the parametric fit of Eqns. 14–17 to the measured Hall carrier concentrations and mobilities of $\text{Ge}_{0.9994}\text{Sn}_{0.0006}$ are shown in Fig. 15 as dashed red lines.

For plotting purposes, the volume carrier concentrations of both the epitaxial and the parallel conducting layers are shown which were obtained by dividing the sheet

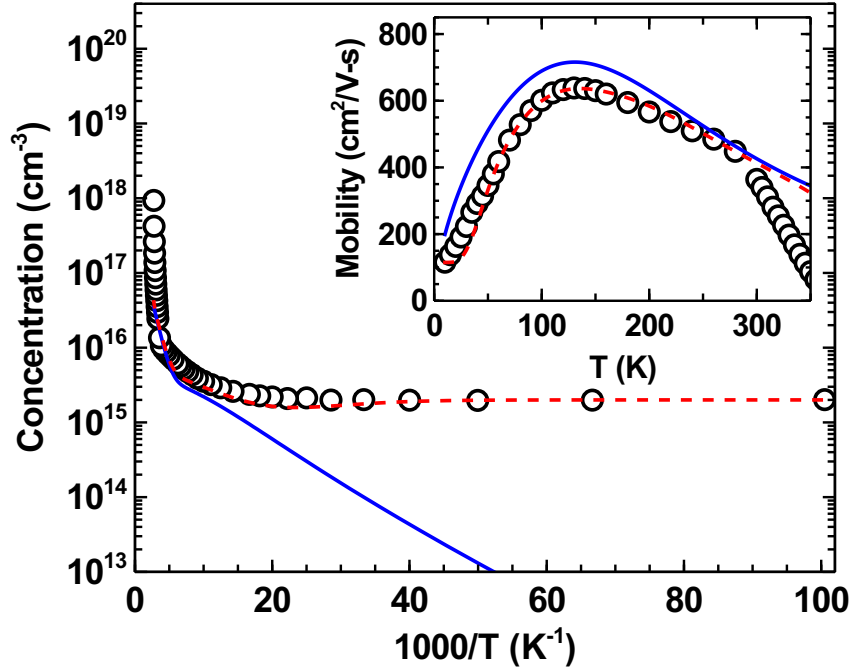


Figure 15. Two-layer model fit for the $p\text{-Ge}_{0.9994}\text{Sn}_{0.0006}/n\text{-Si}$ sample. The dashed line (red) is a curve fit to the experimental data generated using a two conducting layer model with both shallow and deep acceptors. The solid line (blue) is the calculated carrier concentration of the $p\text{-Ge}_{0.9994}\text{Sn}_{0.0006}$ epitaxial layer alone. The inset shows the measured mobility along with the fitting curve (dashed line) and the mobility of the epitaxial layer alone (solid blue line).

concentration by the $\text{Ge}_{1-y}\text{Sn}_y$ layer thickness of 800 nm. The agreement between the data and the fit is relatively good at lower temperatures. The extracted carrier concentration and mobility of the $\text{Ge}_{0.9994}\text{Sn}_{0.0006}$ layer alone are plotted as solid blue lines in Fig. 15 and the inset of Fig. 15 as a function of inverse temperature and temperature, respectively. The results indicate that the carrier concentration and mobility of the $\text{Ge}_{0.9994}\text{Sn}_{0.0006}$ layer alone are clearly affected by those of the degenerate parallel conducting layer. The true 300 K mobility of the epitaxial layer is significantly higher than the measured Hall mobility (487 as a function of. 364 $\text{cm}^2/\text{V-s}$). It is believed that the difference in mobilities is mainly due to carrier scattering near the parallel conducting layer. The temperature dependence of the

mobility in both the low and high temperature regimes was also analyzed. At low temperatures, the mobility of this $\text{Ge}_{1-y}\text{Sn}_y$ (0.06% Sn) sample varies as $T^{0.56}$. This differs from the usual $T^{3/2}$ dependence which is usually observed when ionized impurity scattering is dominant. The mobility then peaks around 130 K and starts to decrease. It then follows a $T^{-2.0}$ dependence which again differs from the usual $T^{-3/2}$ behavior when acoustic mode lattice scattering is dominant. It is worth mentioning here that for bulk p -Ge, a $T^{-2.3}$ dependence was observed by Brown and Bray [55] which they attributed to the involvement of optical phonons in the lattice scattering. The resulting fitting parameters obtained for the $\text{Ge}_{1-y}\text{Sn}_y$ ($y = 0.06\%$) layer are: $N_{A1} = 9.3 \times 10^{16} \text{ cm}^{-3}$, $E_1 = 7.5 \text{ meV}$, $N_{A2} = 9.0 \times 10^{16} \text{ cm}^{-3}$, $E_2 = 140 \text{ meV}$, and $N_D = 8.8 \times 10^{16} \text{ cm}^{-3}$. At present, the exact sources of the shallow (7.5 meV) and deeper (140 meV) acceptors are unknown. The activation energy of 7.5 meV obtained for the shallow acceptor is close to the accepted boron acceptor energy level of 10 meV at a very low doping level. However, previous SIMS measurements showed no detectable boron impurities (within the detection limit of about mid 10^{15} cm^{-3}) in the sample. Thus, further investigation is required to find the exact sources of the acceptors.

Etch Studies

To further investigate the source of the degenerate parallel conducting layer and to determine the properties of the $\text{Ge}_{1-y}\text{Sn}_y$ layer alone, etch studies were performed on selected samples with temperature dependent Hall-effect measurements made from 10 – 300 K after each etch. In addition to the interfacial conducting layer, a significant contribution from surface states were observed. These surface states were quantified by performing room temperature Hall-effect measurements in both ambient (air) and in vacuum with the surface state density given by the difference

in the carrier density. A systematic decrease in the number of (p -type) carriers was observed in vacuum when compared to that in the ambient (air). This reduction is most likely due an (n -type) electron accumulation layer which is formed under vacuum at the p -Ge_{1-y}Sn_y surface. This surface conducting channel is destroyed when exposed to air probably via adsorption of atoms or molecules at the Ge_{1-y}Sn_y surface which occupy the sites. Similar p -type surface states were reported by Alberghini, et al [45] in n -type germanium. Surface states in ZnO were investigated by Schmidt et al [44] using temperature dependent Hall-effect measurements in both air and vacuum. Soderstrom, et al [43] also reported the observation of n -type surface states in p -type InSb.

Simplified energy band diagrams are shown in Figure 16 to illustrate the effect of the n -type surface states in combination with the p -type degenerate conducting layer and the shallow and deep acceptors and intrinsic carriers of the Ge_{1-y}Sn_y layer itself. Fig. 16a shows a diagram for low temperatures, i.e. where none of the shallow or deep acceptors are ionized. In this case, the only contributions to the conduction are the p -type degenerate layer with a carrier density of p_{degen} and the n -type surface state with a density of n_{surf} . The total measured carrier concentration is then approximately given by $p_{\text{meas}} = p_{\text{degen}} - n_{\text{surf}}$. Since the measured carriers at LT were p -type, we know that $p_{\text{degen}} > n_{\text{surf}}$. The actual degenerate carrier density is then given by, $p_{\text{degen}} = p_{\text{meas}} + n_{\text{surf}}$. Fig. 16b shows a diagram for intermediate temperatures where some of the shallow acceptors have been ionized and the measured carriers have increased. Finally, Fig. 16c shows a diagram at room temperature.

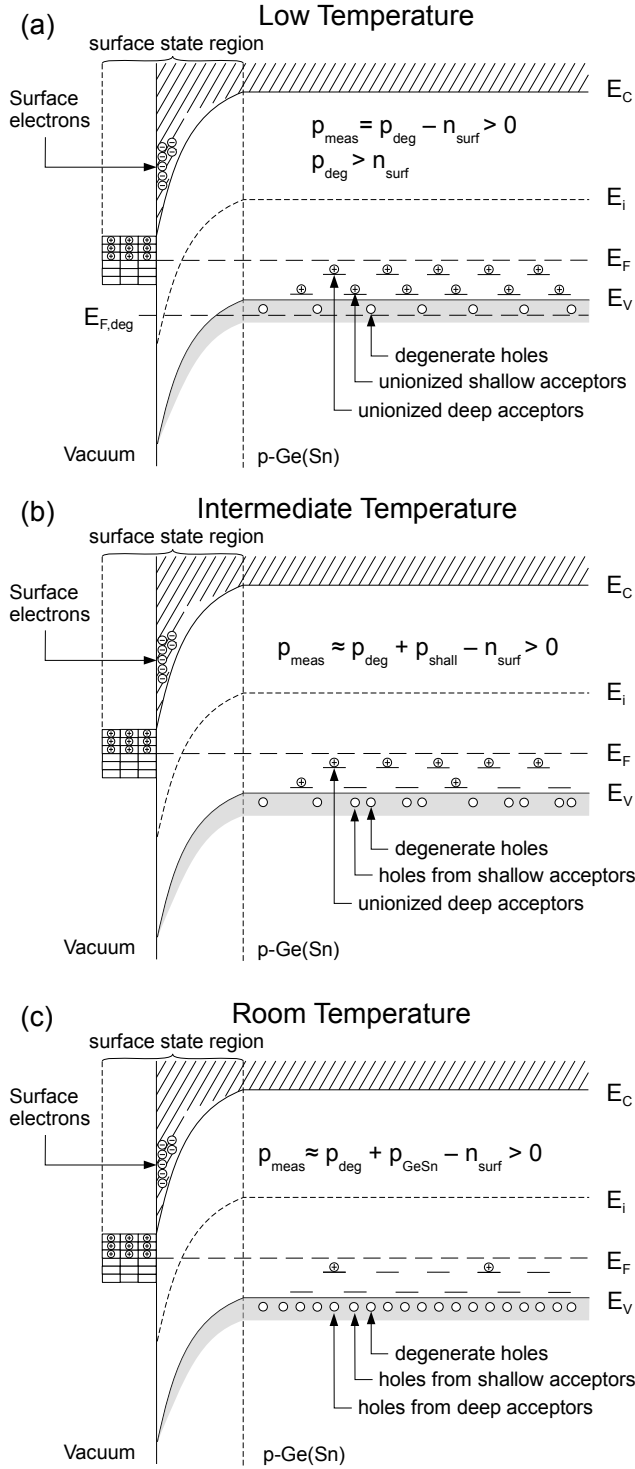


Figure 16. Classical energy-band diagrams at the p -Ge(Sn) surface. The surface state region shows an n -type inversion layer with accumulated surface electrons. Diagrams are shown for (a) Low T (b) Intermediate T and (c) RT for these p -Ge(Sn)/ n -Si samples.

The temperature dependent sheet carrier concentration of this $\text{Ge}_{1-y}\text{Sn}_y$ (0.06% Sn) sample is plotted as a function of inverse temperature for all etches in Figure 17. Carrier profiles for selected temperatures are shown as a function of etch depth in Table 4. As seen in the figure, the hole carrier density was observed to systematically decrease for each subsequent etch. However, some degenerate conduction at low temperatures persisted until almost all of the epilayer was removed, confirming that its origin was in the interfacial region. As the etching progressed some of the Hall data at low temperatures became unmeasurable and thus are not shown in the figure. As mentioned previously, the measured carrier concentration at low temperatures is given by the difference between the actual degenerate p -type carrier concentration and the n -type surface state carrier density. It could be that when sufficient layers were etched, this difference decreased to the point where it could not be reliably measured. In other words the degenerate interfacial layer and the surface layer could compensate each other and cause the net measured carriers to be negligible at low T.

Table 4. Measured sheet carrier concentration in cm^{-2} as a function of etch depth at selected temperatures for the $p\text{-GeSn}/n\text{-Si}$ (0.06% Sn) sample.

Etch Depth (nm)	Temperature				
	50 K	75 K	100 K	200 K	250 K
0	1.72×10^{11}	2.26×10^{11}	3.26×10^{11}	7.96×10^{11}	1.19×10^{12}
180	1.48×10^{11}	2.07×10^{11}	2.97×10^{11}	7.26×10^{11}	9.60×10^{11}
330	1.12×10^{11}	1.70×10^{11}	2.59×10^{11}	7.00×10^{11}	9.44×10^{11}
430	7.11×10^{10}	1.60×10^{11}	2.68×10^{11}	6.84×10^{11}	9.17×10^{11}
530	1.00×10^{11}	1.43×10^{11}	2.38×10^{11}	6.01×10^{11}	8.23×10^{11}
630	5.26×10^{10}	2.27×10^{11}	2.20×10^{11}	4.96×10^{11}	7.12×10^{11}
730	7.99×10^{11}	1.76×10^{11}	1.93×10^{11}	4.88×10^{11}	6.56×10^{11}
830	4.17×10^{10}	4.94×10^{10}	1.19×10^{11}	4.09×10^{11}	5.37×10^{11}
920	1.09×10^8	1.18×10^9	2.44×10^{10}	5.62×10^{11}	6.27×10^{11}

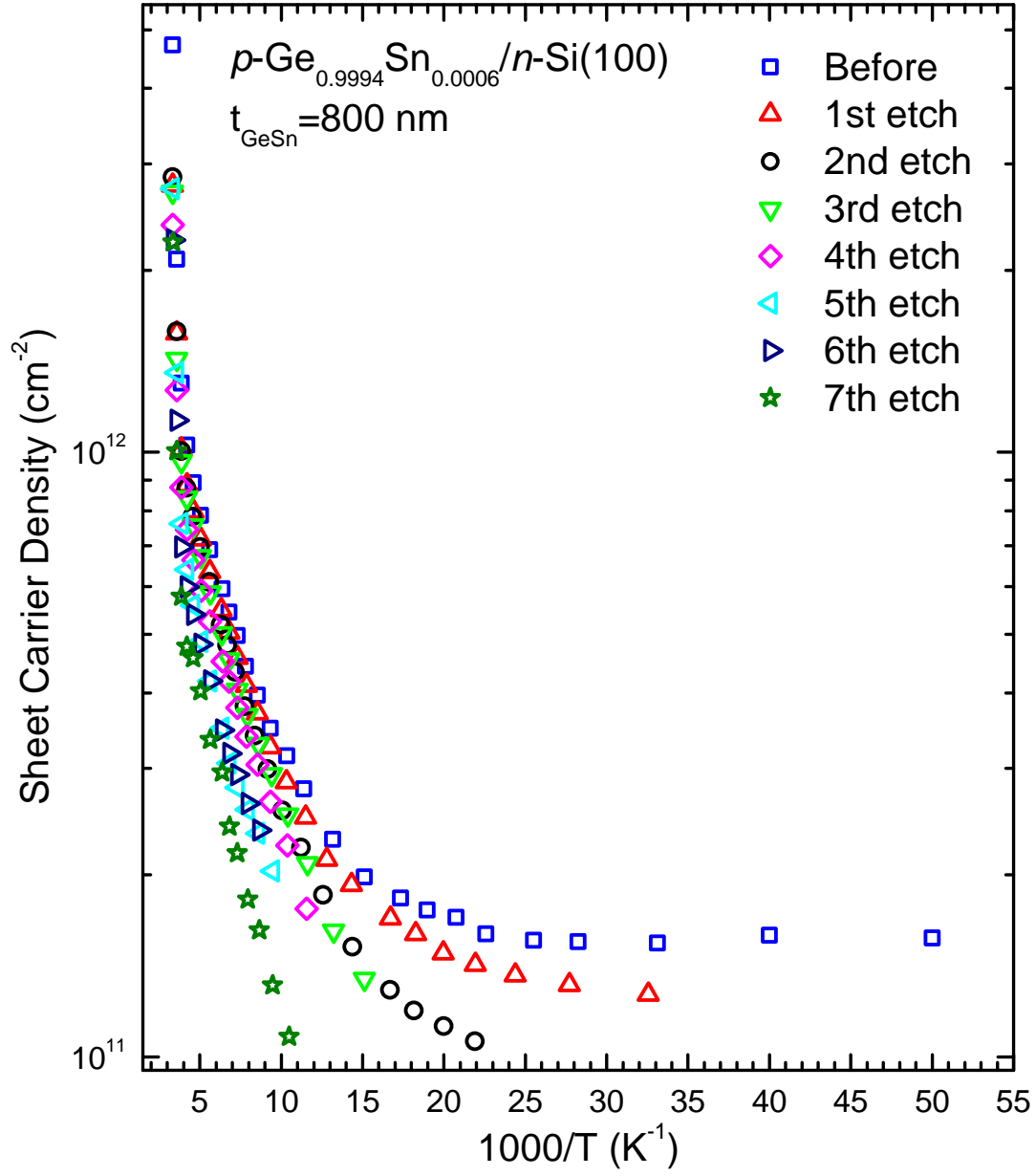


Figure 17. Sheet carrier concentration plotted as a function of inverse temperature for the $p\text{-Ge}_{0.9994}\text{Sn}_{0.0006}/n\text{-Si}$ sample for all etches.

The mobilities of this $\text{Ge}_{1-y}\text{Sn}_y$ (0.06 % Sn) sample are plotted as a function of temperature in Figure 18 for all etches. All of the data shows a sudden decrease in the mobility from 280 K to 300 K which is due to the kink described earlier. After the first etch, the low-temperature(T) (< 40 K) mobility decreased slightly, but the mobility and higher temperatures (> 100 K) increased significantly. This could be due to the fact that the first etch would have removed any native oxide layer from the $\text{Ge}_{0.9994}\text{Sn}_{0.0006}$ film, resulting in a relatively clean surface after the etch. This may have resulted in less carrier scattering at the surface and therefore a higher mobility. After the second etch, the low-T mobility decreased significantly, while the high-T mobility only decreased slightly, still remaining higher than before etching. After the 3rd etch, the low-T mobility decreased further and the peak of the mobility curve shifted to a higher temperature of about 135 K. After the 4th etch (a total etched depth of 530 nm), the mobility changed drastically with a large increase for all temperatures. The peak of the mobility also shifted to a higher temperature of about 160 K. After the 5th etch, the high-T mobility decreased dramatically and was even lower than the values before etching. After the 6th etch, the high-T mobility increased again, but only to about the values of the first 3 etches. The lowest temperature at which the mobility was measureable increased from around 80 K for the 4th etch to about 120 K for the 6th etch. After the 7th etch, the shape of the mobility curve changed completely with the peak now occurring near 260 K. Overall, the mobility decreased significantly, however for T's greater than about 240 K, it remained about the same with the 300 K mobility even showing a slight increase over the previous etch. This change in shape might be due to the degenerate interfacial layer which could cause a flattening of the mobility curve. The significant decrease in mobility is probably due to the very small thickness of the remaining $\text{Ge}_{1-y}\text{Sn}_y$ layer.

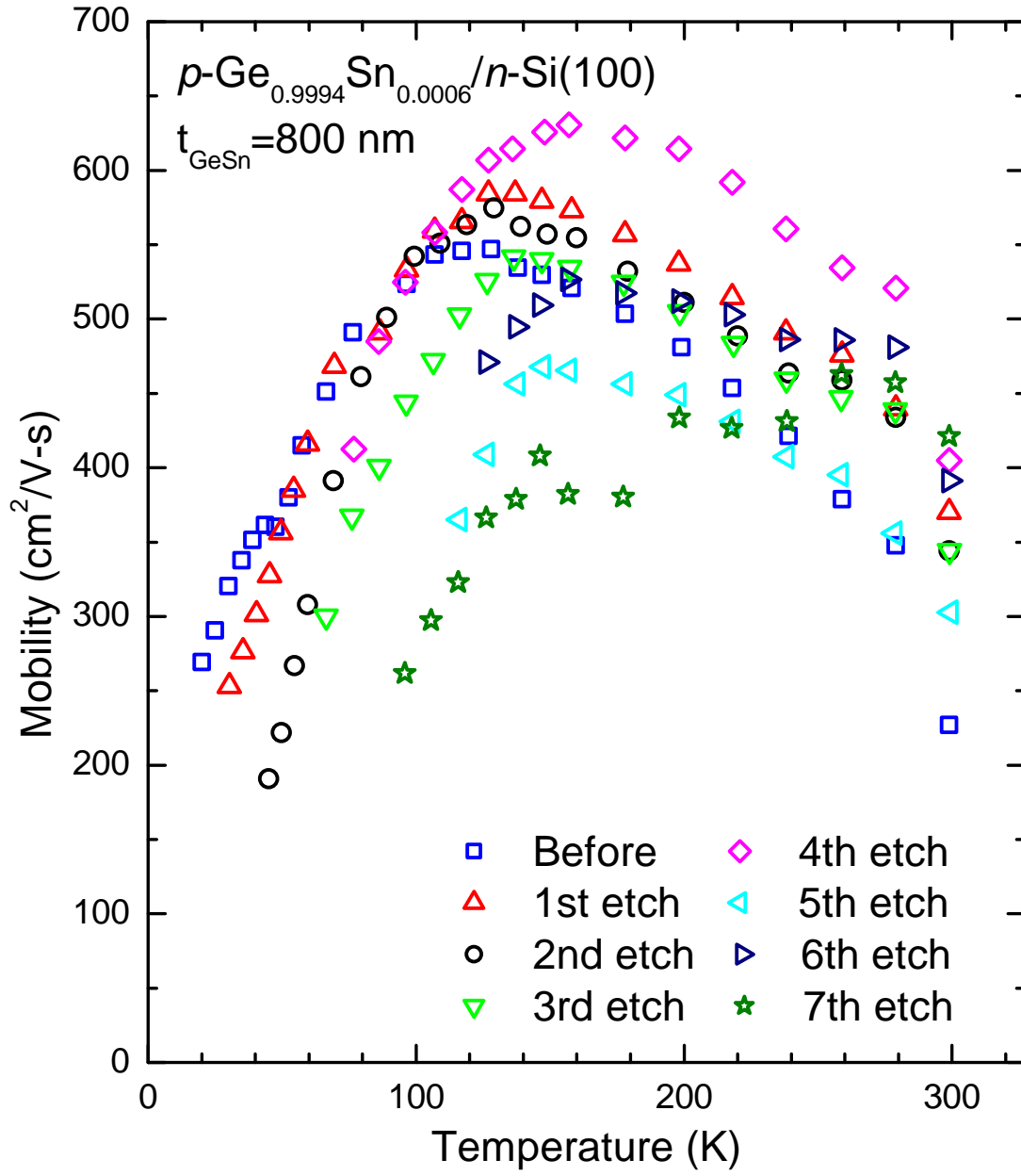


Figure 18. Carrier mobility plotted as a function of temperature for the $p\text{-Ge}_{0.9994}\text{Sn}_{0.0006}/n\text{-Si}$ sample for all etches.

The log of the conductivity is plotted as a function of inverse temperature in Figure 19 for all etches. In the low temperature region, the conductivity initially decreases with etch depth down to about 300 nm, then remains fairly constant from 300 nm to about 530 nm, after which it continues to decrease. The high temperature conductivity also decreases slightly with etch depth down to about 530 nm and then decreases much more rapidly for the last 2 etches.

The RT carrier concentration is plotted as a function of etch depth in Figure 20 for both air (red squares) and vacuum (black circles) and the data is shown in Table 5. The decrease in carriers as etch depth increases can clearly be seen in the figure. This is consistent with the removal of a *p*-type layer. As mentioned previously, the carrier concentration measured in air is consistently higher than that measured in vacuum. This is believed to be caused by *n*-type surface states that form under vacuum. Some simple linear fits were performed to quantify the decrease in carriers as well as the contribution from surface states. Both data sets were fit simultaneously with the constraint that the slopes of the two lines matched. The slope determined from the fit was $-1.15 \times 10^9 \text{ cm}^{-2}/\text{nm}$, which corresponds to a (*p*-type) volume carrier density of $1.15 \times 10^{16} \text{ cm}^{-3}$ in the $\text{Ge}_{1-y}\text{Sn}_y$ layer. The offset between the fitted lines of air and vacuum data gives the surface state (*n*-type) carrier density which was $9.0 \times 10^{11} \text{ cm}^{-2}$ for this sample. As seen in Fig. 17, the carrier concentration measured at LT in vacuum, p_{meas} , was about $1.6 \times 10^{11} \text{ cm}^{-2}$. However, the actual low-temperature degenerate carrier concentration, p_{degen} , could be $1.06 \times 10^{12} \text{ cm}^{-2}$ ($p_{\text{degen}} = p_{\text{meas}} + n_{\text{surf}} = 1.6 \times 10^{11} + 9.0 \times 10^{11}$). This is a significant difference and is due to the fact that the surface state density is much larger than the measured carriers at low T.

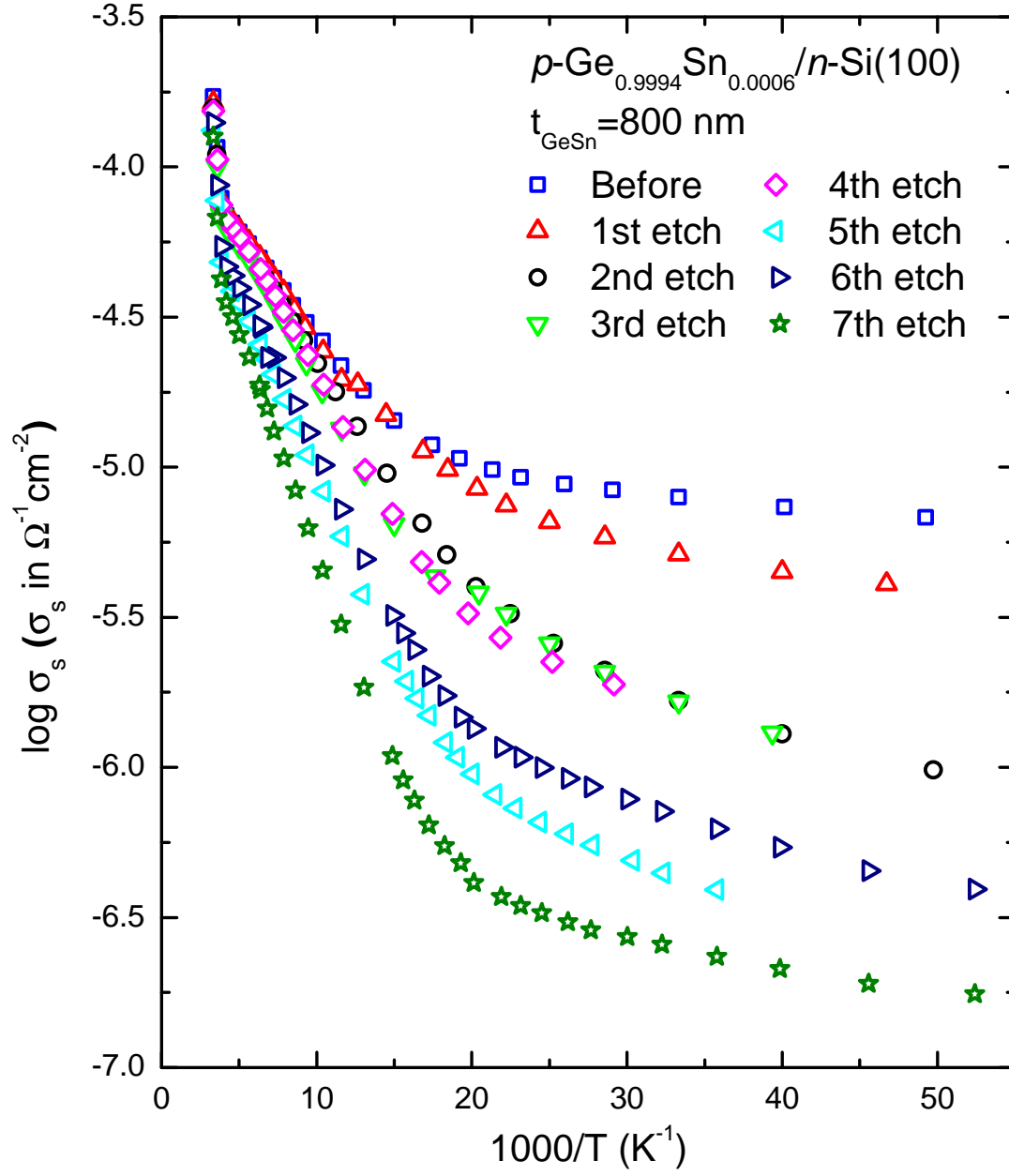


Figure 19. Log conductivity plotted as a function of inverse temperature for the $p\text{-Ge}_{0.9994}\text{Sn}_{0.0006}/n\text{-Si}$ sample for all etches.

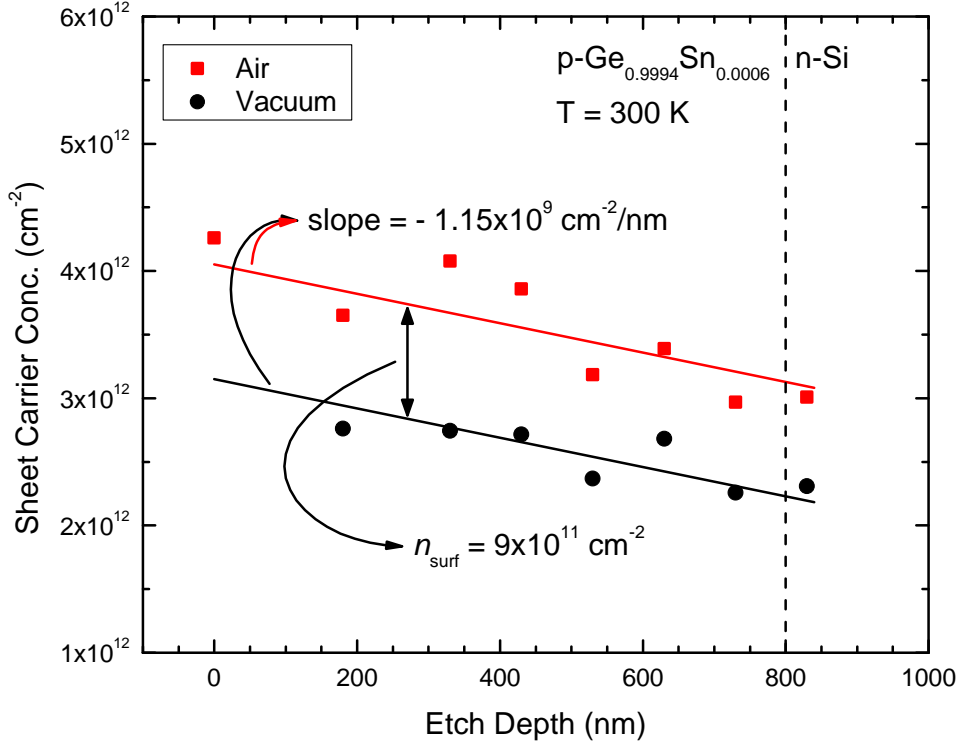


Figure 20. Room temperature sheet carrier concentration plotted as a function of etch depth for the $p\text{-Ge}_{0.9994}\text{Sn}_{0.0006}/n\text{-Si}$ sample. An estimated volume carrier density of $1.15 \times 10^{16} \text{ cm}^{-3}$ was obtained. The average surface state density was $9.0 \times 10^{11} \text{ cm}^{-2}$.

Table 5. Sheet carrier concentration measured at RT in both air and vacuum as a function of etch depth for the $p\text{-GeSn}/n\text{-Si}$ (0.06% Sn) sample.

Removed Thickness (nm)	Etch Depth (nm)	Carrier Conc. in Air, p_{air} (cm^{-2})	Carrier Conc. in Vacuum, p_{vac} (cm^{-2})	Surface State Density, n_{surf} (cm^{-2})
180	180	3.65×10^{12}	2.76×10^{12}	8.91×10^{11}
150	330	4.08×10^{12}	2.74×10^{12}	1.33×10^{12}
100	430	3.86×10^{12}	2.72×10^{12}	1.14×10^{12}
100	530	3.19×10^{12}	2.37×10^{12}	8.16×10^{11}
100	630	3.39×10^{12}	2.68×10^{12}	7.10×10^{11}
100	730	2.97×10^{12}	2.26×10^{12}	7.13×10^{11}
100	830	3.01×10^{12}	2.31×10^{12}	7.00×10^{11}

In order to more accurately determine the carrier density in the $\text{Ge}_{1-y}\text{Sn}_y$ layer, a differential Hall calculation was applied where the carriers in the i^{th} layer of removed thickness d_i are given by:

$$N_i = \frac{\Delta \left(\frac{1}{\rho_s} \right)_i}{e\mu_i d_i}, \quad (18)$$

$$\text{where } \mu_i = \frac{\Delta \left(\frac{R_{Hs}}{\rho_s^2} \right)_i}{\Delta \left(\frac{1}{\rho_s} \right)_i} \quad (19)$$

$$\text{and } \Delta \left(\frac{1}{\rho_s} \right)_i = \frac{1}{(\rho_s)_i} - \frac{1}{(\rho_s)_{i+1}}, \quad (20)$$

$$\text{and where } \Delta \left(\frac{R_{Hs}}{\rho_s^2} \right)_i = \frac{(R_{Hs})_i}{(\rho_s)_i^2} - \frac{(R_{Hs})_{i+1}}{(\rho_s)_{i+1}^2} \quad (21)$$

Here $(R_{Hs})_i$ and $(\rho_s)_i$ are the sheet Hall coefficient and the sheet resistivity measured after the removal of the i^{th} layer and e is the electron charge. We can rewrite this in a more useful form by converting the Hall coefficient to carrier density using the equation $(R_{Hs})_i = 1/e(n_s)_i$. Doing so, we obtain

$$\Delta \left(\frac{R_{Hs}}{\rho_s^2} \right)_i = \frac{1}{e(n_s)_i(\rho_s)_i^2} - \frac{1}{e(n_s)_{i+1}(\rho_s)_{i+1}^2} = \frac{1}{e} \Delta \left(\frac{1}{n_s \rho_s^2} \right)_i \quad (22)$$

The results of the differential Hall equations at RT are plotted as a function of etch depth in Figure 21. There is a large variation in the calculated carrier concentration. However, there is a clear increase in carriers near the film-substrate interface which is consistent with the degenerate interfacial layer discussed earlier. The average value for the first 5 etches is about $3.21 \times 10^{15} \text{ cm}^{-3}$ which is much lower than the value of $1.4 \times 10^{16} \text{ cm}^{-3}$ derived from the linear fits. It is also

significantly lower than the value of $2.97 \times 10^{16} \text{ cm}^{-3}$ given by Table 3. Looking back to Fig. 21, we can see that the average value for the final two etches near the interface is about $6.53 \times 10^{16} \text{ cm}^{-3}$, which is more than one order of magnitude larger than the calculated carrier concentration in the film. Again this large increase could be due to the degenerate conducting layer near the interface.

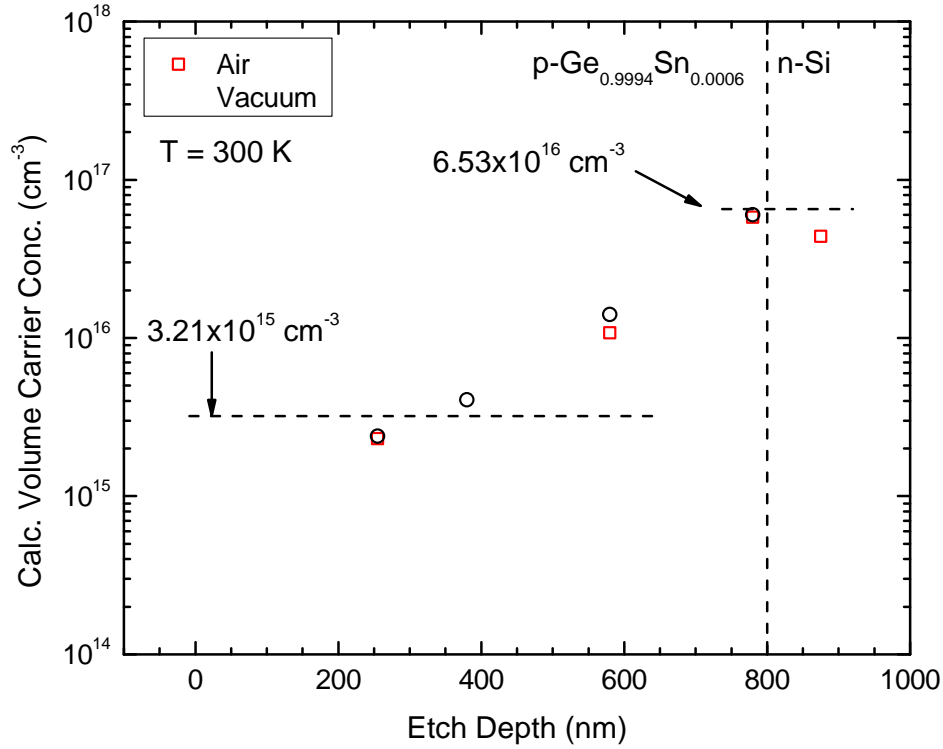


Figure 21. Volume carrier concentration of each removed layer plotted as a function of etch depth for the $p\text{-Ge}_{0.9994}\text{Sn}_{0.0006}/n\text{-Si}$ sample calculated using the differential Hall model in Eqns. (18)-(22).

Carrier profiles for selected temperatures are plotted as a function of etch depth in Figure 22. Since the actual measured temperatures varied for each set of T-dependent data, the measured carrier concentration was linearly interpolated to give values at a common set of temperatures. This then allowed for a direct comparison of the carrier depth profiles at different temperatures. As seen in Fig. 22, the carriers show a clear decrease as a function of etch depth for all of the selected temperatures. As mentioned previously, for temperatures below 75 K and etch depths beyond about 500 nm, the carriers were not measureable. This is also clearly seen in Fig. 17 where the low-T carriers for the later etches are not shown. Again, this could be due to some compensation between the *p*-type degenerate interfacial layer and the *n*-type surface states along with the lack of ionized acceptor contributions at lower temperatures. To determine the volume carrier density in the removed layers, the differential Hall equations were applied to the data for each selected temperature. The results of those calculations are shown in Figure 23. As was the case with the RT carriers measured in air and vacuum, there is a significant amount of fluctuation in the data. Still, the calculated carrier density remained fairly constant throughout the film, increasing dramatically near the interface. This agrees with the air and vacuum data at 300 K shown earlier and confirms the presence of a degenerate conducting layer near the interface. The average values in the film and near the interface were $2.23 \times 10^{15} \text{ cm}^{-3}$ and $1.46 \times 10^{16} \text{ cm}^{-3}$, respectively, which are both lower than the values obtained from the RT data. However the increase in carriers from the film to near the interface is still almost one order of magnitude which agrees well with the RT data.

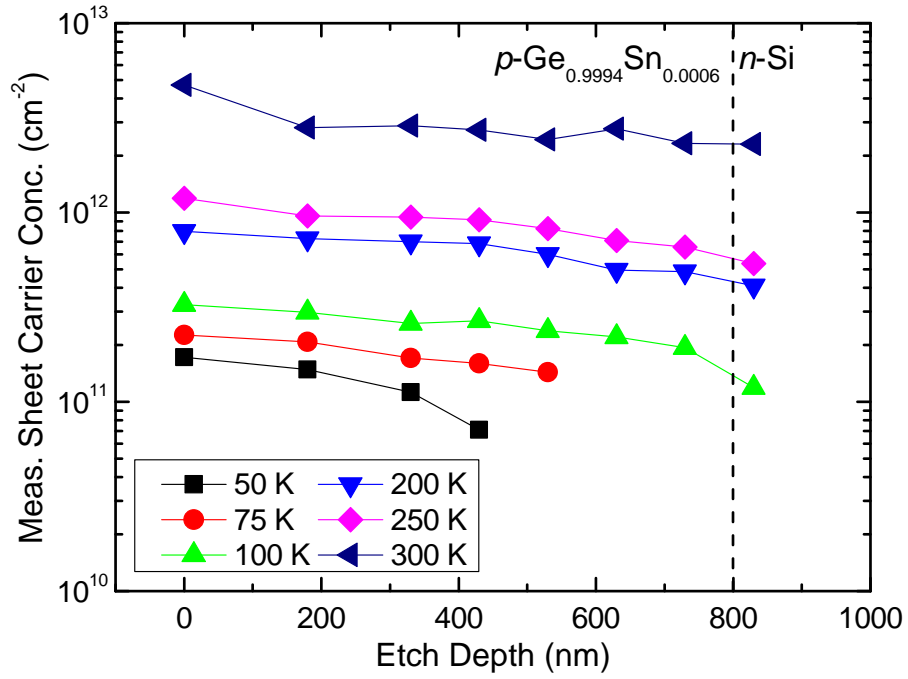


Figure 22. Measured sheet carrier profiles plotted as a function of etch depth at different temperatures for the $\text{Ge}_{0.9994}\text{Sn}_{0.0006}$ sample.

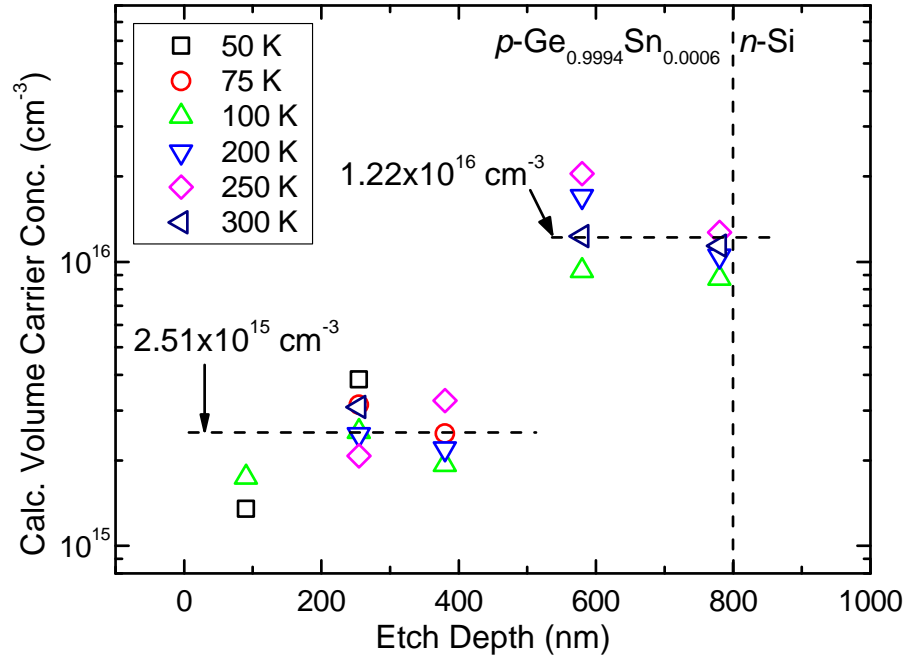


Figure 23. Calculated volume carrier profiles plotted as a function of etch depth at different temperatures for the $\text{Ge}_{0.9994}\text{Sn}_{0.0006}$ sample.

Analysis of the $p\text{-Ge}_{1-y}\text{Sn}_y/n\text{-Si}$ (0.1% Sn) Sample

Etch Studies

The temperature dependent sheet carrier concentration of this $\text{Ge}_{0.999}\text{Sn}_{0.001}$ sample is plotted as a function of inverse temperature for all etches in Figure 24. Carrier profiles for selected temperatures are shown as a function of etch depth in Table 6. This sample shows a slightly different behavior from the $\text{Ge}_{0.9994}\text{Sn}_{0.0006}$ sample. The low temperature carrier concentration did systematically decrease as a function of etch depth which was similar to the previous sample. For temperatures greater than about 90 K, however, the carriers only changed slightly, if at all. At room temperature the carrier concentration decreased some but the change was not as large as with the $\text{Ge}_{0.9994}\text{Sn}_{0.0006}$ sample. Measured sheet carrier concentration profiles for selected temperatures are shown as a function of etch depth in Table 6

Table 6. Measured sheet carrier concentration in cm^{-2} as a function of etch depth at selected temperatures for the $p\text{-GeSn}/n\text{-Si}$ (0.1% Sn) sample.

Etch Depth (nm)	Temperature				
	50 K	75 K	100 K	200 K	250 K
0	1.089×10^{11}	1.478×10^{11}	2.127×10^{11}	5.448×10^{11}	7.846×10^{11}
86	1.033×10^{11}	1.495×10^{11}	2.173×10^{11}	5.412×10^{11}	7.264×10^{11}
193	9.774×10^{10}	1.492×10^{11}	1.950×10^{11}	5.405×10^{11}	7.261×10^{11}
353	9.436×10^{10}	1.460×10^{11}	2.140×10^{11}	5.315×10^{11}	7.096×10^{11}
516	1.083×10^{11}	1.428×10^{11}	2.276×10^{11}	5.272×10^{11}	7.018×10^{11}
665	1.004×10^{11}	1.526×10^{11}	2.097×10^{11}	5.214×10^{11}	6.869×10^{11}
815	9.697×10^{10}	1.488×10^{11}	2.177×10^{11}	5.188×10^{11}	6.846×10^{11}
968	9.486×10^{10}	1.4167×10^{11}	2.103×10^{11}	5.101×10^{11}	6.668×10^{11}
1067	1.015×10^{11}	1.315×10^{11}	2.012×10^{11}	5.117×10^{11}	6.827×10^{11}
1176	7.768×10^{10}	1.382×10^{11}	1.865×10^{11}	5.112×10^{11}	6.875×10^{11}

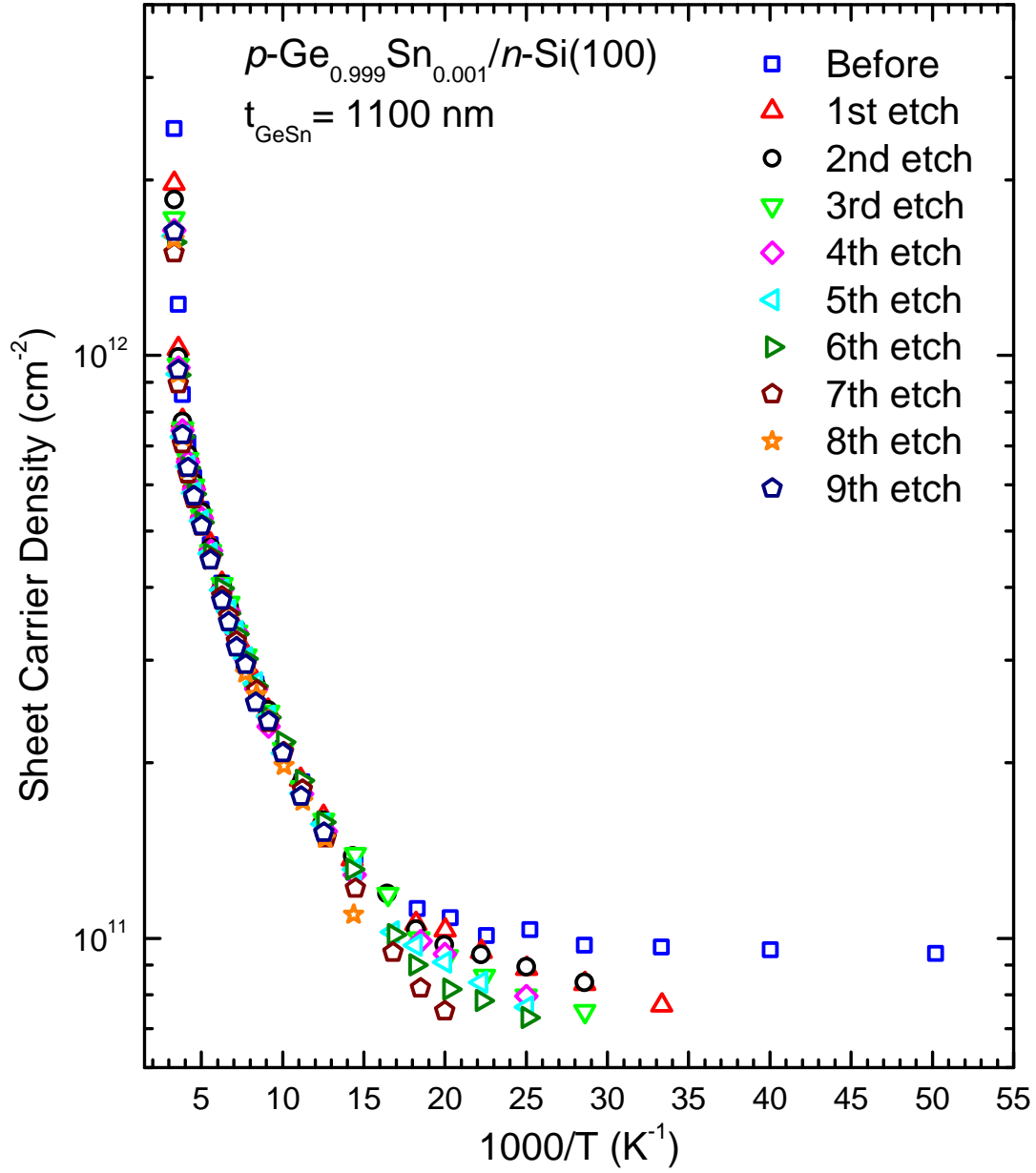


Figure 24. Sheet carrier concentration plotted as a function of inverse temperature for the $p\text{-Ge}_{0.999}\text{Sn}_{0.001}/n\text{-Si}$ sample for all etches.

The mobilities of this $\text{Ge}_{0.999}\text{Sn}_{0.001}$ sample are plotted as a function of temperature in Figure 25 for all etches. The mobilities at low temperatures increased very slightly with etch depth. The mobilities at higher temperatures (near RT) increased more significantly. The low-T mobility decreased slightly after the 7th etch (967 nm depth), but the high-T mobility remained about the same. After the 8th etch (1066 nm depth) the mobility decreased significantly. The low-T values were lower than before etching, but the high-T values remained slightly higher than before etching. Finally after the 9th etch (1175 nm depth), the mobilities decreased dramatically with most of the values less than those before etching. The peak of the mobility curve also shifted up to about 200 K. This shows a similar behavior to the previous sample for the last etch with a large decrease in the mobility values as well as a flattening of the mobility curve.

The log of the conductivity for this $\text{Ge}_{0.999}\text{Sn}_{0.001}$ sample is plotted as a function of inverse temperature in Figure 26 for all etches. The low-T conductivity increases slightly with etch depth for the first 6th etches (up to 815 nm depth), then decreases slightly after the 7th etch, and finally decreases more rapidly after the 8th and 9th etches. The high-T conductivity shows a similar trend, but the change is less pronounced.

The RT carrier concentration for this $\text{Ge}_{0.999}\text{Sn}_{0.001}$ sample is plotted as a function of etch depth in Figure 27 for both air and vacuum with the corresponding data shown in Table 7. Even though the temperature-dependent carrier concentration did not show the much decrease at all with etch depth, a clear decrease is observed in the RT result as seen in the figure. Again, this is reassuring since it is consistent with the removal of a *p*-type layer. As was the case with the $\text{Ge}_{0.9994}\text{Sn}_{0.0006}$ sample, the carrier concentration measured in air is consistently higher than that measured in vacuum. Again, this indicates the formation of *n*-type surface states.

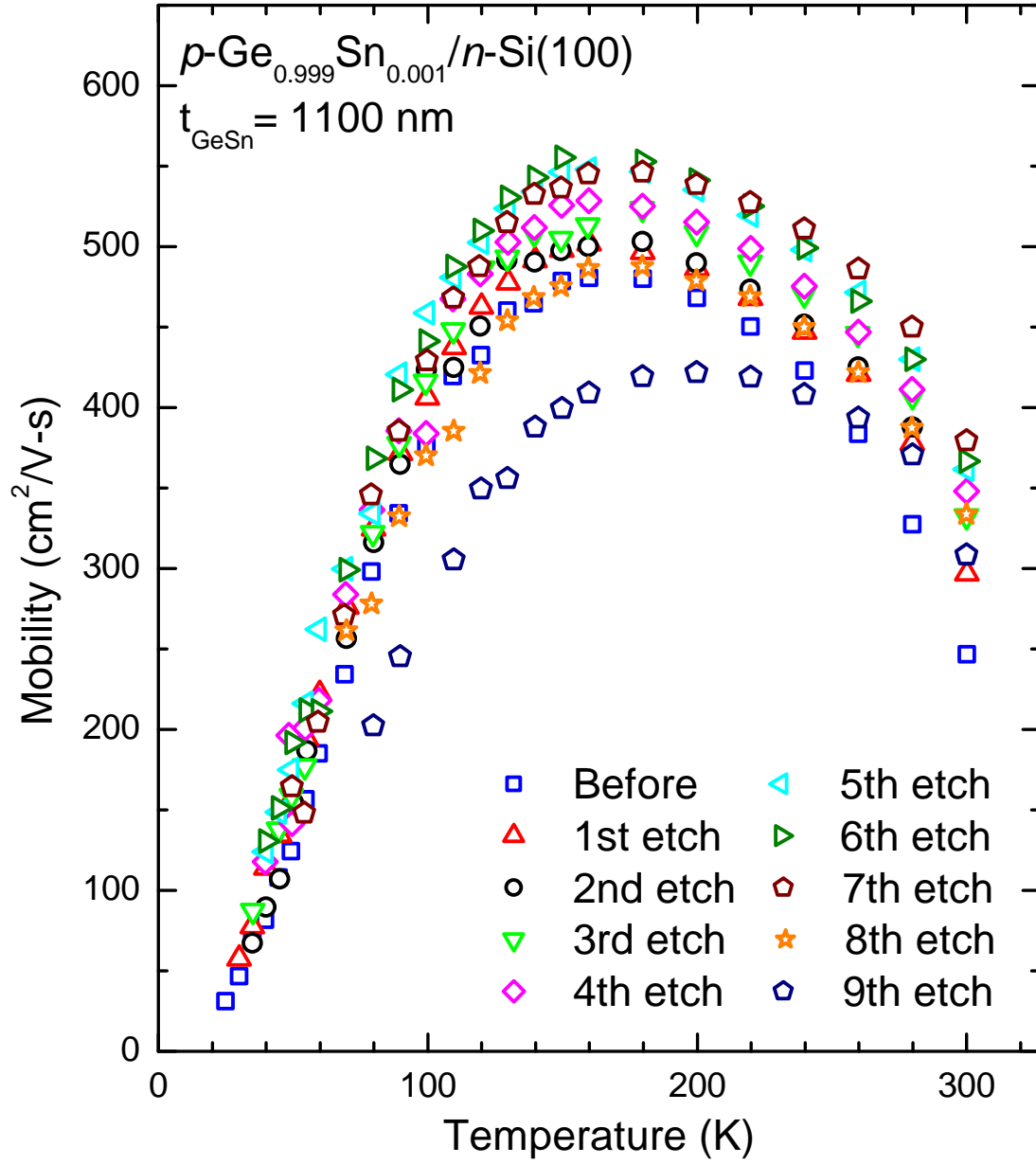


Figure 25. Carrier mobility plotted as a function of temperature for the $p\text{-Ge}_{0.999}\text{Sn}_{0.001}/n\text{-Si}$ sample for all etches.

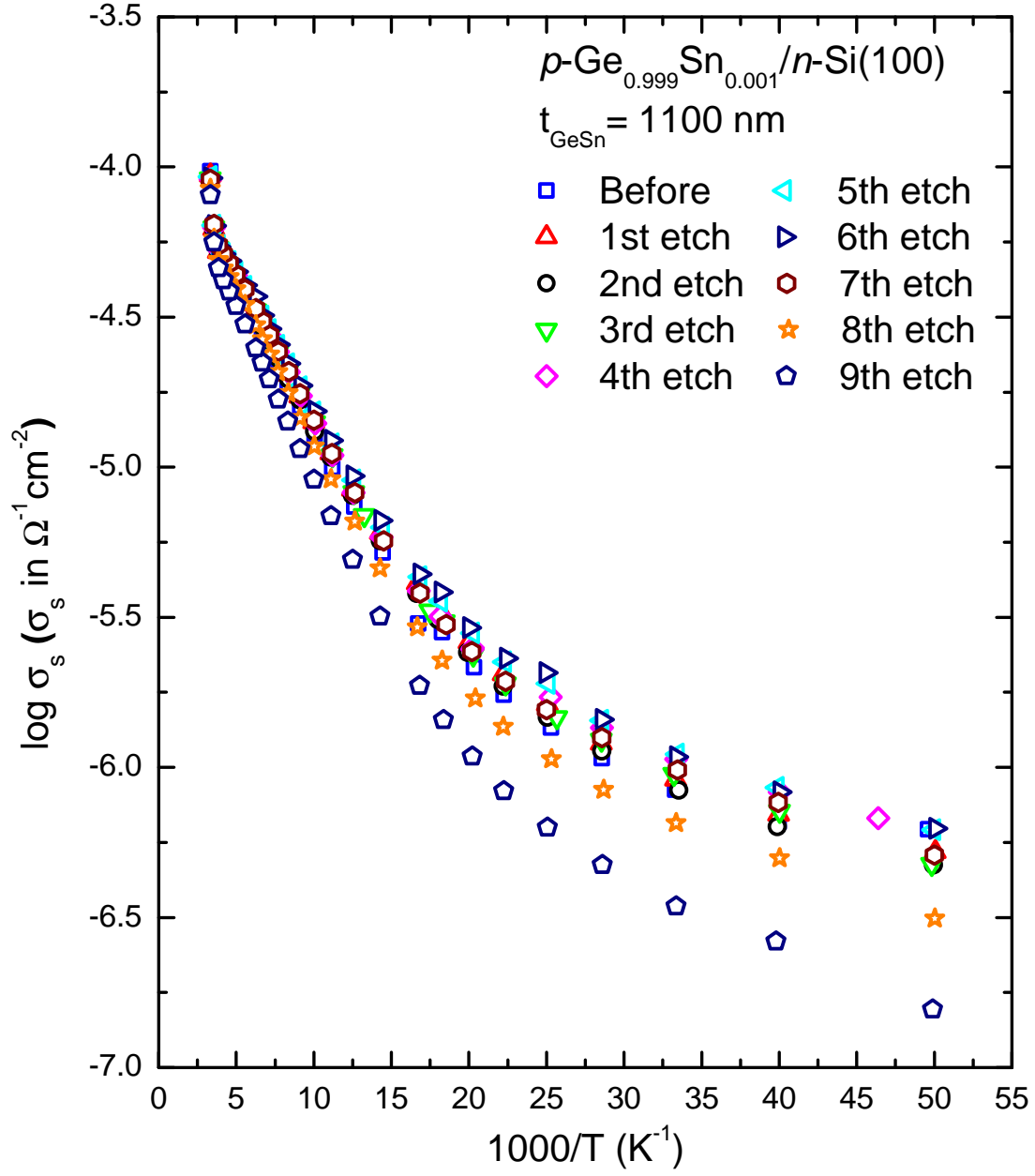


Figure 26. Log conductivity plotted as a function of inverse temperature for the $p\text{-Ge}_{0.999}\text{Sn}_{0.001}/n\text{-Si}$ sample for all etches.

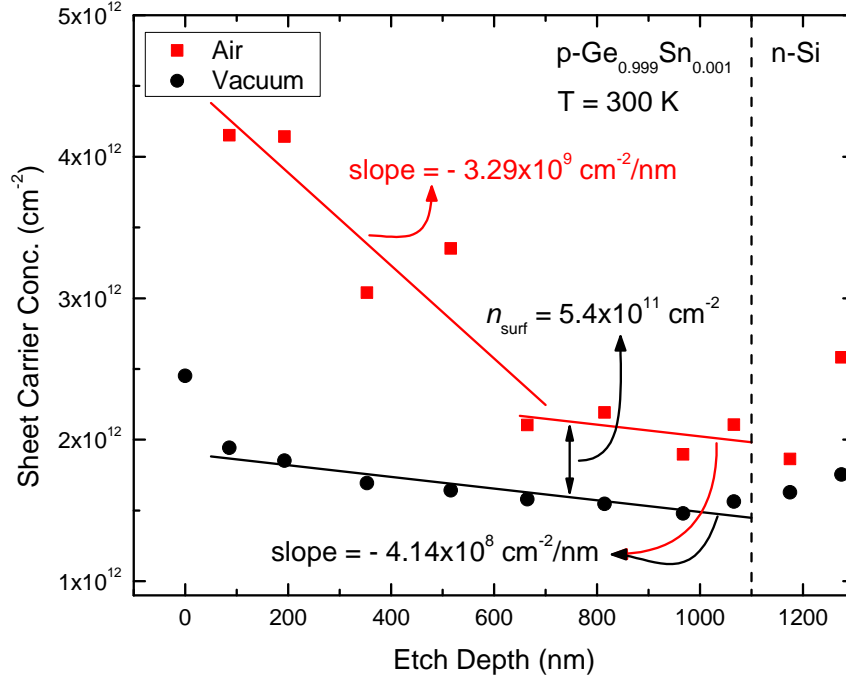


Figure 27. Room temperature sheet carrier concentration plotted as a function of etch depth for the $p\text{-Ge}_{0.999}\text{Sn}_{0.001}/n\text{-Si}$ sample including linear fits with different slopes.

Table 7. Sheet carrier concentration measured at RT in both air and vacuum as a function of etch depth for the $p\text{-GeSn}/n\text{-Si}$ (0.1% Sn) sample.

Etch Depth, d (nm)	Carrier Conc. in Air, p_{air} (cm ⁻²)	Carrier Conc. in Vacuum, p_{vac} (cm ⁻²)	Surface State Density, n_{surf} (cm ⁻²)
0	4.530×10^{12}	2.451×10^{12}	2.08×10^{12}
86	4.150×10^{12}	1.942×10^{12}	2.21×10^{12}
193	4.141×10^{12}	1.852×10^{12}	2.29×10^{12}
353	3.039×10^{12}	1.693×10^{12}	1.35×10^{12}
516	3.350×10^{12}	1.642×10^{12}	1.71×10^{12}
665	2.103×10^{12}	1.578×10^{12}	5.26×10^{11}
815	2.192×10^{12}	1.545×10^{12}	6.47×10^{11}
967	1.896×10^{12}	1.479×10^{12}	4.17×10^{11}
1066	2.106×10^{12}	1.563×10^{12}	5.43×10^{11}
1175	1.863×10^{12}	1.628×10^{12}	2.35×10^{11}
1275	2.583×10^{12}	1.754×10^{12}	8.28×10^{11}

In contrast to the previous sample, the surface states do not seem to be constant for all etches in this case. In fact, the RT carrier concentration measured in air changes much more rapidly with etch depth than that measured in vacuum. Linear fits were performed to calculate the surface state density and to determine the carriers in each layer. However, this time the air and vacuum data were fit with different slopes. The results of the fit are also shown in Figure 27. The fit to the vacuum data gave a slope of $-4.14 \times 10^8 \text{ cm}^{-2}/\text{nm}$, and an offset (value before etching) of $1.90 \times 10^{12} \text{ cm}^{-2}$. To obtain the best fit, the first 6 values measured in air (Etches 0-5) were fit separately and showed a large decrease with a slope of $-3.29 \times 10^9 \text{ cm}^{-2}/\text{nm}$ and an offset (value before etching) of $4.55 \times 10^{12} \text{ cm}^{-2}$. The next 4 values (Etches 5-8) were well fit separately using the slope of $-4.14 \times 10^8 \text{ cm}^{-2}/\text{nm}$ obtained from the vacuum data. An offset of $2.44 \times 10^{12} \text{ cm}^{-2}$ was obtained.

An examination of the surface state density for this sample is more difficult. Because the slopes between the air and vacuum cases are different, the surface state density is no longer constant. It is still given by the difference between the air and vacuum data, but it will change as a function of etch depth. Based on these fits, the surface state density could vary from $2.4 \times 10^{12} \text{ cm}^{-2}$ for an etch depth of about 80 nm to $5.4 \times 10^{11} \text{ cm}^{-2}$ for etch depths from about 650 nm to 1100 nm. The latter value is smaller than the surface state density of $9.0 \times 10^{11} \text{ cm}^{-2}$ for the $\text{Ge}_{0.9994}\text{Sn}_{0.0006}$ sample. From Fig. 24, we can see that the measured (vacuum) carrier concentration at LT, p_{meas} , was about $9.5 \times 10^{10} \text{ cm}^{-2}$ for this $\text{Ge}_{0.999}\text{Sn}_{0.001}$ sample. Using the surface state value of 2.4×10^{12} obtained for small etch depths, we get an actual low temperature carrier concentration of $2.5 \times 10^{12} \text{ cm}^{-2}$ ($=p_{\text{meas}}+n_{\text{surf}}= 9.5 \times 10^{10} + 2.4 \times 10^{12}$). Using the surface state value of 5.4×10^{11} obtained for etch depths greater than 600 nm, we get an actual low temperature

carrier concentration of $6.4 \times 10^{11} \text{ cm}^{-2}$ ($=9.5 \times 10^{10} + 5.4 \times 10^{11}$). As was the case with the previous sample, the actual degenerate carrier densities at low T are much greater than those measured due to the large effect of the surface states. It is worth mentioning again that the uncertainty in the determination of these surface states comes from the large variation in the air data. As stated previously, the surface states, or rather their compensation, may depend greatly on the ambient air environment. It is believed that the *n*-type surface states are destroyed when exposed to air due to the adsorption of some specific atoms or molecules. These atoms or molecules form bonds with the Ge (or Sn) surface atoms effectively 'using up' the excess surface electrons and creating an electrically neutral surface state. The exact species involved in passivating the surface states are unknown at present, although oxygen and hydrogen seem to be plausible candidates. Still, it is obvious that the resulting carrier concentration will depend greatly on the levels of those particular atoms in the environment at that time. Because of this, the results are very sensitive to the ambient conditions and vary significantly from one measurement to the next. This fact may also imply that the surface states are sensitive to Sn content and that the Sn content may vary somewhat throughout the film, e.g. more Sn near the surface.

The results of the differential Hall equations are plotted as a function of etch depth for this sample in Figure 28. Again, there is a large spread (almost one order of magnitude) in the calculated values. As with the $\text{Ge}_{0.9994}\text{Sn}_{0.0006}$ sample, there is a clear increase in carriers near the film-substrate interface which is consistent with the degenerate interfacial layer. The average value for the first 5 etches up to an etch depth of about 700 nm is $8.07 \times 10^{14} \text{ cm}^{-3}$ which is significantly lower than the value of $4.14 \times 10^{15} \text{ cm}^{-3}$ derived from the linear fit to the vacuum data. It is also much lower than the value of $1.76 \times 10^{16} \text{ cm}^{-3}$ given by Table 3. It is obvious that a

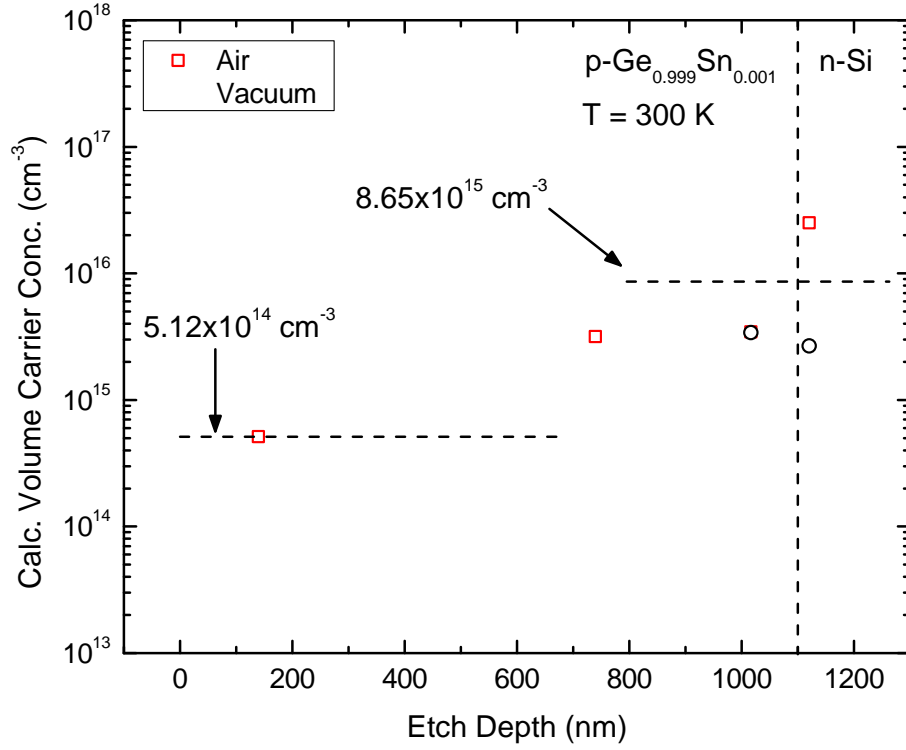


Figure 28. Volume carrier concentration of each removed layer plotted as a function of etch depth for the $p\text{-Ge}_{0.999}\text{Sn}_{0.001}/n\text{-Si}$ sample calculated using the differential Hall model in Eqns. (18)-(22).

simple RT measurement of the carrier density does not give an accurate value for the actual carriers in the film due to the effects of the degenerate interfacial layer as well as the surface states. The average value for the next few etches near the interface is about $1.17 \times 10^{16} \text{ cm}^{-3}$ which again is more than one order of magnitude larger than the calculated carrier concentration in the film. This increase is consistent with a degenerate conducting layer near the interface.

Carrier profiles for selected temperatures are plotted as a function of etch depth in Figure 29. As was the case with the previous sample, the measured carrier concentration was linearly interpolated to give values at a common set of

temperatures, allowing for a comparison of the different carrier depth profiles. As seen in Fig. 29, some of the profiles show a slight decrease with etch depth, while others appear relatively flat. As mentioned previously, for lower temperatures and larger etch depths, the carriers were not measureable. This is also clearly seen in Fig. 24 where the low-T carriers for the later etches are not shown. The volume carrier density in the removed layers was calculated using the differential Hall equations for each set of data. The results of those calculations are shown in Figure 30. As was the case with the RT carriers shown previously, there is a significant amount of fluctuation in the data. Still, it is easy to see that the carrier density remained fairly constant throughout the film, and then increased near the interface. This agrees well with the RT data and once again confirms the presence of a degenerate conducting layer near the interface. The average values in the film and near the interface were $4.35 \times 10^{14} \text{ cm}^{-3}$ and $2.65 \times 10^{15} \text{ cm}^{-3}$, respectively, which are both lower than the values obtained from the RT air and vacuum data. However the increase in carriers from the film to near the interface is still almost one order of magnitude which agrees well with the RT data. Compared to the previous sample, there are fewer good data points for the calculated carrier density. This is probably due to the very small changes in the carriers as a function of etch depth. Looking at Fig. 29 more closely, we can see places where the carriers almost seem to remain the same from one etch to the next, or even increase slightly. Those small fluctuations in the measured data can lead to much larger fluctuations in the calculated values as seen in Fig. 30.

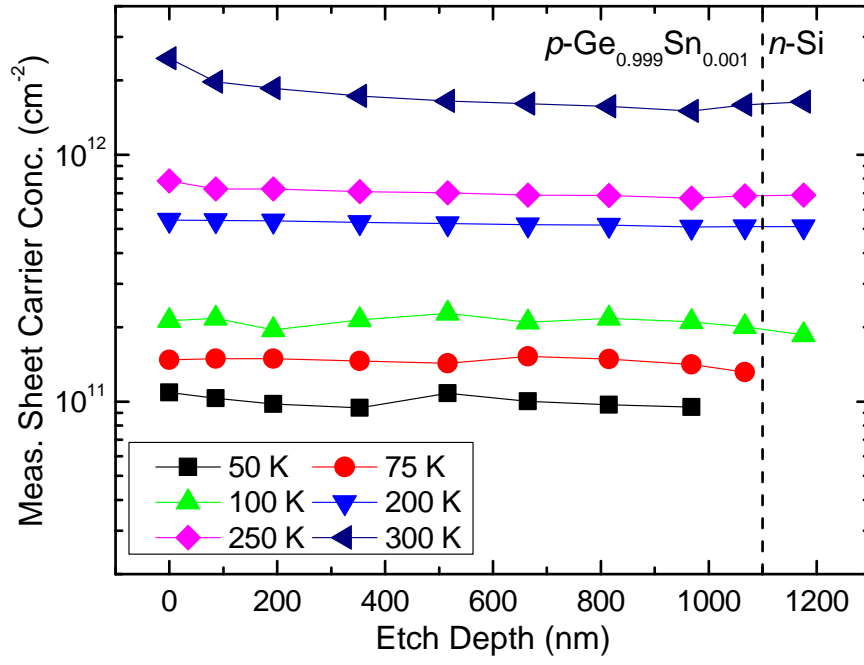


Figure 29. Measured sheet carrier profiles plotted as a function of etch depth at different temperatures for the $\text{Ge}_{0.999}\text{Sn}_{0.001}$ sample.

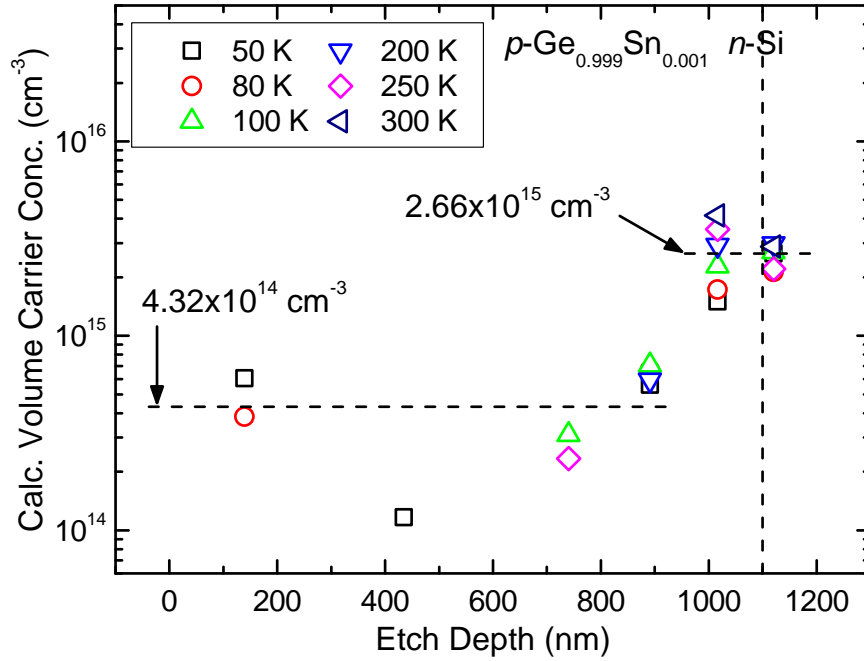


Figure 30. Calculated volume carrier profiles plotted as a function of etch depth at different temperatures for the $\text{Ge}_{0.999}\text{Sn}_{0.001}$ sample.

Analysis of the p -Ge/ n -Si Sample

Etch Studies

The temperature dependent sheet carrier concentration of this p -Ge/ n -Si sample is plotted as a function of inverse temperature for all etches in Figure 31. Carrier profiles for selected temperatures are shown as a function of etch depth in Table 8. This sample shows a different behavior than either of the previous two samples studied. The carrier concentration actually increases with etching, more drastically at low temperatures but still noticeable even at RT. The carriers increased after the first etch (108 nm depth), remained about the same for the next two etches (up to 318 nm depth), then increased again after the 4th etch (391 nm depth) and remained about the same for the 5th etch. Finally, after the 6th etch (542 nm depth), the carriers increased dramatically at all temperatures. It is worth mentioning here that Mavroidis et al [46] saw a similar increase in carriers as a function of etch depth in Si-doped n -GaN/ Al_2O_3 samples. They explained it as an artifact of the multilayer conduction. Subsequent calculations verified that fact and showed that the change in carrier concentration can be significantly affected by the change in mobility.

Table 8. Measured sheet carrier concentration in cm^{-2} as a function of etch depth at selected temperatures for the p -Ge/ n -Si sample.

Etch Depth (nm)	Temperature				
	50 K	75 K	100 K	200 K	250 K
0	6.333×10^{11}	6.997×10^{11}	8.120×10^{11}	1.347×10^{12}	1.575×10^{12}
108	6.708×10^{11}	7.657×10^{11}	9.238×10^{11}	1.549×10^{12}	1.821×10^{12}
219	7.093×10^{11}	7.558×10^{11}	9.057×10^{11}	1.549×10^{12}	1.798×10^{12}
318	7.796×10^{11}	8.093×10^{11}	9.652×10^{11}	1.613×10^{12}	1.843×10^{12}
391	8.168×10^{11}	8.008×10^{11}	9.488×10^{11}	1.610×10^{12}	1.881×10^{12}
469	9.025×10^{11}	8.061×10^{11}	1.074×10^{12}	1.596×10^{12}	1.887×10^{12}
541	1.044×10^{12}	1.203×10^{12}	1.189×10^{12}	1.741×10^{12}	2.035×10^{12}

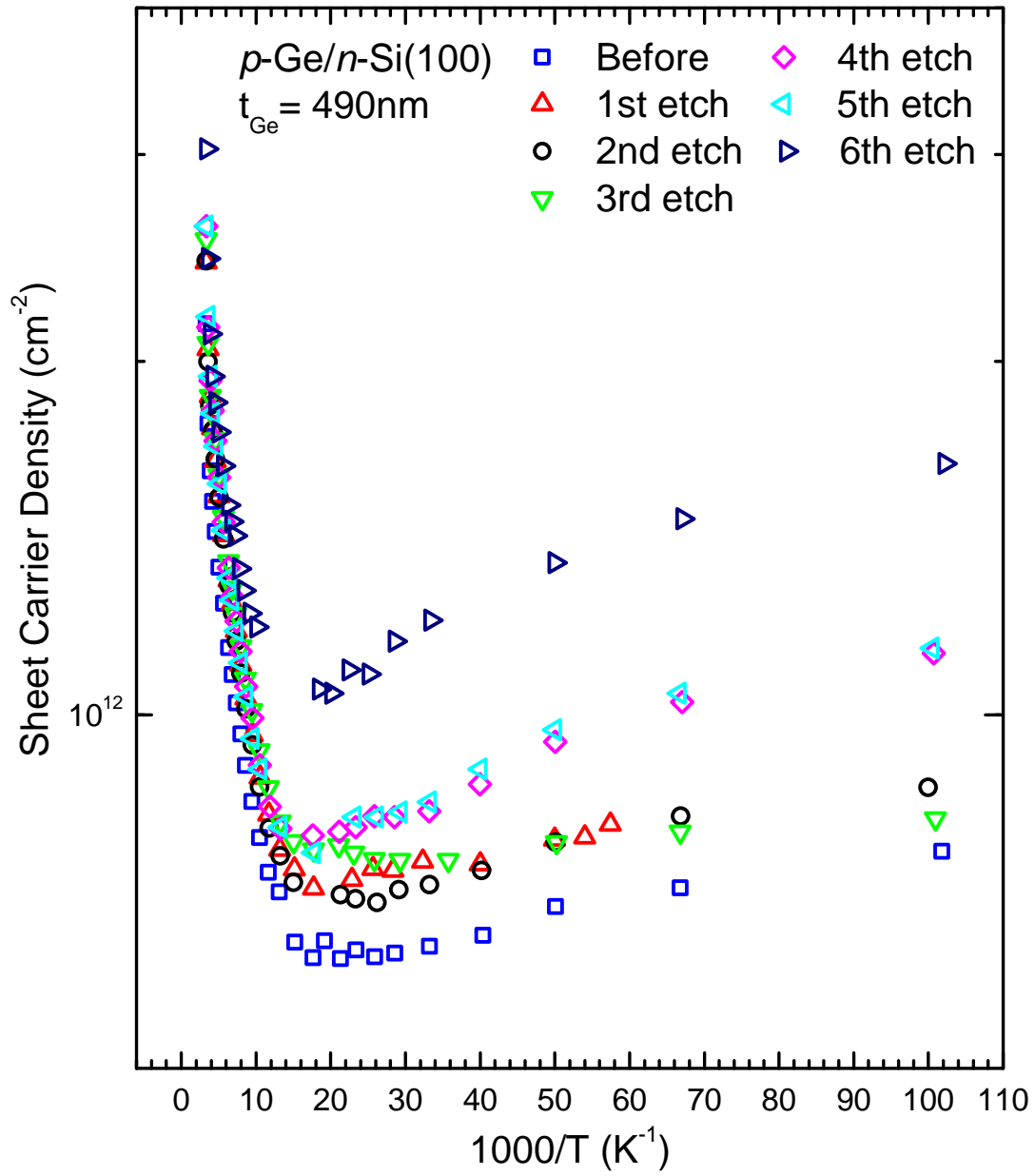


Figure 31. Sheet carrier concentration plotted as a function of inverse temperature for the $p\text{-Ge}/n\text{-Si}$ sample for all etches.

The temperature dependent mobilities of this p -Ge/ n -Si sample are plotted as a function of temperature in Figure 31 for all etches. A substantial decrease with etch depth is observed for the mobility at all temperatures. Unlike the carrier concentration, a clear change is observed between all etches. For instance, there is a large decrease between the 2nd and 3rd etch for temperatures between 50 and 300 K, however little to no change was observed in the carrier concentration between those two etches. The decrease in mobility is more pronounced in the intermediate temperature region with the peak mobility reduced to 1/2 of it's original value by about the 4th etch (391 nm depth). The LT mobilities do not change as much until the 4th etch where a significant decrease is observed. The increase in the LT mobility between the 2nd to 3rd etches is puzzling and goes against the trend of the rest of the data. This could have been caused by some less than perfect thermal contact during the 3rd etch which would have resulted in a slightly higher sample temperature and therefore a slightly higher mobility than expected. Overall, the slope of the mobilities at low temperatures seemed to decrease with etch depth. The mobility curves were fit using Matheison's rule and low-T slopes of $T^{1.60}$ before etching and $T^{1.50}$ after the 6th etch were obtained. The mobilities seem to converge somewhat for higher temperatures, especially for etches 3-5. Still the slopes at higher temperatures seem to increase (decrease in a negative sense) with etch depth. Fits of the mobility curves gave high-T slopes of $T^{-2.16}$ before etching and $T^{-1.67}$ after the 6th etch. Strictly speaking, we should use the two layer model described earlier and fit the carrier concentration and mobility simultaneously. This would remove the effect of the degenerate conducting layer at low-T and account for the slightly higher mobility at 10 K. Still, we can get a good idea of how the temperature dependence of the mobility changes with etch depth by doing a simple fit using Matheison's rule.

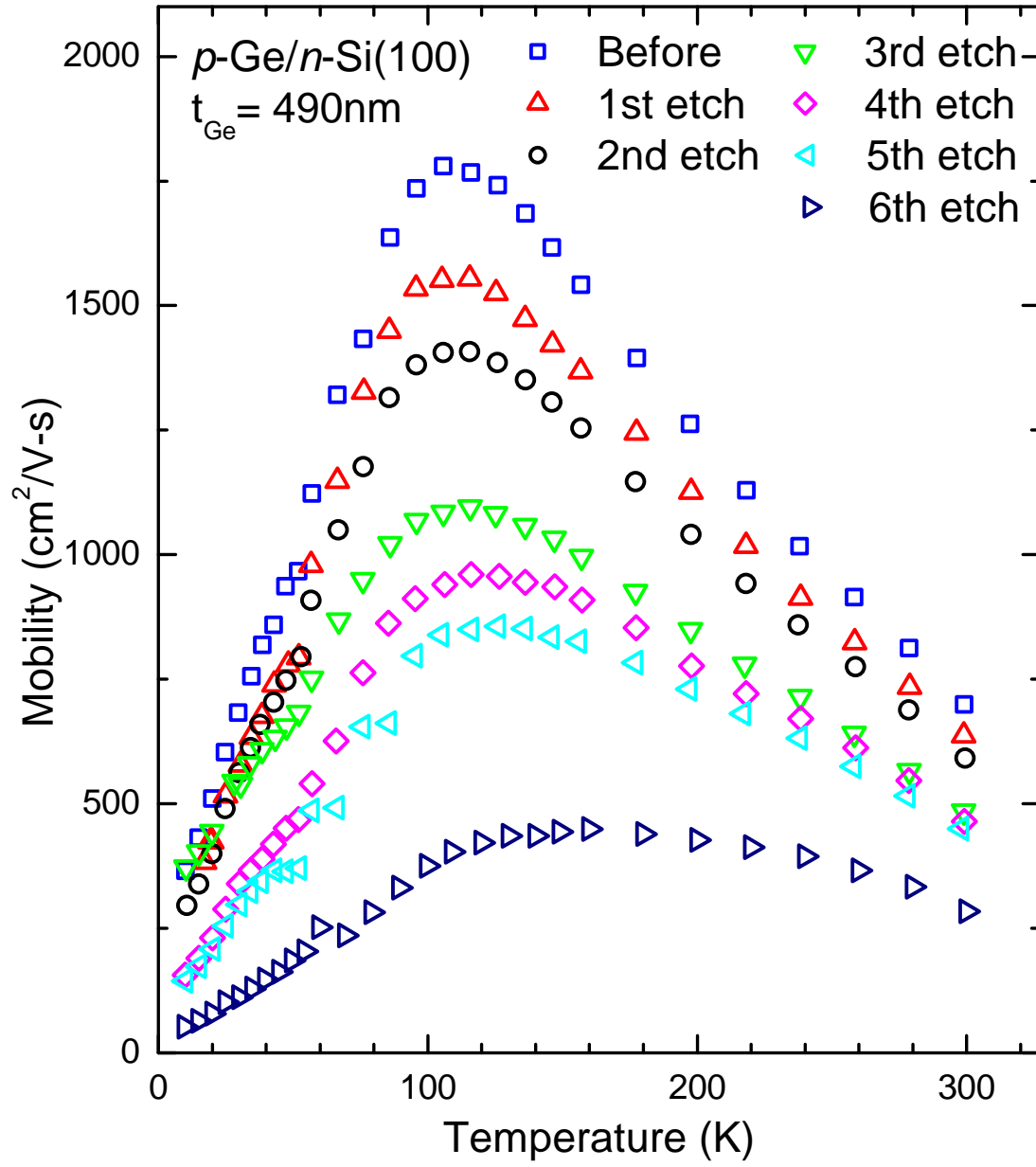


Figure 32. Carrier mobility plotted as a function of temperature for the *p*-Ge/*n*-Si sample for all etches.

There is a kink in the mobility at around 50 K which becomes more obvious with increasing etch depth. This may be due to competing terms such as ionized impurity scattering and scattering at the Ge/Si interface. However, to investigate this further would require fitting the mobility data with all the relevant scattering mechanisms including ionized impurities, optical phonon modes, deformation potential acoustic phonon modes, charged dislocations, surface roughness, space charge region, etc. Even if the appropriate terms to include were determined, the fitting would not be straightforward. The parameters needed for the different scattering equations are well known for the case of bulk Ge, but it is unclear how they would change for this tensile-strained Ge/Si sample. The temperature dependence of the strain could also have an effect here. For those reasons, a full fit of the mobility was not attempted and we've restricted ourselves to a more qualitative discussion of the behavior.

The log of the conductivity for this p -Ge/ n -Si sample is plotted as a function of inverse temperature for all etches in Figure 33. The conductivity shows a very different temperature dependence for this sample compared with the two p -Ge_{1-y}Sn_y/ n -Si samples discussed previously. The conductivity does increase with temperature showing two distinct slopes corresponding to the shallow and deep acceptors, however it then reaches a maximum around 160 – 180 K after which it decreases slightly up to 300 K. This is in contrast to the Ge_{1-y}Sn_y samples where the conductivity increased continuously with increasing temperature.

Also, the overall change in conductivity was not as large for this sample. Specifically, from LT to the peak temperature, the log conductivity increased from about -4.40 to about -3.65, a relative difference of only 17%. For the Ge_{0.9994}Sn_{0.0006} sample, the log conductivity was -5.20 and -3.75 at LT and RT respectively, for a relative difference of about 28 %. This difference increased with etching to almost 40 % by the 5th etch for that Ge_{1-y}Sn_y sample. In contrast, for this sample, the

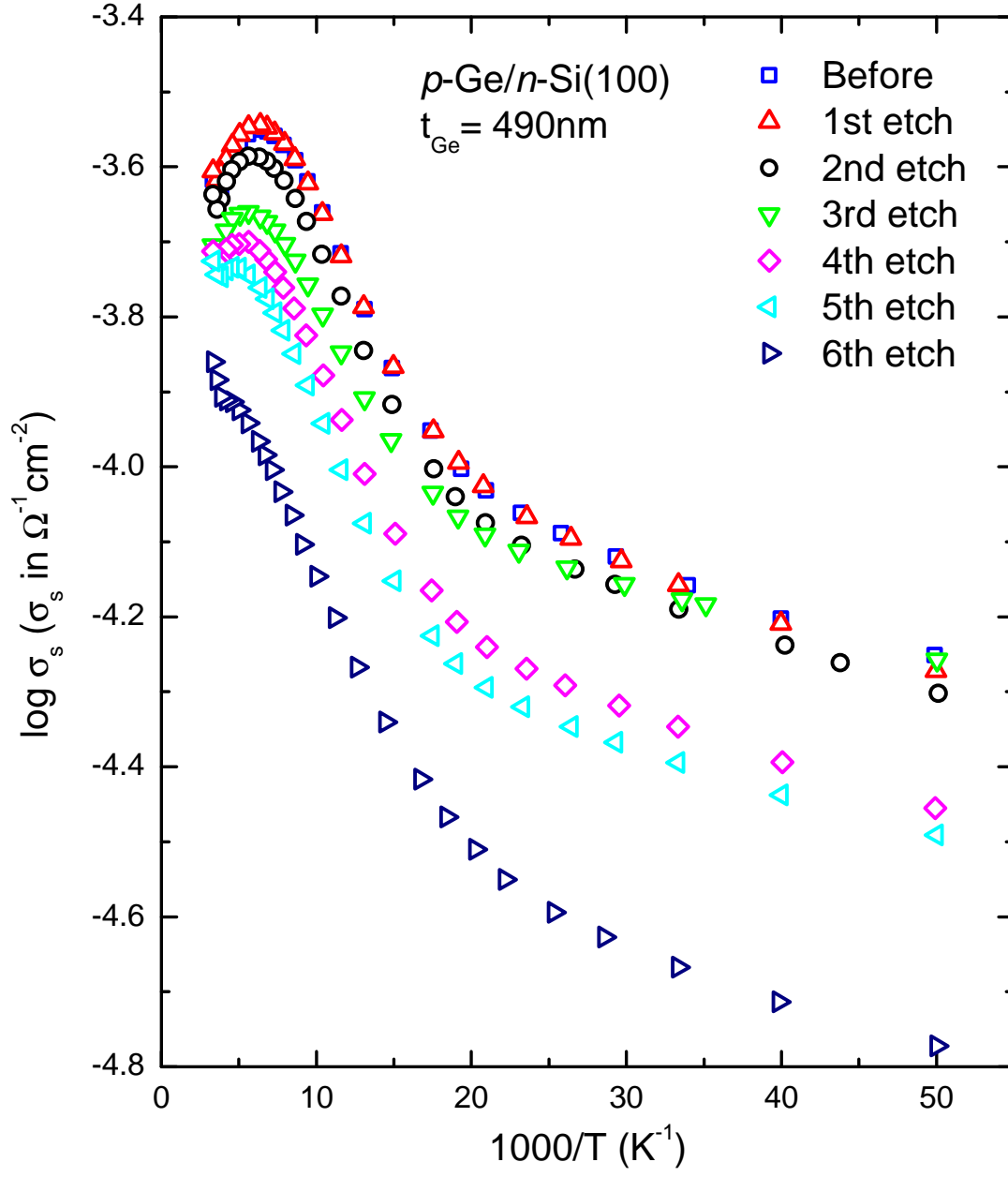


Figure 33. Log conductivity plotted as a function of inverse temperature for the *p*-Ge/*n*-Si sample for all etches.

relative difference remains about the same for all etches. The conductivities are rather shifted with increasing etch depth. As with the carrier concentration, not much change is observed between the first few etches, with a large change after the 4th etch.

The RT carrier concentration for this p -Ge/ n -Si sample is plotted as a function of etch depth in Figure 34 for both air and vacuum with the corresponding data shown in Table 9. As was the case with the temperature dependent data, the RT carrier concentration is observed to increase with etch depth. The second etch does not seem to follow the trend of the rest of the data, and both values seem lower than the average. Etches 1, 3, 4, and 5 on the other hand all seem to show the same trend increasing at about the same rate with a similar offset between air and vacuum.

Simultaneous linear fits of the air and vacuum data were performed with the constraint that the slopes match. The results are plotted as solid lines in Fig. 34. The slope obtained from the fit was $+1.14 \times 10^9 \text{ cm}^{-2}/\text{nm}$, which corresponds to an estimated increased volume carrier density of $1.14 \times 10^{16} \text{ cm}^{-3}$ in the Ge layer. The surface state (n -type) carrier density, given by the offset between the two lines, was only $9.7 \times 10^{10} \text{ cm}^{-2}$ for this sample, which is more than one order of magnitude smaller than the surface state density of the $\text{Ge}_{1-y}\text{Sn}_y$ samples studied. From Fig. 31, we can see that the measured (vacuum) carrier concentration at LT, p_{meas} , was about $7.6 \times 10^{11} \text{ cm}^{-2}$ for this Ge/Si sample. This means that the actual low temperature degenerate carrier concentration, p_{degen} , could be about $8.6 \times 10^{11} \text{ cm}^{-2}$ ($p_{\text{meas}} + n_{\text{surf}} = 7.6 \times 10^{11} + 9.7 \times 10^{10}$). This is significantly less than the values of $1.06 \times 10^{12} \text{ cm}^{-2}$ and $6.4 \times 10^{11} \text{ cm}^{-2}$ obtained for the $\text{Ge}_{0.9994}\text{Sn}_{0.0006}$ and $\text{Ge}_{0.999}\text{Sn}_{0.001}$ samples, respectively.

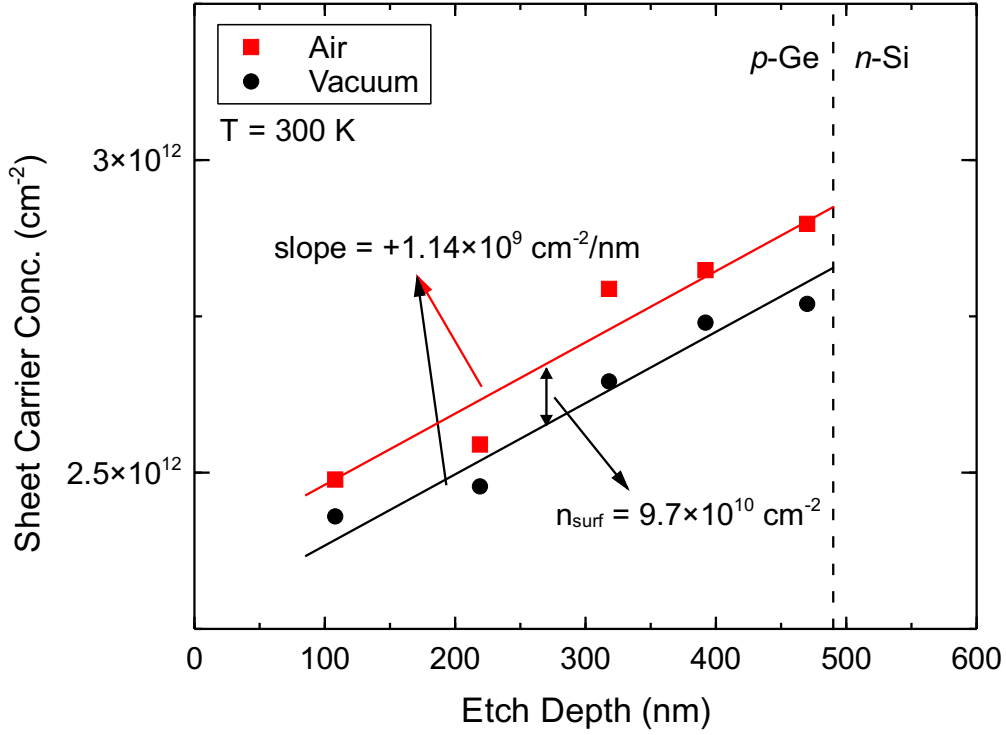


Figure 34. Room temperature sheet carrier concentration plotted as a function of etch depth for the p -Ge/ n -Si sample.

Table 9. Sheet carrier concentration measured at RT in both air and vacuum as a function of etch depth for the p -Ge/ n -Si sample.

Etch Depth, d (nm)	Carrier Conc. in Air, p_{air} (cm ⁻²)	Carrier Conc. in Vacuum, p_{vac} (cm ⁻²)	Surface State Density, n_{surf} (cm ⁻²)
0	2.162×10^{12}	2.228×10^{12}	3.210×10^{10}
108	2.489×10^{12}	2.430×10^{12}	5.938×10^{10}
219	2.545×10^{12}	2.478×10^{12}	6.740×10^{10}
318	2.794×10^{12}	2.646×10^{12}	1.480×10^{11}
392	2.824×10^{12}	2.740×10^{12}	8.465×10^{10}
470	2.898×10^{12}	2.770×10^{12}	1.280×10^{11}
542	3.177×10^{12}	3.135×10^{12}	4.213×10^{10}

The results of the differential Hall equations are plotted as a function of etch depth for this sample in Figure 35. Fortunately, even though there was an increase in the measured carrier concentration with increasing etch depth, all of the calculated values for the volume carrier density came out positive which is a very encouraging result. For etch depths up to about 430 nm, the average value was $8.65 \times 10^{15} \text{ cm}^{-3}$ which again is lower than the value of $1.14 \times 10^{16} \text{ cm}^{-3}$ obtained from the linear fits. Near the interface, the average was $5.29 \times 10^{16} \text{ cm}^{-3}$ which is much higher than the value in the film. Again, this is an indication of a degenerate conducting layer in the interfacial region.

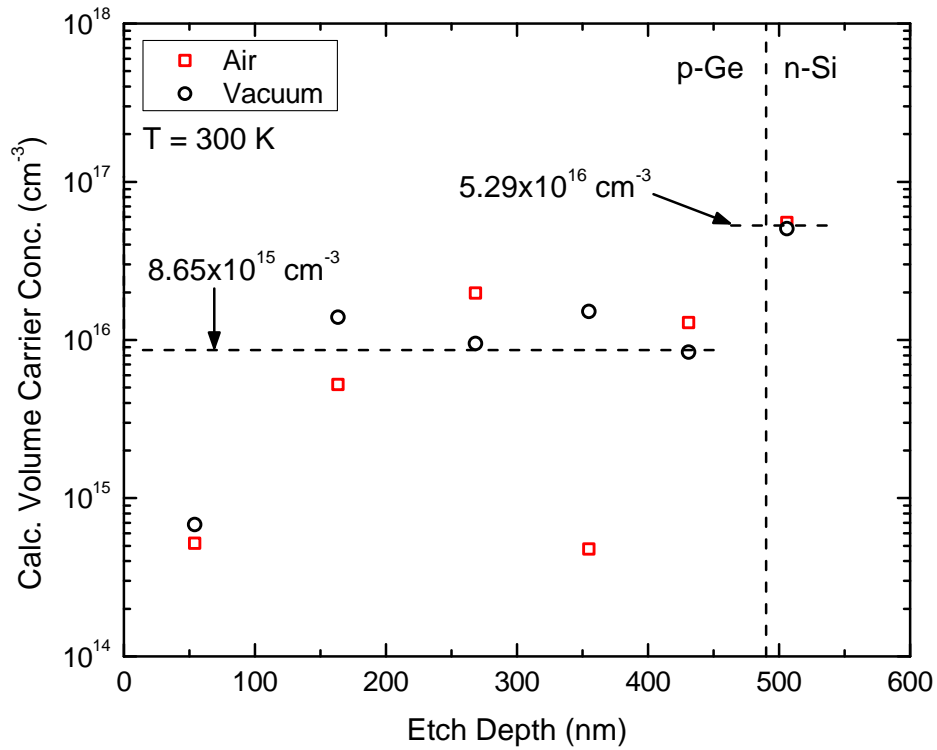


Figure 35. Volume carrier concentration of each removed layer plotted as a function of etch depth for the *p*-Ge/*n*-Si sample calculated using the differential Hall model in Eqns. (18)-(22).

Carrier profiles are plotted as a function of etch depth for selected temperatures in Figure 36. The measured carrier concentration was interpolated as before at a common set of temperatures, which is necessary to compare data from different etches. As seen in Fig. 36, most of the profiles show an increase with etch depth which is consistent with the carrier depth profile. Again, this is believed to be an artifact of the multilayer conduction similar to what was reported by Mavroidis et al [46] Unlike the previous two $\text{Ge}_{1-y}\text{Sn}_y$ samples, the data for this sample was measureable at low temperatures throughout all of the etches. There were however some data points in the intermediate region (near 75 K) that were not measureable and for that reason were not shown in Fig. 31. The volume carrier density in each of the removed layers was calculated using the differential Hall equations, with the equations being applied separately for each selected temperature. The results of the differential Hall calculations are shown in Figure 37. All of the calculated values came out positive, confirming that the removed layers were p -type in spite of the measured increase in carriers with etching. The positive results are mainly due to the fact that the resistivity (or mobility) is involved in the calculation in addition to the carrier concentration. As was the case with the previous two samples, there was a significant amount of fluctuation in the calculated carrier concentration. Still, the results show the same trend where the carrier density remains fairly constant throughout the film, and then increases sharply near the interface. The average value for the first few etches was $6.6 \times 10^{15} \text{ cm}^{-3}$, much less than the value of $5.9 \times 10^{16} \text{ cm}^{-3}$ given by Table 3. That value was obtained by simply dividing the RT sheet carriers (measured in vacuum) by the film thickness of 490 nm. Closer to the interface, the average calculated value was $4.1 \times 10^{16} \text{ cm}^{-3}$. Again, the carriers near the interface are about one order of magnitude higher than those in the film, which generally agrees with the RT data.

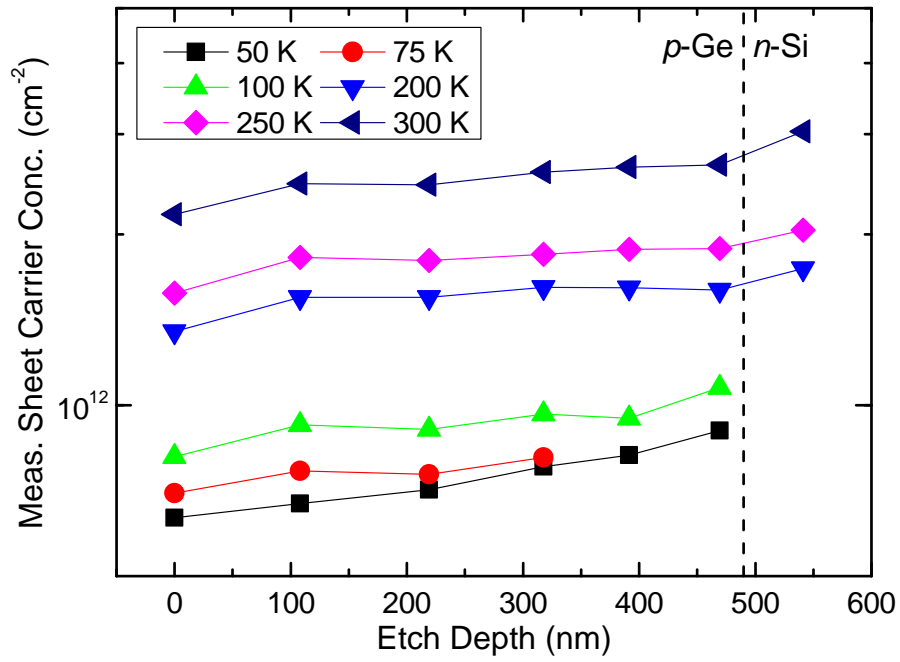


Figure 36. Measured sheet carrier profiles plotted as a function of etch depth at different temperatures for the Ge/Si sample.

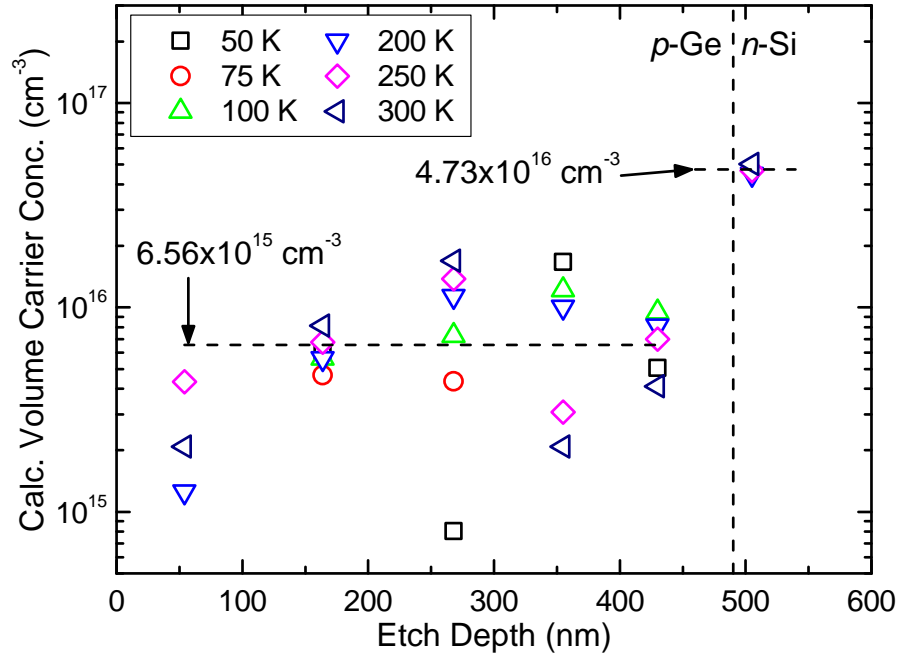


Figure 37. Calculated volume carrier profiles plotted as a function of etch depth at different temperatures for the Ge/Si sample.

Hall-Effect Measurements of $p\text{-Ge}_{0.90}\text{Si}_{0.08}\text{Sn}_{0.02}/p\text{-Ge}$

Temperature-dependent Hall-effect measurements were carried out on a set of $p\text{-Ge}_{0.90}\text{Si}_{0.08}\text{Sn}_{0.02}$ samples grown on $p\text{-Ge}$ substrates ($\rho = 0.04 \text{ } \Omega\text{-cm}$). The Ge substrates were $150 - \mu\text{m}$ -thick Ge(100) wafers miscut 6° relative to (111), and highly doped with Ga acceptor atoms ($p = 6 \times 10^{17} \text{ cm}^{-3}$), which are typically used as platforms for multijunction solar cells. One of the $\text{Ge}_{0.90}\text{Si}_{0.08}\text{Sn}_{0.02}$ samples was undoped and the other three samples were *in-situ* doped with boron at levels of 3×10^{17} , 7×10^{17} , and $1 \times 10^{18} \text{ cm}^{-3}$, respectively. The samples were not annealed. Both Cr/Au and indium contacts were used and both showed good ohmic behavior and similar Hall voltages. The temperature-dependent sheet carrier concentrations for the samples with Cr/Au contacts are shown in Figure 38. At temperatures below about 50 K, the carriers are relatively temperature independent, i.e. degenerate. After initially decreasing, the carriers begin to increase slightly as the temperature increases from about 100 K to 300 K. Above around 450 K, the carriers start to increase exponentially in the intrinsic regime as seen in the far left side of the figure. Additionally, a conductivity-type conversion from p - to n -type occurred for the $p\text{-Ge}$ substrate, undoped $\text{Ge}_{0.90}\text{Si}_{0.08}\text{Sn}_{0.02}$, and $p\text{-Ge}_{0.90}\text{Si}_{0.08}\text{Sn}_{0.02}$ ($1 \times 10^{18} \text{ cm}^{-3}$) samples at temperatures of 550 K, 675 K, and 640 K, respectively. The other samples may show a similar type conversion at higher temperatures. The lower type conversion temperature seen in the Ge substrate may be due to a larger electron mobility in the bulk sample compared to that in the epilayers.

For the $p\text{-Ge}(\text{Sn})/n\text{-Si}$ samples previously studied, the source of the degenerate conduction seemed to be in the interfacial region, probably arising from the dislocations at the mismatched Ge(Sn)-Si interface. However, an interfacial conducting layer is not likely for these $p\text{-Ge}_{0.90}\text{Si}_{0.08}\text{Sn}_{0.02}/p\text{-Ge}$ samples since the epilayers were lattice-matched to the Ge substrate. This was accomplished by

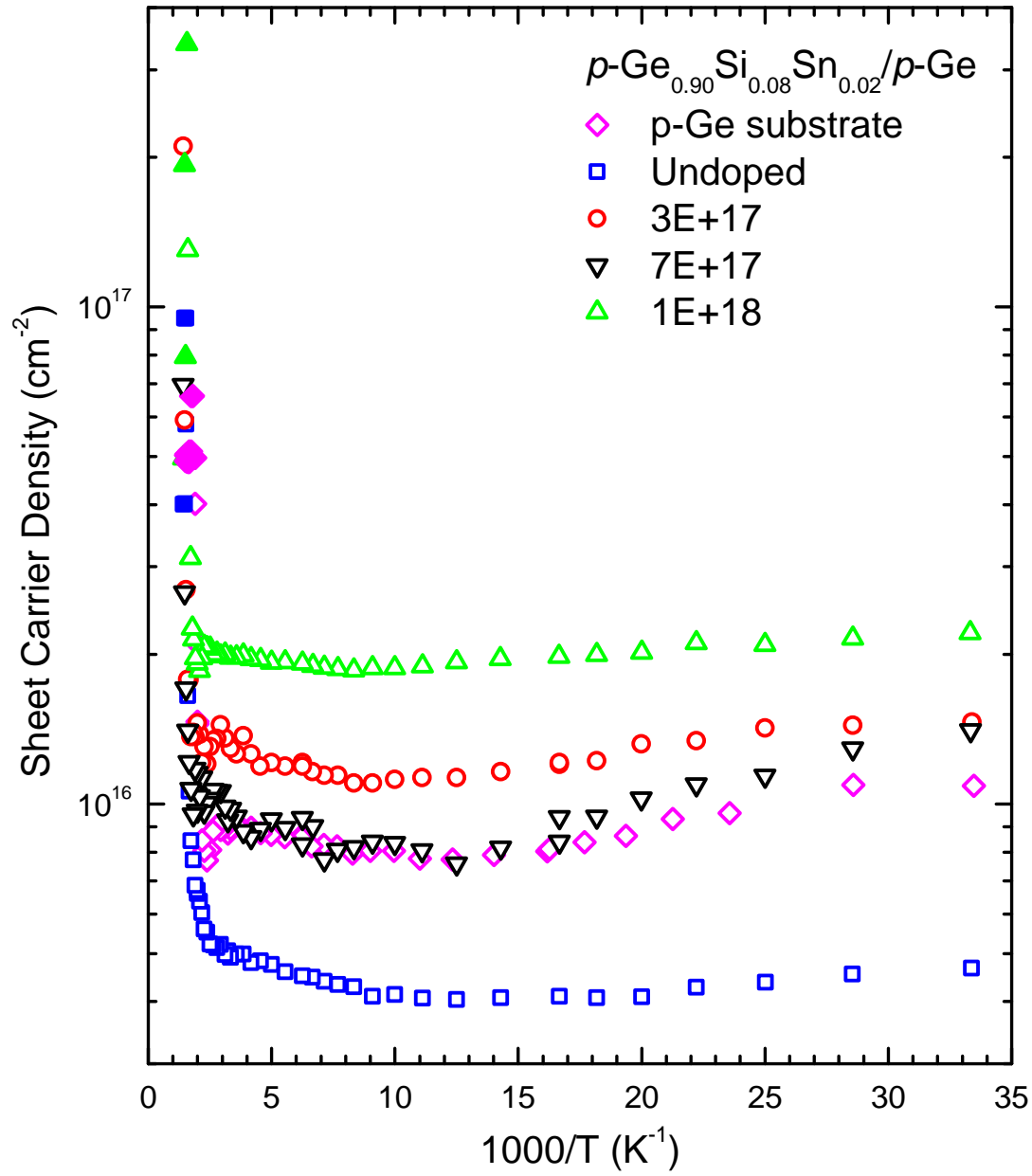


Figure 38. Sheet carrier concentration plotted as a function of inverse temperature for undoped and p -type doped $\text{Ge}_{0.90}\text{Si}_{0.08}\text{Sn}_{0.02}/p\text{-Ge}$ samples along with the $p\text{-Ge}$ substrate. Open symbols indicate p -type conductivity, while closed symbols indicate n -type conductivity.

adjusting the Si and Sn compositions in the alloy. Subsequent HRXRD measurements confirmed that the $\text{Ge}_{0.90}\text{Si}_{0.08}\text{Sn}_{0.02}$ layers were indeed lattice-matched to the substrate and had a fully relaxed strain state. Furthermore, XTEM images of the samples showed a perfectly smooth interface and no edge type dislocations were observed. The degenerate conduction in these samples seems to come at least in part from the p -Ge substrate. In fact, it is very clear from Fig. 38 that the effect of the p -Ge is significant. The temperature dependence of all the epilayer samples match almost exactly to that of the substrate, with the only difference being the absolute value of the carrier density. It is reasonable to conclude then that the observed degenerate behavior is largely affected by the doped p -Ge substrate and not by an interfacial conducting layer. Unfortunately, this substrate conduction makes the determination of the actual electrical properties of the $\text{Ge}_{0.90}\text{Si}_{0.08}\text{Sn}_{0.02}$ films alone much more difficult. It is worth mentioning here that for the doped samples, there is some degenerate conduction from the film itself since the doping levels are fairly high ($3 \times 10^{17} - 1 \times 10^{18} \text{ cm}^{-3}$). In fact, the concentrations of both the doped epilayers and the p -Ge substrate are close to the Mott density for holes in Ge which is calculated to be about $8.82 \times 10^{17} \text{ cm}^{-3}$ using a density of states effective mass of $m_h = 0.34m_0$. For the undoped sample on the other hand, the measured carriers are lower than those of the Ge substrate. This is somewhat counter-intuitive since one would expect the undoped epilayer with minimal carriers to have an insignificant impact on the total measured carrier concentration. In other words, we would expect the values measured for the undoped $\text{Ge}_{0.90}\text{Si}_{0.08}\text{Sn}_{0.02}$ / p -Ge to be almost exactly the same as the values measured for the p -Ge substrate alone. However, this is not the case. It could be that the undoped epilayer provides some additional series resistance to the current which is attempting to flow from the contacts, down through the epilayer and into

the substrate. This increased resistance could lead to larger measured Hall voltages which would result in a lower measured value of the carrier concentration for this $\text{Ge}_{0.90}\text{Si}_{0.08}\text{Sn}_{0.02}$ /*p*-Ge sample.

The mobilities of these $\text{Ge}_{0.90}\text{Si}_{0.08}\text{Sn}_{0.02}$ samples are plotted as a function of temperature in Figure 39. The undoped sample showed the highest mobility up to temperatures of about 500 K and had a peak mobility of about $1,030 \text{ cm}^2/(\text{V}\cdot\text{s})$ at 120 K. A fit of the mobility curve using Matheison's rule for the undoped sample gave a $T^{0.74}$ dependence at low-T (below 120 K) and a $T^{-1.65}$ dependence at high-T (above 120 K). The best fit was obtained by excluding the data above about 450 K where the mobility started decreasing more rapidly due to the type conversion. The Ge substrate had a peak mobility of about $690 \text{ cm}^2/(\text{V}\cdot\text{s})$ at 130 K which was significantly lower than the undoped sample, but still higher than all of the doped samples. A fit of the mobility curve for the *p*-Ge substrate yielded a $T^{1.53}$ dependence at low-T (below 130 K) and a $T^{-1.38}$ dependence at high-T (above 130 K). The best fit was obtained by excluding the data above about 400 K where the affect of the type conversion became significant. This low-T behavior for the *p*-Ge substrate is much closer to the theoretical $T^{3/2}$ dependence expected for ionized impurity scattering.

The log conductivity for these $\text{Ge}_{0.90}\text{Si}_{0.08}\text{Sn}_{0.02}$ samples are plotted as a function of inverse temperature in Figure 40. At low temperatures, the conductivity of the Ge substrate and the undoped $\text{Ge}_{0.90}\text{Si}_{0.08}\text{Sn}_{0.02}$ sample are almost identical. For temperatures above about 70 K, however, the values start to diverge. The temperature dependent conductivity of all the samples have a very similar shape. The nearly flat region at low temperatures is due to the degenerate conduction. The conductivities then increase mainly due to an increase in the mobility, reaching a peak near 150 K, and then start to decrease rapidly due to the large decrease in the

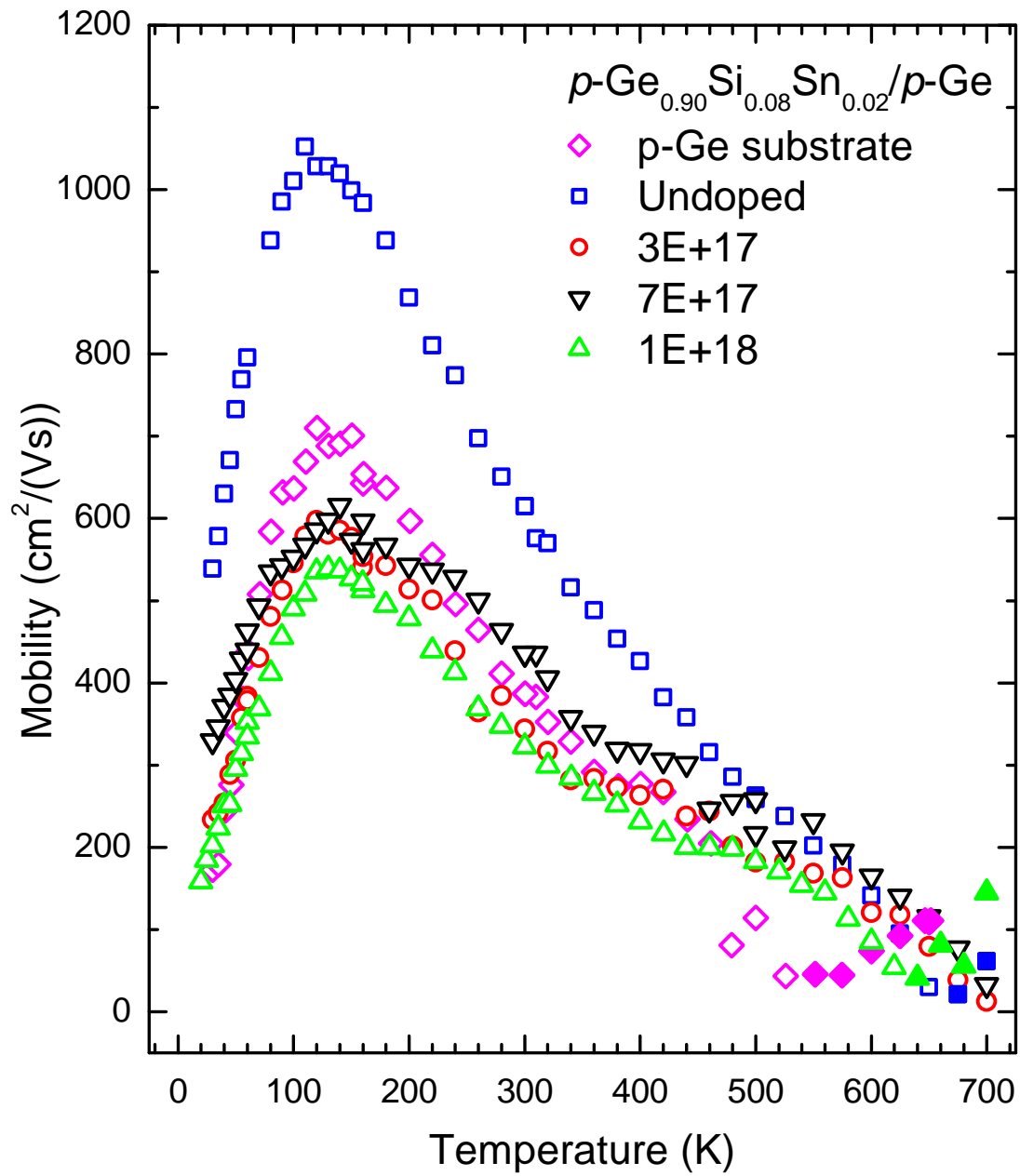


Figure 39. Carrier mobility plotted as a function of temperature for undoped and *p*-type doped $\text{Ge}_{0.90}\text{Si}_{0.08}\text{Sn}_{0.02}/p\text{-Ge}$ samples along with the *p*-Ge substrate. Open symbols indicate *p*-type conductivity, while closed symbols indicate *n*-type conductivity.

mobility. At temperatures below about 150 K, the increase in the conductivity is predominantly caused by the increase in the mobility since the carriers are relatively constant in this temperature range. Above about 150 K, the carriers increase slightly, but the mobility decreases more quickly, and so the conductivity as well. Finally, the conductivity undergoes a sharp transition and begins to increase dramatically in the intrinsic region. This onset occurs at 500 K for the Ge substrate, just before the type conversion in the carrier concentration. The Ge substrate also shows the greatest increase in conductivity in the intrinsic region which again is due to a larger electron mobility in the bulk sample.

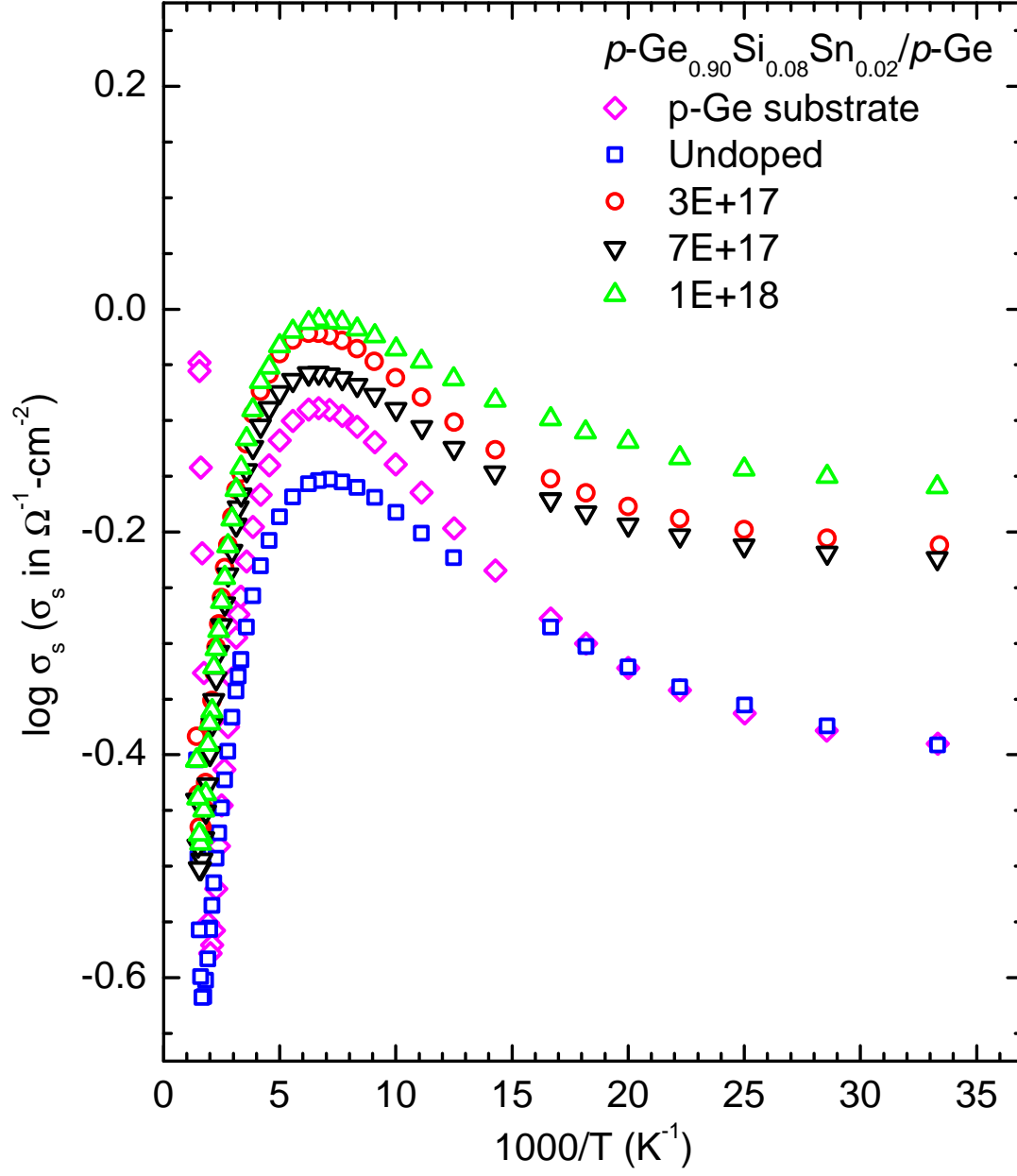


Figure 40. Log conductivity plotted as a function of inverse temperature for undoped and p -type doped $\text{Ge}_{0.90}\text{Si}_{0.08}\text{Sn}_{0.02}/\text{p-Ge}$ samples along with the p -Ge substrate.

Analysis of the $p\text{-Ge}_{0.90}\text{Si}_{0.08}\text{Sn}_{0.02}/p\text{-Ge}$ ($1 \times 10^{18} \text{ cm}^{-3}$) Sample

Etch Studies

To further investigate the source of the degenerate conduction and to determine the properties of the $\text{Ge}_{1-x-y}\text{Si}_x\text{Sn}_y$ layer alone, etch studies were performed on selected samples with temperature-dependent Hall-effect measurements made at low temperatures (10 – 300 K) after each etch. As with the $p\text{-Ge}(\text{Sn})/n\text{-Si}$ samples, a measurable contribution from surface states was observed. These were again quantified by performing room-temperature Hall-effect measurements in both ambient (air) and in vacuum with the surface state density given by the difference in the carrier density. The sheet carrier concentration for this $p\text{-Ge}_{0.90}\text{Si}_{0.08}\text{Sn}_{0.02}/p\text{-Ge}$ ($p_0 = 10^{18} \text{ cm}^{-3}$) sample is plotted as a function of inverse temperature in Figure 41 for all etches. The carriers at almost all temperatures showed some change as the etches progressed, however they do not show a consistent decrease or increase with etch depth. We can however examine the low temperature carriers and consider the effect of the surface states. The measured p -type carrier concentration, p_{meas} , will be given by: $p_{\text{meas}} = p_{\text{degen}} - n_{\text{surf}}$, where p_{degen} could be a combination of carriers from the doped $\text{Ge}_{0.90}\text{Si}_{0.08}\text{Sn}_{0.02}$ layer and the $p\text{-Ge}$ substrate, and where n_{surf} is the n -type surface state density.

The mobility of this $\text{Ge}_{0.90}\text{Si}_{0.08}\text{Sn}_{0.02}/p\text{-Ge}$ sample is plotted as a function of temperature for all etches in Figure 42. Again, there was not a clear change as a function of etch depth with the exception of the 1st and 6th etches which had slightly higher mobilities at low temperatures. It is not clear however if these increases were a result of a real change in the sample or if the data is simply no good. Since the etches before and after those two (i.e. Before etching, 2nd, 5th, and 7th etches) all showed lower mobilities, it is reasonable to conclude that this data was anomalous and not indicative of any true change in the mobility.

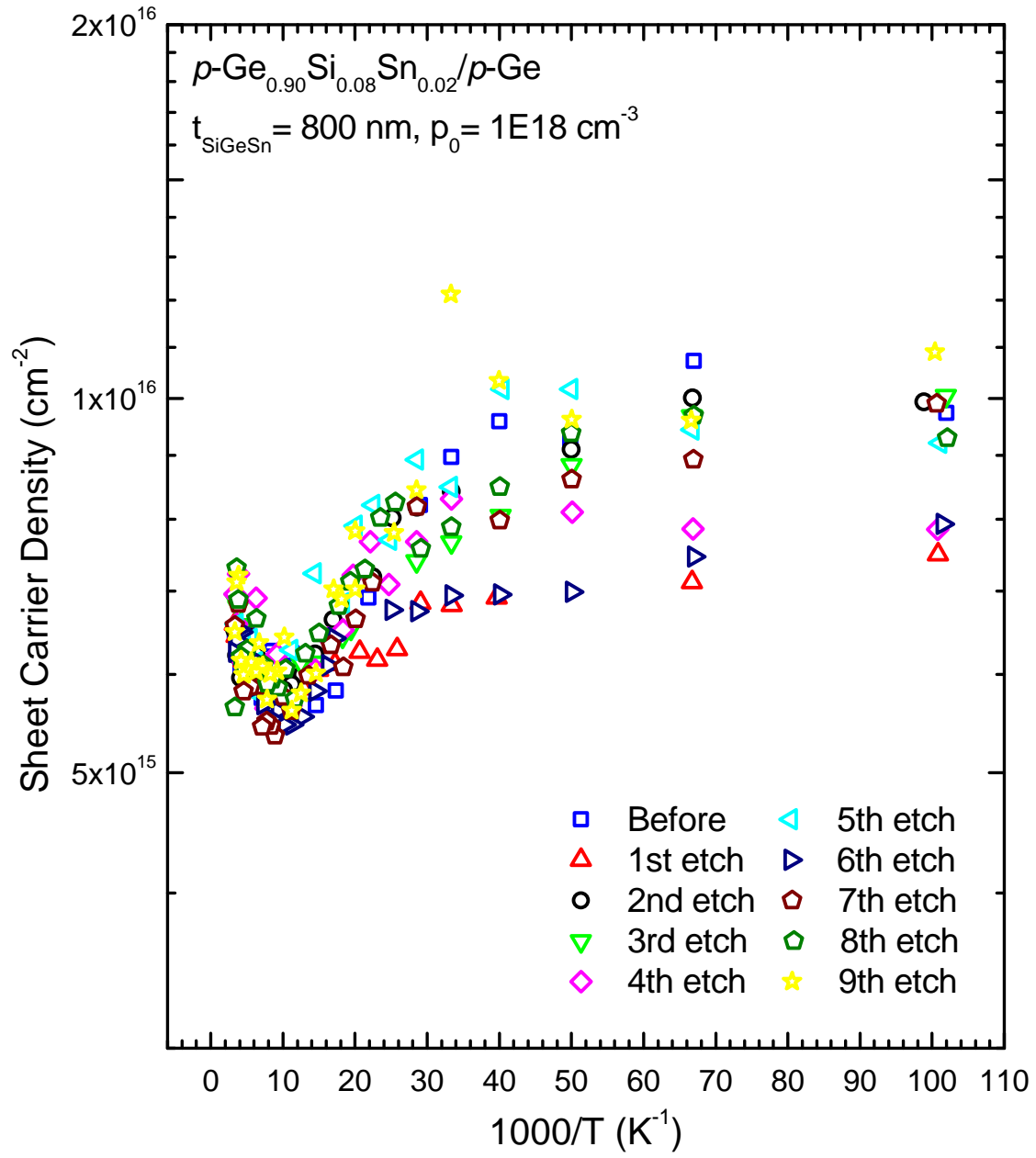


Figure 41. Sheet carrier concentration plotted as a function of inverse temperature for the $p\text{-Ge}_{0.90}\text{Si}_{0.08}\text{Sn}_{0.02}/p\text{-Ge}$ sample for all etches.

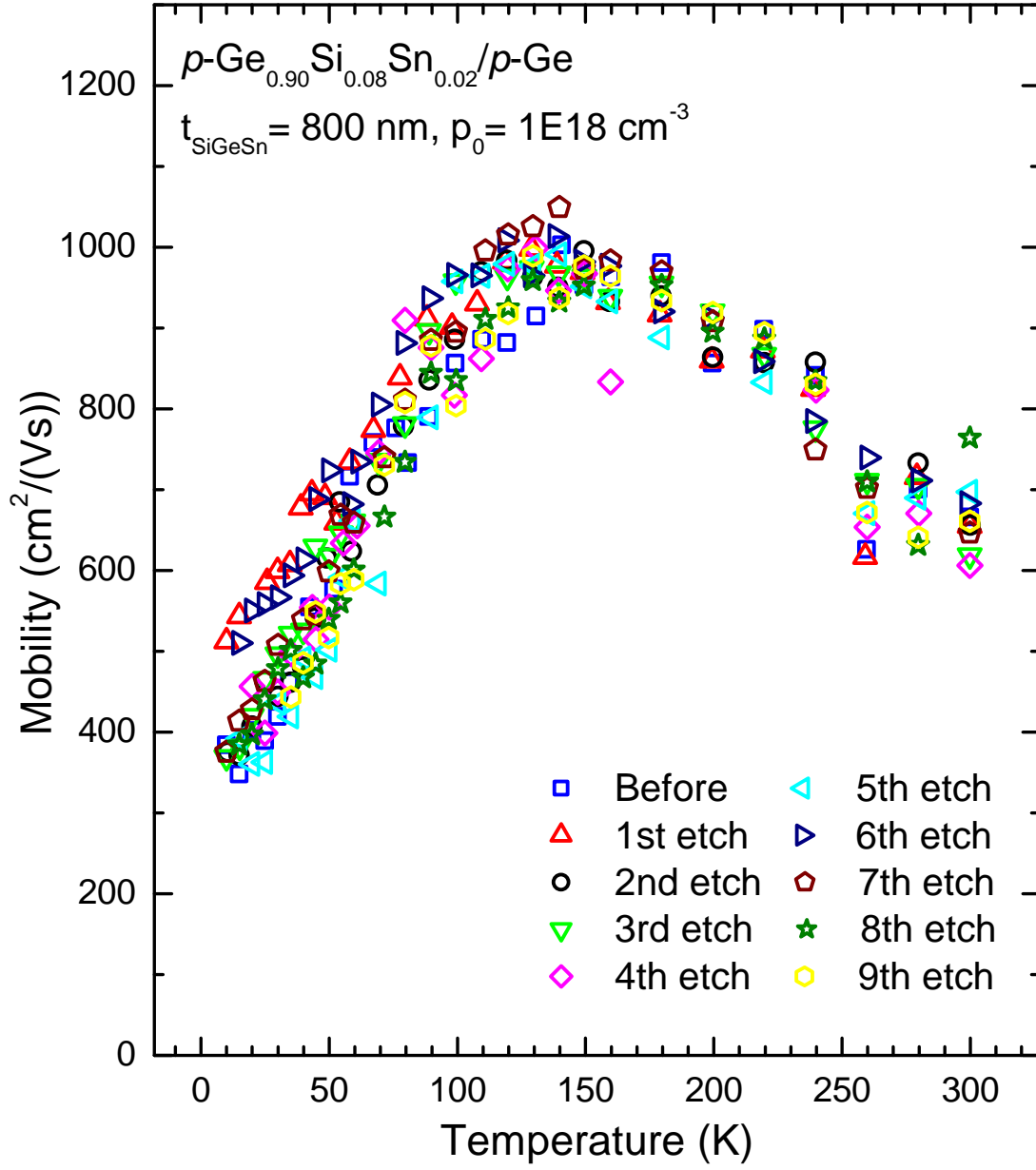


Figure 42. Carrier mobility plotted as a function of temperature for the $p\text{-Ge}_{0.90}\text{Si}_{0.08}\text{Sn}_{0.02}/p\text{-Ge}$ sample for all etches.

The log conductivity of this $\text{Ge}_{0.90}\text{Si}_{0.08}\text{Sn}_{0.02}/p\text{-Ge}$ sample is plotted as a function of inverse temperature for all etches in Figure 43. There is not much measurable change in the conductivity as a function of etch depth either. Again, the 1st and 6th etches showed slightly higher conductivities at low temperatures, but they seem to be the exception. Overall, it appears that the temperature dependent data cannot be used to accurately determine the carriers in the $\text{Ge}_{0.90}\text{Si}_{0.08}\text{Sn}_{0.02}$ layer alone. This is most likely due to the very similar levels of doping in the $\text{Ge}_{0.90}\text{Si}_{0.08}\text{Sn}_{0.02}$ layer ($1 \times 10^{18} \text{ cm}^{-3}$) and the $p\text{-Ge}$ substrate ($6 \times 10^{17} \text{ cm}^{-3}$).

The measured room temperature carrier concentration is plotted in Figure 44 as a function of etch depth for both air and vacuum. Here the 2nd and 3rd etches with layer thicknesses of 85 nm and 105 nm, respectively, were averaged and treated as one etch with a thickness of 138 nm in order to obtain a better fit. Subsequently, the 4th etch was treated as an etch with a thickness of 171 nm. With this adjustment included, a clear decrease in the p -type carrier concentration as a function of etch depth can be seen. This was not necessarily the case with the temperature dependent data. As with the $\text{Ge}_{1-y}\text{Sn}_y$ samples, the carrier concentration measured in air is systematically higher than that measured in vacuum. The linear fit yielded a slope of $4.8 \times 10^{11} \text{ cm}^{-2}/\text{nm}$ which corresponds to a volume carrier density of $4.8 \times 10^{18} \text{ cm}^{-3}$. This is somewhat higher than the boron concentration of $1.0 \times 10^{18} \text{ cm}^{-3}$ measured using SIMS, but is still the correct order of magnitude. This could be due in part to the effect of the $p\text{-Ge}$ substrate. Overall, this is an encouraging result, especially in light of the simplicity of the linear fits.

The surface state density given by the offset between the two lines was $5 \times 10^{13} \text{ cm}^{-2}$, which is more than 2 orders of magnitude lower than the measured values. This is very different from both the Ge/Si and the $\text{Ge}_{1-y}\text{Sn}_y/\text{Si}$ samples where the surface states were about one order of magnitude less than the measured values. It

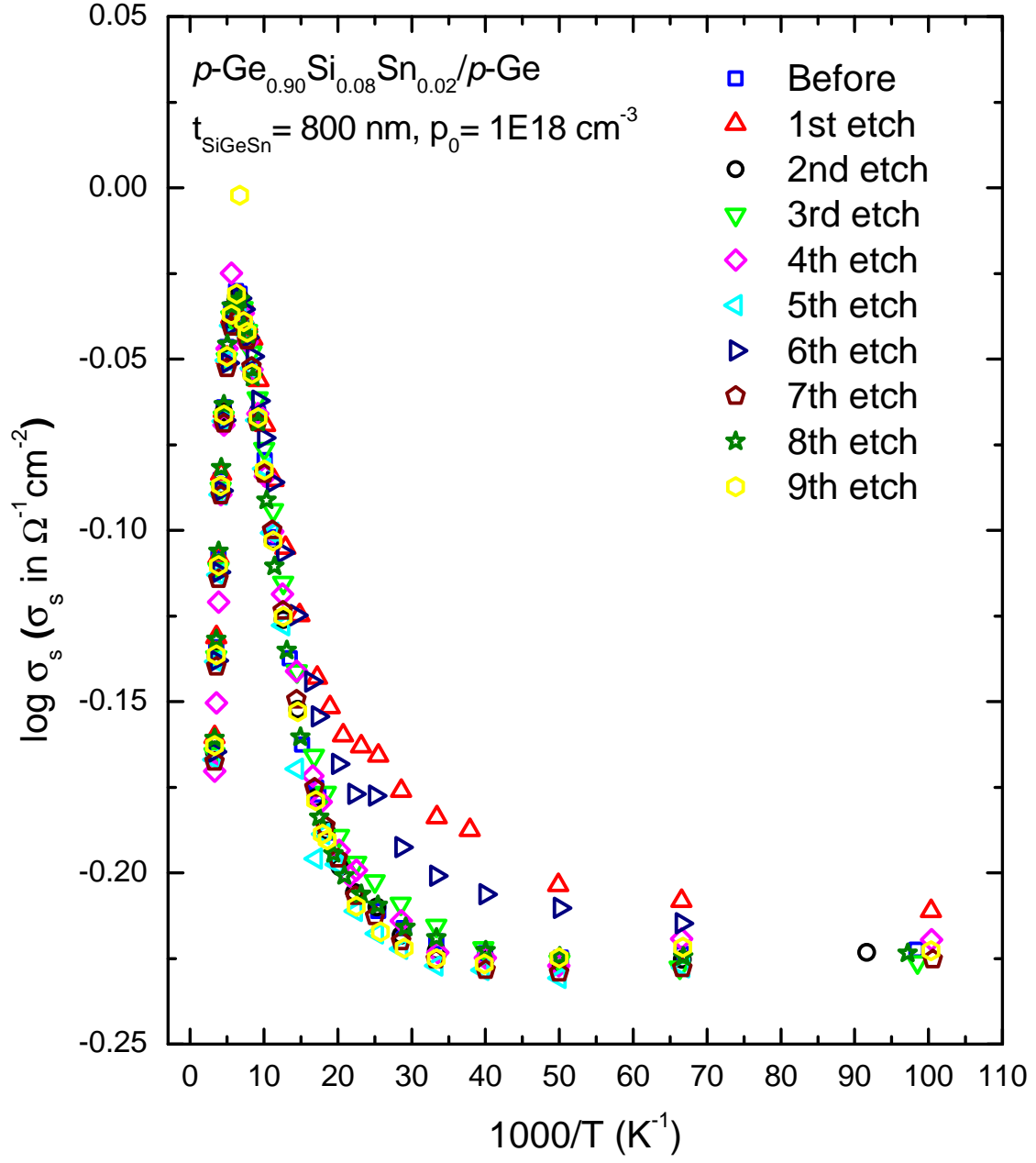


Figure 43. Log conductivity plotted as a function of inverse temperature for the $p\text{-Ge}_{0.90}\text{Si}_{0.08}\text{Sn}_{0.02}/p\text{-Ge}$ sample for all etches.

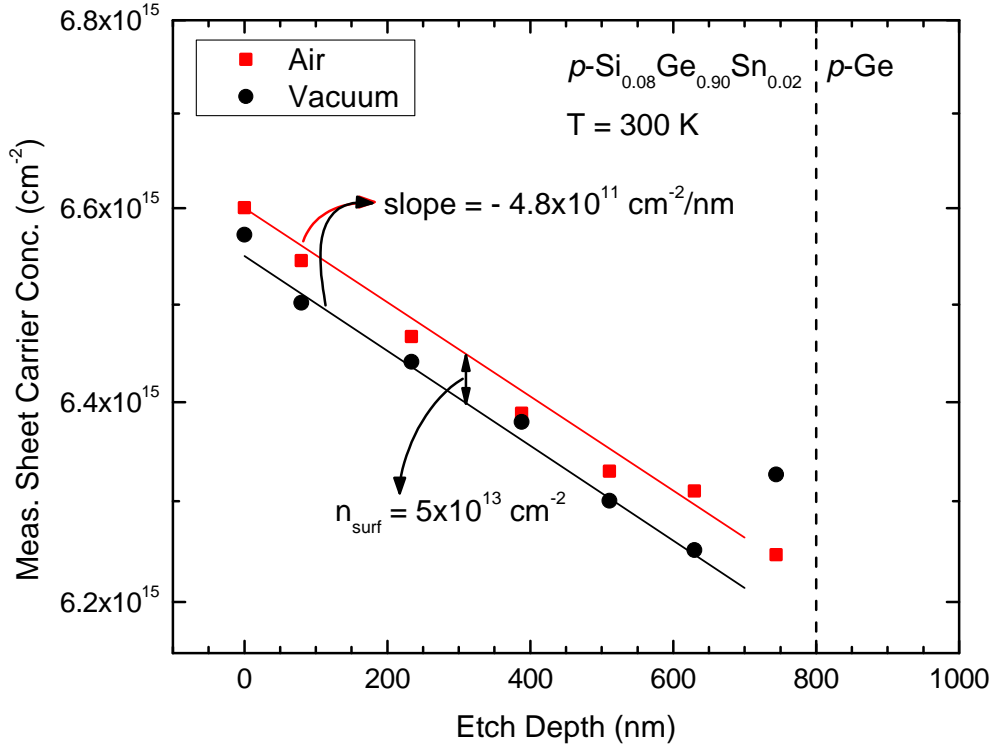


Figure 44. Room temperature sheet carrier concentration plotted as a function of etch depth for the $p\text{-Ge}_{0.90}\text{Si}_{0.08}\text{Sn}_{0.02}/p\text{-Ge}$ sample.

could be that the high doping level and/or the presence of Si in the ternary alloy reduces the surface state density. Also, the low temperature carrier densities of the Ge/Si and the $\text{Ge}_{1-y}\text{Sn}_y/\text{Si}$ samples were generally about an order of magnitude lower than the room temperature carrier densities. Because of that, the effect of the surface states on the low temperature carriers was significant. For this $\text{Ge}_{0.90}\text{Si}_{0.08}\text{Sn}_{0.02}$ sample, however, the low temperature carriers are actually somewhat higher than the room temperature carriers. So the surface state density is much smaller than the measured carrier density even at low temperatures, and therefore the effect of the surface states is negligible.

The differential Hall equations (Eqns. 18-22) were applied to the RT data for this sample and the results are shown in Figure 45. As with the previous samples, there is a large variation in the data. The average value was $6.32 \times 10^{17} \text{ cm}^{-3}$ which is much lower than the value of $4.8 \times 10^{18} \text{ cm}^{-3}$ obtained from the linear fits and somewhat lower than the boron concentration of $1.0 \times 10^{18} \text{ cm}^{-3}$ measured using SIMS. Measured carrier profiles are plotted as a function of etch depth for selected temperatures in Figure 46. The differential Hall equations were applied to each profile separately and the resulting calculated volume carrier concentration is plotted as a function of etch depth in Figure 47. Unfortunately there is not a clear decrease in the measured profiles as was the case with previous samples. There is also no sharp increase near the interface which would indicate a degenerate interfacial conducting layer.

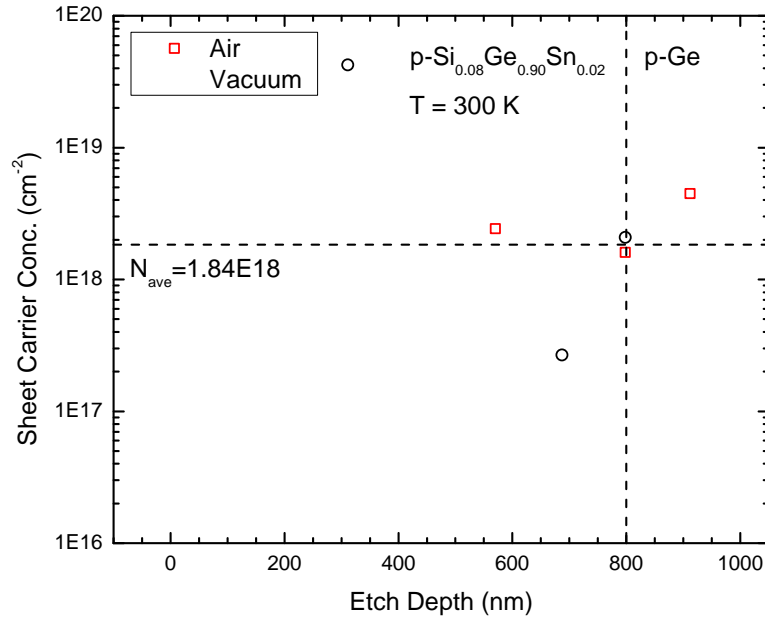


Figure 45. Volume carrier concentration of each removed layer plotted as a function of etch depth for the $p\text{-Ge}_{0.90}\text{Si}_{0.08}\text{Sn}_{0.02}/p\text{-Ge}$ sample calculated using the differential Hall model in Eqns. (18)-(22).

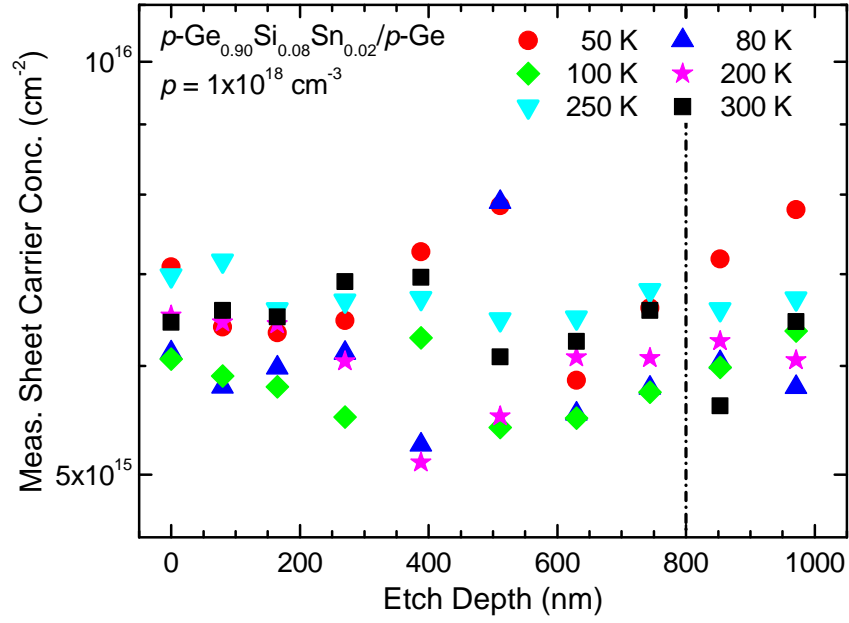


Figure 46. Measured sheet carrier profiles plotted as a function of etch depth at different temperatures for the $p\text{-Ge}_{0.90}\text{Si}_{0.08}\text{Sn}_{0.02}/p\text{-Ge}$ sample.

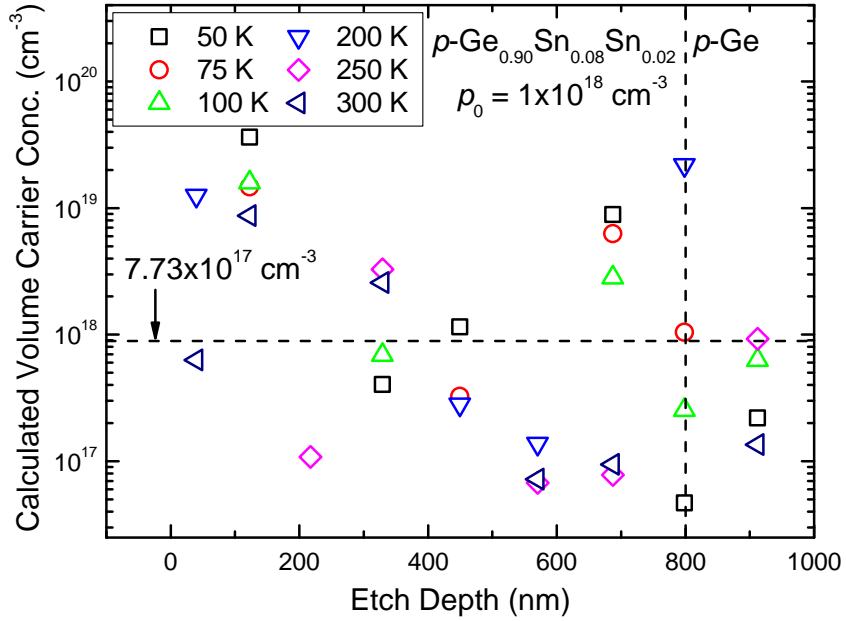


Figure 47. Calculated volume carrier profiles plotted as a function of etch depth at different temperatures for the $p\text{-Ge}_{0.90}\text{Si}_{0.08}\text{Sn}_{0.02}/p\text{-Ge}$ sample.

V. Conclusions

Optical and electrical properties of $\text{Ge}_{1-y}\text{Sn}_y$ and $\text{Ge}_{1-x-y}\text{Si}_x\text{Sn}_y$ grown on Si and Ge substrates have been characterized as a function of sample composition and temperature. Several important results were obtained including a larger than expected reduction in the direct bandgap due to the addition of Sn and strain as well as a reduced Γ -L separation from T-dependent PL measurements. Novel results found for the electrical properties include degenerate parallel conducting layers near the film-substrate interface, conductivity type conversions above room temperature, and the presence of surface states through T-dependent Hall-effect measurements.

Specifically, the T-dependent PL of 0.19% tensile-strained $p\text{-Ge}/p\text{-Si}$, 0.22% tensile-strained phosphorus doped $n\text{-Ge}_{0.997}\text{Sn}_{0.003}/n\text{-Si}$, and 0.16 % tensile-strained $p\text{-Ge}_{0.99}\text{Sn}_{0.01}/n\text{-Si}$ samples was investigated. These samples show both direct (E_D) and indirect bandgap related (E_{ID}) optical transitions, but show very different T-dependent PL spectra. The $p\text{-Ge}/p\text{-Si}$ film shows a strong E_D transition at RT, and much stronger, dominant E_D and weak E_{ID} PL emissions at LT. On the other hand, for the $n\text{-Ge}_{0.997}\text{Sn}_{0.003}/n\text{-Si}$, strong, dominant E_{ID} emission was observed at LT, but weak E_D transition was observed at RT. Finally, for the $p\text{-Ge}_{0.99}\text{Sn}_{0.01}/n\text{-Si}$ sample, very weak E_{ID} emission was observed at LT, and relatively strong E_D transition was observed at RT. The T-dependent PL results also clearly show competitiveness between the E_D and E_{ID} PL transitions as T changes. The T-dependent PL results for the $p\text{-Ge}/p\text{-Si}$ sample show that the estimated reduced energy separation between the L and Γ valleys, $[E_\Gamma(0) - E_L(0)]$, at 0 K is about 116 meV compared to the theoretically predicted value of 132 meV. On the other hand, for $n\text{-Ge}_{0.997}\text{Sn}_{0.003}/\text{Si}$ sample, the estimated $[E_\Gamma(0) - E_L(0)]$ is about 56 meV compared to the predicted value of 122 meV, and $[E_\Gamma(300) - E_L(300)]$ is about 59 meV compared to the predicted value of 115 meV. Therefore, our T-dependent PL

results strongly indicate that the Sn content and strain reduce the bandgap of $\text{Ge}_{1-y}\text{Sn}_y/\text{Si}$ much more effectively than the theory predicted, and the indirect-to-direct bandgap conversion of $\text{Ge}_{1-y}\text{Sn}_y/\text{Si}$ sample could take place at much lower Sn content than originally anticipated. This observation clearly showed that strong direct bandgap optical transitions at RT could be obtained from $\text{Ge}_{1-y}\text{Sn}_y$ alloys with proper tensile strain and n -type doping concentration, making these $\text{Ge}_{1-y}\text{Sn}_y$ alloys attractive candidates for the fabrication of direct bandgap Ge- and Si-based light emitting devices.

The electrical properties of p -Ge, p - $\text{Ge}_{1-y}\text{Sn}_y$ ($y = 0.06 < 0.1\%$), and p - $\text{Si}_{0.09}\text{Ge}_{0.882}\text{Sn}_{0.028}$ samples grown on n -Si substrates as well as p - $\text{Ge}_{0.90}\text{Si}_{0.08}\text{Sn}_{0.02}$ samples grown on p -Ge substrates have been investigated as a function of temperature. Evidence for a parallel degenerate conducting layer near the interface of Ge, $\text{Ge}_{1-y}\text{Sn}_y$ or $\text{Ge}_{0.882}\text{Si}_{0.09}\text{Sn}_{0.028}$ and Si substrate has been found. This layer is believed to be associated with dislocation defects at the interfaces caused by the lattice mismatch between the epilayer and the substrate. Near the interfaces, the sheet carrier concentrations ranged from 1.6×10^{11} to $3.6 \times 10^{12} \text{ cm}^{-2}$ depending on the sample. The temperature-dependent Hall-effect measurements also showed a conductivity type change from p - to n -type at around 370-435 K for these samples. The mobilities of these epilayers are generally lower than the mobility of bulk Ge due to carrier scattering near the interface between the epitaxial layer and the Si substrate and also due to alloy scattering. In addition to the shallow boron acceptor, an unknown deep acceptor was also observed in these materials. Detailed behavior of temperature-dependent conductivity of these samples is also discussed. It was also shown that the observed degenerate conducting layer significantly affects the electrical properties of all these epitaxial layers, and thus it may also significantly affect the operation of electronic and optoelectronic devices above room

temperature. Etching studies were performed to investigate the source of the degenerate conducting layer and to determine the electrical properties of the epilayers themselves. The resulting calculated values for the volume carrier density were reasonable although there were considerable fluctuations in the data. In addition, a significant contribution from n -type surface states were observed for almost all samples which resulted in actual p -type carrier densities greater than what was measured. It is strongly believed that the information obtained in these studies will be useful for subsequent growth of $\text{Ge}_{1-y}\text{Sn}_y$ and $\text{Ge}_{1-x-y}\text{Si}_x\text{Sn}_y$ semiconductor alloys and for the development of future novel electronic and optoelectronic devices made from materials.

VI. Recommendations for Future Work

The following are recommendations for future study of these $\text{Ge}_{1-y}\text{Sn}_y$ and $\text{Ge}_{1-x-y}\text{Si}_x\text{Sn}_y$ materials. The first is an extensive temperature- and laser power-dependent PL study of a 0.19% tensile-strained $i\text{-Ge}_{1-y}\text{Sn}_y/n\text{-Si}$ (0.03% Sn) sample, which is already underway. This investigation may provide direct observation of the $\Gamma\text{-hh}$ and $\Gamma\text{-lh}$ transitions. Secondly, the competitiveness between not only the direct and indirect transitions, but also the $\Gamma\text{-lh}$ and $\Gamma\text{-hh}$ transitions themselves, can be analyzed using the measured PL data as a function of temperature and laser power. Another possible study would involve additional laser power-dependent as well as wavelength-dependent PL of Ge/Si and $\text{Ge}_{1-y}\text{Sn}_y/\text{Si}$ samples. Various IR as well as visible wavelengths would be investigated using the Ti-sapphire and Ar-ion lasers, respectively. If high-quality $\text{Ge}_{1-y}\text{Sn}_y$ samples with higher Sn-contents were obtained, temperature dependent and power dependent PL could be performed. This would allow for a more accurate analysis of the band gap bowing of the direct and indirect transitions. Lastly, if high-quality $\text{Ge}_{1-x-y}\text{Si}_x\text{Sn}_y$ samples were obtained, they could be characterized and potentially yield valuable information. There have only been a few reports of PL from $\text{Ge}_{1-x-y}\text{Si}_x\text{Sn}_y$ materials in the literature and so any good PL data obtained would most likely be publishable. Further, the electrical properties of these ternary alloys are not well known at all at present. Most of the samples previously studied were grown lattice-matched on doped Ge substrates, which made determining the electrical properties of the $\text{Ge}_{1-x-y}\text{Si}_x\text{Sn}_y$ layers alone very difficult. If possible, samples grown on non-conductive or different conductivity type substrates like high-resistivity Si or semi-insulating GaAs should be obtained for electrical measurements. Hall-effect measurements and etching studies could yield very valuable information about the transport of carriers in these materials which is in high demand.

Appendix A. Magnetic Field Correction

Let B_S be the magnetic field at the sample and B_P be the magnetic field at the pole. The actual Hall Coefficient is given by

$$\begin{aligned}
 R_H^{real} &= \frac{\Delta R_{13,24}^{real}}{B_S} \\
 \Delta R_H^{real} &= \frac{\Delta R_{13,24}^{real}}{B_S} \times \frac{B_P}{B_P} = \left(\frac{B_P}{B_S} \right) \frac{\Delta R_{13,24}^{real}}{B_P} \\
 &= \left(\frac{B_P}{B_S} \right) R_H^{cc}
 \end{aligned} \tag{A.1}$$

where $R_{13,24}^{real} = [R_{13,24}]_{B=0} - [R_{13,24}]_{B=B_S}$ and ‘cc’ stands for computer calculated.

Similarly, we can write the actual carrier concentration as

$$\begin{aligned}
 n_s^{real} &= \frac{r}{e R_H^{real}} \\
 &= \frac{r}{e \left(\frac{B_P}{B_S} \right) R_H^{cc}} = \left(\frac{B_S}{B_P} \right) \frac{r}{e R_H^{cc}} \\
 &= \left(\frac{B_S}{B_P} \right) n_s^{cc}
 \end{aligned} \tag{A.2}$$

Finally, we have the real carrier mobility which can be written as

$$\begin{aligned}
 \mu^{real} &= \frac{R_H^{real}}{\rho_0} \\
 &= \left(\frac{B_P}{B_S} \right) \frac{R_H^{real}}{\rho_0} \\
 &= \left(\frac{B_P}{B_S} \right) \mu^{cc}
 \end{aligned} \tag{A.3}$$

This gives the scale factors which can be used to correct the data output by the LakeShore Hall Measurement System in order to obtain the real values for the sample.

Appendix B. Band Structure Calculations

The compositional dependence of the band gaps of these $\text{Ge}_{1-y}\text{Sn}_y$ alloys were calculated as a function of temperature using an equation of the form:

$$E_{i,\text{GeSn}}(y, T) = yE_{i,\text{Sn}} + (1 - y)E_{i,\text{Ge}}(T) - y(1 - y)b_i(T) \quad (\text{B.1})$$

where $i = \Gamma, L$ for the direct and indirect gaps, $E_{i,\text{Sn}}$ and $E_{i,\text{Ge}}$ are the band gaps of elemental Sn and Ge, b_i is the bowing parameter, y is the Sn composition, and T is temperature. The parameters used in these equations are listed in Table 10 at both low temperature (LT) and room temperature (RT). Note that the band gaps of α -Sn are assumed to be temperature independent. This is because the only measurements of the band gaps found in the literature were taken at 4 K. The temperature dependence of the Ge band gaps are given by the following Varshni equations:

$$E_{\Gamma,\text{Ge}}(T) = 0.890 - 5.82 \times 10^{-4} \frac{T^2}{T + 296} \quad (\text{B.2})$$

$$E_{L,\text{Ge}}(T) = 0.742 - 4.80 \times 10^{-4} \frac{T^2}{T + 235} \quad (\text{B.3})$$

To better visualize the band gap bowing, a plot of the calculated GeSn band gaps vs Sn composition at LT and RT is shown in Figures 48a and 48b, respectively.

Table 10. Parameters used for the compositional dependence of the band gap in $\text{Ge}_{1-y}\text{Sn}_y$ alloys. All values are given in eV.

T(K)	$E_{\Gamma,\text{Ge}}$	$E_{L,\text{Ge}}$	$E_{\Gamma,\text{Sn}}$	$E_{L,\text{Sn}}$	b_{Γ}	b_L
0	0.890	0.742	-0.410	0.140	2.55	0.89
300	0.802	0.661	-0.410	0.140	1.95	0.68

The effect of tensile strain was calculated using deformation potential theory which yields the following equations for the split heavy hole (hh) and light hole (lh)

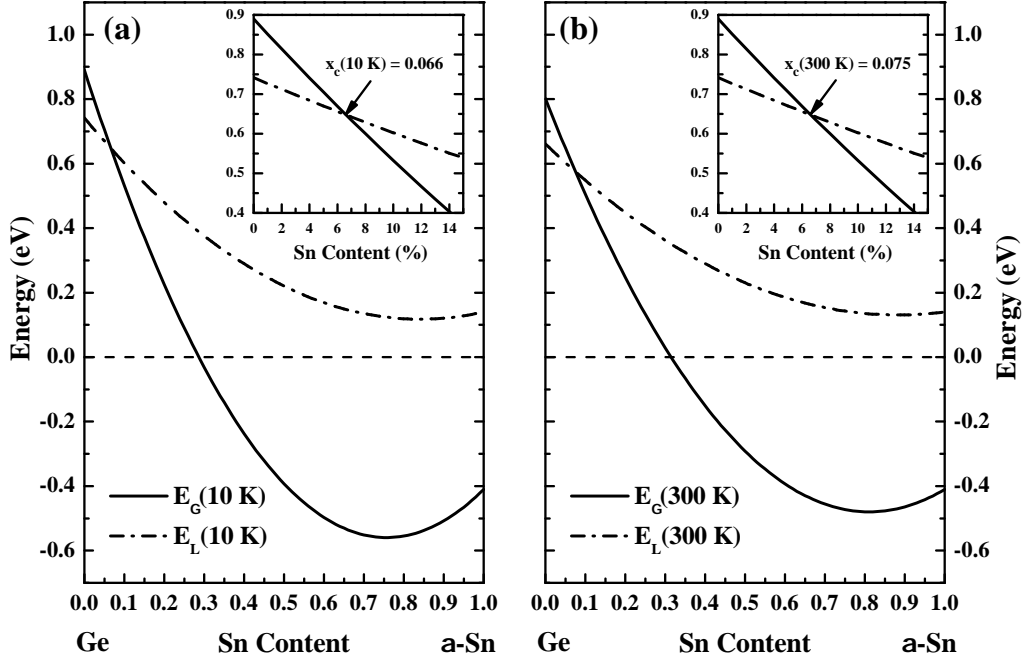


Figure 48. Calculated compositional dependence of the unstrained $\text{Ge}_{1-y}\text{Sn}_y$ band gaps (a) at 10 K and (b) at 300 K.

transition energies:

$$E_{hh}^i = E_0^i - \delta E_{\text{hy}}^i + \frac{1}{2} \delta E_{\text{sh}} \quad (\text{B.4})$$

$$E_{lh}^i = E_0^i + \frac{\Delta_0}{2} - \delta E_{\text{hy}}^i - \frac{1}{4} \delta E_{\text{sh}} - \frac{1}{2} \sqrt{\frac{9}{4} (\delta E_{\text{sh}})^2 + \Delta_0 \cdot \delta E_{\text{sh}} + \Delta_0^2} \quad (\text{B.5})$$

where again $i = \Gamma, \text{L}$ for the direct and indirect gaps, E_0^i is the unstrained band gap, δE_{hy}^i and δE_{sh} are the hydrostatic and shear deformation energies, and Δ_0 is the spin-orbital splitting energy. Here δE_{hy}^i and δE_{sh} can be written in terms of the

in-plane strain $\varepsilon_{||}$ as

$$\delta E_{\text{hy}}^i = -2a_i(1 - C_{12}/C_{11})\varepsilon_{||}, \text{ and} \quad (\text{B.6})$$

$$\delta E_{\text{sh}} = -2b(1 + 2C_{12}/C_{11})\varepsilon_{||} \quad (\text{B.7})$$

where a_i and b are the hydrostatic and shear deformation potential constants. For $\varepsilon_{||} < 0$ the strain is compressive and for $\varepsilon_{||} > 0$ the strain is tensile. A summary of the parameters used in the strain calculation is given in Table 11. The hh-lh splitting is shown in Figure 49 where the direct band gaps are plotted as a function of in-plane strain.

Table 11. Parameters used for the strain dependence of the band gap in $\text{Ge}_{1-y}\text{Sn}_y$ alloys.

a_{Γ} (eV)	a_L (eV)	b (eV)	Δ_0 (eV)	C_{12}/C_{11}
-9.48	-2.78	-2.55	0.297	0.3758

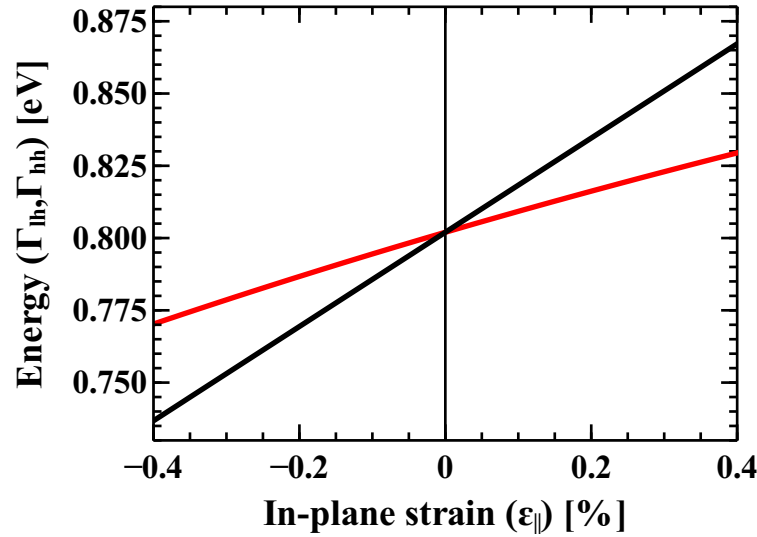


Figure 49. Strain dependence of the Γ -hh (red) and Γ -lh (black) band gaps of $\text{Ge}_{1-y}\text{Sn}_y$

Appendix C. Temperature Dependent Strain Calculation

The in-plane biaxial strain in these films can be written as a function of temperature as $\varepsilon_{||}(T) = (a_{\text{Ge}}(T) - a_{\text{Si}}(T))/a_{\text{Ge}}(T)$ where a_{Si} is the equilibrium lattice constant of Si and a_{Ge} is the effective lattice constant of the Ge epilayer. Using the measured value for the room temperature strain we can solve for the effective lattice constant of the Ge layer giving

$$a_{\text{Ge}}(300) = \frac{1}{1 - \varepsilon_{||}(300)} a_{\text{Si}}(300) \quad (\text{C.1})$$

In order to determine the lattice constants at low temperatures, the thermal expansivities of Si and Ge were first calculated using a mixed Einstein-Debye model given by the following equation [56]:

$$\begin{aligned} \alpha_i(T) = \frac{4k_B}{[a_i(300)]^3 B_{0i}} & \left[\frac{2}{3} \gamma_{\text{TA},i} \left(\frac{\theta_{\text{TA},i}}{T} \right)^2 \frac{e^{\theta_{\text{TA},i}/T}}{(e^{\theta_{\text{TA},i}/T} - 1)^2} \right. \\ & + \gamma_{\text{TA},i} \left(\frac{T}{\theta_{\text{TA},i}} \right)^3 I_{\text{LA}}(x_{D,i}) \\ & \left. + \gamma_{\text{opt},i} \left(\frac{\theta_{\text{opt},i}}{T} \right)^2 \frac{e^{\theta_{\text{opt},i}/T}}{(e^{\theta_{\text{opt},i}/T} - 1)^2} \right], \end{aligned} \quad (\text{C.2})$$

where
$$I_{\text{LA}}(x_{\text{LA},i}) = 24 \sum_{m=0}^N \left(1 - e^{-x_{\text{LA},i}(m+1)} \left(\sum_{k=0}^4 \frac{(x_{\text{LA},i}(m+1))^k}{k!} \right) \right) / (m+1)^4$$

and
$$x_{\text{LA},i} = \theta_{\text{LA},i}/T$$

and where $i = \text{Si, Ge}$. Here $k_B = 1.38 \times 10^{-23}$ J/K is Boltzmann's constant, B_0 is the bulk modulus, $a(300)$ is the RT lattice constant, γ_{TA} , γ_{LA} , γ_{opt} are the Grüneisen parameters and θ_{TA} , θ_{LA} , θ_{opt} are the phonon temperatures for the transverse-acoustic (TA), longitudinal-acoustic (LA), and optic (opt) modes. Values for all of the parameters used in this model are given in Table 12.

Table 12. Parameters used for the temperature dependence of the thermal expansivities of Si and Ge.[56]

	γ_{TA}	θ_{TA} (K)	γ_{LA}	θ_{LA} (K)	γ_{opt}	θ_{opt} (K)	θ_D (K)	B_0 (GPa)
Si	-0.55	217	1.21	734	1.21	673	645	97.9
Ge	-0.09	117	1.29	411	1.29	388	347	75.8

Recalling the definition of the coefficient of linear thermal expansion, we can write it in terms of the lattice constant as

$$\alpha_i = \frac{1}{a_i} \frac{da_i}{dT} \quad (C.3)$$

where again $i = \text{Si, Ge}$. Rearranging, we have

$$\frac{da_i}{a_i} = \alpha_i dT \quad (C.4)$$

We can now integrate from RT to low temperature

$$\int_{a_i(300)}^{a_i(T_f)} \frac{da_i}{a_i} = \int_{300}^{T_f} \alpha_i(T) dT \quad (C.5)$$

where T_f could range from 5-20 K depending on the sample. Performing the integral on the left hand side, we obtain

$$\ln(a_i(T_f)) - \ln(a_i(300)) = \int_{300}^{T_f} \alpha_i(T) dT \quad (C.6)$$

Using the logarithm property $\ln(b) - \ln(a) = \ln(b/a)$, we can rewrite the equation as

$$\ln\left(\frac{a_i(T_f)}{a_i(300)}\right) = \int_{300}^{T_f} \alpha_i(T) dT \quad (C.7)$$

Finally, taking the exponential of both sides and multiplying through by $a_i(300)$, we

have expressions for the lattice constants of the epilayer and substrate at LT:

$$a_i(T_f) = e^{\int_{300}^{T_f} \alpha_i(T) dT} a_i(300) \quad (\text{C.8})$$

where $a_{\text{Si}}(300) = 5.431 \text{ \AA}$, and $a_{\text{Ge}}(300)$ is given by Eqn. (C.1). Finally, we can find LT strain from the LT lattice constants using the following equation:

$$\varepsilon_{||}(LT) = \frac{a_{\text{Si}}(LT) - a_{\text{Ge}}(LT)}{a_{\text{Ge}}(LT)} \quad (\text{C.9})$$

A summary of the 300 K and 10 K strain values for the three PL samples studied is given in Table 13.

Table 13. Comparison of room temperature and low temperature strain values for selected Ge and $\text{Ge}_{1-y}\text{Sn}_y$ samples. Negative values represent tensile strain.

Sample Name/ Composition	$\varepsilon_{ }(300 \text{ K})$ [%]	$\varepsilon_{ }(10 \text{ K})$ [%]
Ge/ <i>p</i> -Si	-0.19	-0.27
<i>n</i> -Ge _{0.997} Sn _{0.003} / <i>n</i> -Si	-0.22	-0.30
<i>p</i> -Ge _{0.99} Sn _{0.01} / <i>n</i> -Si	-0.16	-0.23

Appendix D. Publications and Presentations

M.-Y. Ryu, T. R. Harris, Y. K. Yeo, R. T. Beeler, and J. Kouvetakis,
"Temperature-dependent photoluminescence of Ge/Si and $\text{Ge}_{1-y}\text{Sn}_y/\text{Si}$, indicating possible indirect-to-direct bandgap transition at lower Sn content," *Appl. Phys. Lett.* **102** (17), 171908 (2013)

T. R. Harris, M.-Y. Ryu, Y. K. Yeo, R. T. Beeler, and J. Kouvetakis, "Electrical characterization studies of p -type Ge, $\text{Ge}_{1-y}\text{Sn}_y$, and $\text{Ge}_{0.882}\text{Si}_{0.090}\text{Sn}_{0.028}$ grown on n -Si substrates," *Curr. Appl. Phys., In Press Corrected Proof* (2013)

M.-Y. Ryu, Y. K. Yeo, M. Ahoujja, T. Harris, R. Beeler, and J. Kouvetakis,
"Degenerate parallel conducting layer and conductivity type conversion observed from p - $\text{Ge}_{1-y}\text{Sn}_y$ ($y=0.06\%$) grown on n -Si substrates, *Appl. Phys. Lett.* **101**, 131110 (2012)

T. R. Harris, Y. K. Yeo, M.-Y. Ryu, R. T. Beeler, and J. Kouvetakis, "Electrical Properties of p -Ge and p -GeSn materials grown on n -Si substrates," *APS March Meeting*, Baltimore, MD, March 18-22, 2013

Bibliography

- [1] M. E. Levinshen, S. L. Rumyantsev, and M. Shur, *Handbook Series on Semiconductor Parameters, Volume 1: Si, Ge, C (Diamond), GaAs, GaP, GaSb, InAs, InP, InSb*, World Scientific (1996).
- [2] J. Liu, X. Sun, D. Pan, X. Wang, L. C. Kimerling, T. L. Koch, and J. Michel, “Tensile-strained, n-type Ge as a gain medium for monolithic laser integration on Si”, *Optics Express* **15** (18), 11272–11277 (2007).
- [3] C. G. Van de Walle, “Band lineups and deformation potentials in the model-solid theory”, *Physical Review B* **39** (3), 1871–1883 (1989).
- [4] X. Sun, J. Liu, L. C. Kimerling, and J. Michel, “Direct gap photoluminescence of n-type tensile-strained Ge-on-Si”, *Applied Physics Letters* **95**, 011911 (2009).
- [5] G. A. Slack and S. F. Bartram, “Thermal expansion of some diamondlike crystals”, *Journal of Applied Physics* **46** (1), 89–98 (1975).
- [6] H. Luan, D. R. Lim, K. K. Lee, K. M. Chen, J. G. Sandland, K. Wada, and L. C. Kimerling, “High-quality Ge epilayers on Si with low threading-dislocation densities”, *Applied Physics Letters* **75** (19), 2909–2911 (1999).
- [7] J. Liu, X. Sun, R. Camacho-Aguilera, L. C. Kimerling, and J. Michel, “Ge-on-Si laser operating at room temperature”, *Optics Letters* **35** (5), 679–681 (2010).
- [8] G. Grzybowski, L. Jiang, J. Mathews, R. Roucka, C. Xu, R. T. Beeler, J. Kouvetakis, and J. Menendez, “Photoluminescence from heavily doped GeSn:P materials grown on Si(100)”, *Applied Physics Letters* **99**, 171910 (2011).
- [9] J. Mathews, R. T. Beeler, J. Tolle, C. Xu, R. Roucka, J. Kouvetakis, and J. Menendez, “Direct-gap photoluminescence with tunable emission wavelength in $\text{Ge}_{1-y}\text{Sn}_y$ alloys on silicon”, *Applied Physics Letters* **97**, 221912 (2010).
- [10] D. W. Jenkins and J. D. Dow, “Electronic properties of metastable $\text{Ge}_x\text{Sn}_{1-x}$ alloys”, *Physical Review B* **36** (15), 7994–8000 (1987).
- [11] G. He and H. A. Atwater, “Interband transitions in $\text{Sn}_x\text{Ge}_{1-x}$ alloys”, *Physical Review Letters* **79** (10), 1937–1940 (1997).
- [12] R. Chen, H. Lin, Y. Huo, C. Hitzman, T. I. Kamins, and J. S. Harris, “Increased photoluminescence of strain-reduced, high-Sn composition $\text{Ge}_{1-x}\text{Sn}_x$ alloys grown by molecular beam epitaxy”, *Applied Physics Letters* **99**, 181125 (2011).

- [13] V. R. DCosta, C. S. Cook, A. G. Birdwell, C. L. Littler, M. Canonico, S. Zollner, J. Kouvetakis, and J. Menendez, “Optical critical points of thin-film $\text{Ge}_{1-y}\text{Sn}_y$ alloys: A comparative $\text{Ge}_{1-y}\text{Sn}_y\text{Ge}_{1-x}\text{Si}_x$ study”, *Physical Review B* **73** (12), 125207 (2006).
- [14] M. Bauer, J. Taraci, J. Tolle, A. V. G. Chizmeshya, S. Zollner, D. J. Smith, J. Menendez, C. Hu, and J. Kouvetakis, “GeSn semiconductors for band-gap and lattice engineering”, *Applied Physics Letters* **81**, 2992 (2002).
- [15] M. Bauer, C. Ritter, P. A. Crozier, J. Ren, J. Menendez, G. Wolf, and J. Kouvetakis, “Synthesis of ternary SiGeSn semiconductors on Si(100) via $\text{Sn}_x\text{Ge}_{1-x}$ buffer layers”, *Applied Physics Letters* **83**, 2163 (2003).
- [16] J. Kouvetakis and A. V. G. Chizmeshya, “New classes of Si-based photonic materials and device architectures via designer molecular routes”, *J. Mater. Chem.* **17** (17), 1649–1655 (2007).
- [17] J. Xie, J. Tolle, V. R. DCosta, A. V. G. Chizmeshya, J. Menendez, and J. Kouvetakis, “Direct integration of active $\text{Ge}_{1-x}\text{Si}_4\text{Sn}_x$ semiconductors on Si(100)”, *Applied Physics Letters* **95**, 181909 (2009).
- [18] J. Tolle, R. Roucka, A. V. G. Chizmeshya, J. Kouvetakis, V. R. DCosta, and J. Menendez, “Compliant tin-based buffers for the growth of defect-free strained heterostructures on silicon”, *Applied Physics Letters* **88**, 252112 (2006).
- [19] G. Grzybowski, R. Roucka, J. Mathews, L. Jiang, R. T. Beeler, J. Kouvetakis, and J. Menéndez, “Direct versus indirect optical recombination in Ge films grown on Si substrates”, *Phys. Rev. B* **84**, 205307 (2011).
- [20] K. Mder, A. Baldereschi, and H. von Knel, “Band structure and instability of $\text{Ge}_{1-x}\text{Sn}_x$ alloys”, *Solid State Communications* **69** (12), 1123–1126 (1989).
- [21] N. Amrane, S. Ait Abderrahmane, and H. Aourag, “Band structure calculation of GeSn and SiSn”, *Infrared Physics & Technology* **36** (5), 843–848 (1995).
- [22] W. Yin, X. Gong, and S. Wei, “Origin of the unusually large band-gap bowing and the breakdown of the band-edge distribution rule in the $\text{Sn}_x\text{Ge}_{1-x}$ alloys”, *Physical Review B* **78** (16), 161203 (2008).
- [23] C. D. Thurmond, F. A. Trumbore, and M. Kowalchik, “Germanium solidus curves”, *Journal of Chemical Physics* **25** (4), 799 (1956).
- [24] O. Gurdal and M. Hasan, “Growth of metastable $\text{Ge}_{1-x}\text{Sn}_x/\text{Ge}$ strained layer superlattices on Ge(001) 2×1 by temperature-modulated molecular beam epitaxy”, *Applied Physics Letters* **67** (7), 956 (1995).

- [25] S. Shah, J. Greene, L. Abels, Q. Yao, and P. Raccach, “Growth of single-crystal metastable $\text{Ge}_{1-x}\text{Sn}_x$ alloys on Ge(100) and GaAs(100) substrates”, *Journal of Crystal Growth* **83** (1), 3–10 (1987).
- [26] S. Oguz, W. Paul, T. F. Deutsch, B. Tsaur, and D. V. Murphy, “Synthesis of metastable, semiconducting GeSn alloys by pulsed UV laser crystallization”, *Applied Physics Letters* **43** (9), 848–850 (1983).
- [27] O. Gurdal, P. Desjardins, J. R. A. Carlsson, N. Taylor, H. H. Radamson, J. Sundgren, and J. E. Greene, “Low temperature growth and critical epitaxial thickness of fully strained metastable $\text{Ge}_{1-x}\text{Sn}_x$ ”, *Journal of Applied Physics* **83** (1), 162 (1998).
- [28] G. He and H. A. Atwater, “Synthesis of epitaxial $\text{Sn}_x\text{Ge}_{1-x}$ alloy films by ion assisted molecular beam epitaxy”, *Applied Physics Letters* **68** (5), 664–666 (1996).
- [29] G. Grzybowski, R. T. Beeler, L. Jiang, D. J. Smith, J. Kouvetakis, and J. Menendez, “Next generation of $\text{Ge}_{1-y}\text{Sn}_y$ ($y=0.01-0.09$) alloys grown on Si(100) via Ge_3H_8 and SnD_4 : Reaction kinetics and tunable emission”, *Applied Physics Letters* **101** (7), 072105–072105–5 (2012).
- [30] Y. Chibane and M. Ferhat, “Electronic structure of $\text{Sn}_x\text{Ge}_{1-x}$ alloys for small Sn compositions: Unusual structural and electronic properties”, *Journal of Applied Physics* **107**, 053512 (2010).
- [31] M.-Y. Ryu, T. R. Harris, Y. K. Yeo, R. T. Beeler, and J. Kouvetakis, “Temperature-dependent photoluminescence of Ge/Si and $\text{Ge}_{1-y}\text{Sn}_y/\text{Si}$, indicating possible indirect-to-direct bandgap transition at lower Sn content”, *Applied Physics Letters* **102** (17), 171908 (2013).
- [32] J. Haynes, M. Lax, and W. Flood, “Analysis of intrinsic recombination radiation from silicon and germanium”, *Journal of Physics and Chemistry of Solids* **8**, 392–396 (1959).
- [33] J. Wagner and L. Via, “Radiative recombination in heavily doped p-type germanium”, *Physical Review B* **30** (12), 7030–7036 (1984).
- [34] Y. Varshni, “Temperature dependence of the energy gap in semiconductors”, *Physica* **34** (1), 149 – 154 (1967).
- [35] J. R. Chelikowsky and M. L. Cohen, “Nonlocal pseudopotential calculations for the electronic structure of eleven diamond and zinc-blende semiconductors”, *Physical Review B* **14** (2), 556–582 (1976).
- [36] H. P. Ladrón de Guevara, A. G. Rodríguez, H. Navarro-Contreras, and M. A. Vidal, “ $\text{Ge}_{1-x}\text{Sn}_x$ alloys pseudomorphically grown on Ge(001)”, *Applied Physics Letters* **83** (24), 4942–4944 (2003).

- [37] C. Liu, T.-H. Cheng, Y.-Y. Chen, S.-R. Jan, C.-Y. Chen, S. Chan, Y.-H. Nien, Y. Yamamoto, and B. Tillack, “Direct and indirect radiative recombination from Ge”, *Thin Solid Films* **520** (8), 3249 – 3254 (2012).
- [38] C. Haas, “Infrared absorption in heavily doped n -type germanium”, *Phys. Rev.* **125**, 1965–1971 (1962).
- [39] S. Jain and D. Roulston, “A simple expression for band gap narrowing (BGN) in heavily doped Si, Ge, GaAs and $\text{Ge}_x\text{Si}_{1-x}$ strained layers”, *Solid-State Electronics* **34** (5), 453 – 465 (1991).
- [40] R. Camacho-Aguilera, Z. Han, Y. Cai, L. C. Kimerling, and J. Michel, “Direct band gap narrowing in highly doped Ge”, *Applied Physics Letters* **102** (15), 152106 (2013).
- [41] J. Liu, D. D. Cannon, K. Wada, Y. Ishikawa, D. T. Danielson, S. Jongthammanurak, J. Michel, and L. C. Kimerling, “Deformation potential constants of biaxially tensile stressed Ge epitaxial films on Si(100)”, *Physical Review B* **70** (15), 155309 (2004).
- [42] T. R. Harris, M.-Y. Ryu, Y. K. Yeo, R. T. Beeler, and J. Kouvetakis, “Electrical characterization studies of p-type Ge, $\text{Ge}_{1-y}\text{Sn}_y$, and $\text{Si}_{0.090}\text{Ge}_{0.882}\text{Sn}_{0.028}$ grown on n-Si substrates”, *Current Applied Physics* (2013), in Press.
- [43] J. R. Soderstrom, M. M. Cumming, J. Y. Yao, and T. G. Andersson, “Molecular beam epitaxy growth and characterization of InSb layers on GaAs substrates”, *Semiconductor Science and Technology* **7** (3), 337 (1992).
- [44] O. Schmidt, A. Geis, P. Kiesel, C. G. V. de Walle, N. M. Johnson, A. Bakin, A. Waag, and G. H. Dhlér, “Analysis of a conducting channel at the native zinc oxide surface”, *Superlattices and Microstructures* **39** (14), 8 – 16 (2006).
- [45] J. E. Alberghini and R. M. Broudy, “Surface conductivity on degenerate germanium”, *Phys. Rev. Lett.* **17**, 863–865 (1966).
- [46] C. Mavroidis, J. J. Harris, M. J. Kappers, C. J. Humphreys, and Z. Bougrioua, “Detailed interpretation of electron transport in n-GaN”, *Journal of Applied Physics* **93** (11), 9095–9103 (2003).
- [47] J. J. Harris, K. J. Lee, I. Harrison, L. B. Flannery, D. Korakakis, T. S. Cheng, C. T. Foxon, Z. Bougrioua, I. Moerman, W. Van der Stricht, E. J. Thrush, B. Hamilton, and K. Ferhah, “Interpretation of the temperature-dependent transport properties of GaN/sapphire films grown by MBE and MOCVD”, *physica status solidi (a)* **176** (1), 363–367 (1999).

- [48] D. C. Look and R. J. Molnar, “Degenerate layer at GaN/sapphire interface: Influence on Hall-effect measurements”, *Applied Physics Letters* **70** (25), 3377–3379 (1997).
- [49] J. W. P. Hsu, D. V. Lang, S. Richter, R. N. Kleiman, A. M. Sergent, and R. J. Molnar, “Nature of the highly conducting interfacial layer in GaN films”, *Applied Physics Letters* **77** (18), 2873–2875 (2000).
- [50] E. H. Putley and W. H. Mitchell, “The electrical conductivity and hall effect of silicon”, *Proceedings of the Physical Society* **72** (2), 193 (1958).
- [51] M. Ahoujja, Y. K. Yeo, R. L. Hengehold, G. S. Pomrenke, D. C. Look, and J. Huffman, “Electrical properties of boron-doped p-SiGeC grown on n-Si substrate”, *Applied Physics Letters* **77** (9), 1327–1329 (2000).
- [52] S. M. Sze, *Physics of Semiconductor Devices*, Wiley-Interscience publication, John Wiley & Sons (1981).
- [53] E. M. Conwell, “Properties of silicon and germanium”, *Proceedings of the IRE* **40** (11), 1327–1337 (1952).
- [54] D. Look, *Electrical Characterization of GaAs Materials and Devices*, Design And Measurement in Electronic Engineering, Wiley (1989).
- [55] D. M. Brown and R. Bray, “Analysis of lattice and ionized impurity scattering in *p*-type germanium”, *Phys. Rev.* **127**, 1593–1602 (1962).
- [56] E. Eser, H. Ko, and B. Mamedov, “Use of the integer and non-integer *n*-dimensional debye functions in computing thermal expansivity, with applications to Si and Ge semiconductors”, *Journal of Physics and Chemistry of Solids* **73** (1), 35 – 38 (2012).

REPORT DOCUMENTATION PAGE

Form Approved
OMB No. 0704-0188

The public reporting burden for this collection of information is estimated to average 1 hour per response, including the time for reviewing instructions, searching existing data sources, gathering and maintaining the data needed, and completing and reviewing the collection of information. Send comments regarding this burden estimate or any other aspect of this collection of information, including suggestions for reducing this burden to Department of Defense, Washington Headquarters Services, Directorate for Information Operations and Reports (0704-0188), 1215 Jefferson Davis Highway, Suite 1204, Arlington, VA 22202-4302. Respondents should be aware that notwithstanding any other provision of law, no person shall be subject to any penalty for failing to comply with a collection of information if it does not display a currently valid OMB control number. **PLEASE DO NOT RETURN YOUR FORM TO THE ABOVE ADDRESS.**

1. REPORT DATE (DD-MM-YYYY) 27-03-2014			2. REPORT TYPE PhD Dissertation		3. DATES COVERED (From — To) 29-03-2010 — 27-03-2014	
4. TITLE AND SUBTITLE A Systematic Study of the Optical and Electrical Properties of $\text{Ge}_{1-y}\text{Sn}_y$ and $\text{Ge}_{1-x-y}\text{Si}_x\text{Sn}_y$ Semiconductor Alloys					5a. CONTRACT NUMBER	
					5b. GRANT NUMBER	
					5c. PROGRAM ELEMENT NUMBER	
6. AUTHOR(S) Thomas R. Harris					5d. PROJECT NUMBER	
					5e. TASK NUMBER	
					5f. WORK UNIT NUMBER	
7. PERFORMING ORGANIZATION NAME(S) AND ADDRESS(ES) Air Force Institute of Technology Graduate School of Engineering and Management (AFIT/EN) 2950 Hobson Way WPAFB OH 45433-7765					8. PERFORMING ORGANIZATION REPORT NUMBER AFIT-ENP-DS-14-M-04	
9. SPONSORING / MONITORING AGENCY NAME(S) AND ADDRESS(ES) Dr. Gernot S. Pomrenke Air Force Office of Scientific Research Directorate of Physics and Electronics 875 North Randolph Street Arlington, Virginia 22203-1768 gernot.pomrenke@afosr.af.mil					10. SPONSOR/MONITOR'S ACRONYM(S) AFOSR/RSE	
					11. SPONSOR/MONITOR'S REPORT NUMBER(S)	
12. DISTRIBUTION / AVAILABILITY STATEMENT Distribution Statement A: Approved for Public Release; Distribution Unlimited.						
13. SUPPLEMENTARY NOTES						
14. ABSTRACT In order to fully utilize newly developed $\text{Ge}_{1-y}\text{Sn}_y$ and $\text{Ge}_{1-x-y}\text{Si}_x\text{Sn}_y$ materials for new novel optoelectronic devices, the optical and electrical properties of these alloys were investigated using photoluminescence (PL) and Hall-effect measurements. Direct bandgap PL emission was observed from almost all the samples, making them very promising candidates for Si-based light emitting devices. T-dependent PL studies also indicate that the indirect-to-direct bandgap transition of $\text{Ge}_{1-y}\text{Sn}_y$ alloys might take place at a much lower Sn content than the theory predicts. T-dependent Hall-effect measurements showed both degenerate parallel conducting layers as well as a conductivity type change from p to n at around 370-435 K, which could affect the operation of devices made from these materials. Etch studies were performed to determine the properties of the epilayers alone. Reasonable results for the average volume carrier density in the film were obtained. It was also found that there exists high level of surface states at the surface of almost all the samples. These studies should be very useful for the development of practical devices based on $\text{Ge}_{1-y}\text{Sn}_y$ alloys.						
15. SUBJECT TERMS Optoelectronics, GeSn, Photoluminescence, Hall-Effect, Semiconductor Characterization, Semiconductor Alloys						
16. SECURITY CLASSIFICATION OF:			17. LIMITATION OF ABSTRACT	18. NUMBER OF PAGES	19a. NAME OF RESPONSIBLE PERSON	
a. REPORT	b. ABSTRACT	c. THIS PAGE			Prof. Yung Kee Yeo, AFIT/ENP	
U	U	U	UU	138	19b. TELEPHONE NUMBER (include area code) (937) 255-3636, x4532; yung.yeo@afit.edu	